NUMERICAL SIMULATION OF FLOW IN OPEN-CHANNELS

WITH HYDRAULIC STRUCTURES

A Thesis
Presented to
The Academic Faculty

by

Sibel Kara

In Partial Fulfillment
of the Requirements for the Degree
Doctor of Philosophy in the
School of Civil and Environmental Engineering

Georgia Institute of Technology
December 2014

NUMERICAL SIMULATION OF FLOW IN OPEN-CHANNELS

WITH HYDRAULIC STRUCTURES

Approved by:

Dr. TERRY W. STURM, Advisor
School of Civil and Environmental
Engineering
Georgia Institute of Technology

Dr. THORSTEN STOESSER, Advisor
Hydro-Environmental Research Center
Cardiff School of Engineering
Cardiff University

Dr. PHILIP J. ROBERTS
School of Civil and Environmental
Engineering
Georgia Institute of Technology

Dr. DONALD R. WEBSTER
School of Civil and Environmental
Engineering
Georgia Institute of Technology

Dr. ALEXANDER ALEXEEV
School of Mechanical Engineering
Georgia Institute of Technology

Date Approved: 23 July, 2014

Dedicated to my husband Mustafa Can Kara and my son Poyraz Kara

ACKNOWLEDGEMENTS

TABLE OF CONTENTS

LIST OF TABLES

LIST OF FIGURES

Page

x

SUMMARY

Extreme hydrological events associated with global warming are likely to produce an increasing number of flooding scenarios resulting in significant bridge inundation and associated damages. During large floods, the presence of a bridge in an open channel triggers a highly turbulent flow field including 3D complex coherent structures around bridge structures. These turbulence structures are highly energetic and possess high sediment entrainment capacity which increases scouring around the bridge foundation and consequently lead to structural stability problems or even failure of the structure. Hence, understanding the complex turbulent flow field for these extreme flow conditions is crucial to estimate the failure risks for existing bridges and better design of future bridges.

This research employs the method Large Eddy Simulation (LES) to predict accurately the 3D turbulent flow around bridge structures. The LES code is refined with a novel free surface algorithm based on the Level Set Method (LSM) to determine the complex water surface profiles. The code is used to analyze the hydrodynamics of compound channel flow with deep and shallow overbanks, free flow around a bridge abutment, pressure flow with a partially submerged bridge deck and bridge overtopping flow. All simulations are validated with data from complementary physical model tests under analogous geometrical and flow conditions. Primary velocity, bed shear stress, turbulence characteristics and 3D coherent flow structures are examined thoroughly for each of the flow cases to explain the hydrodynamics of these complex turbulent flows.

CHAPTER 1

INTRODUCTION

1.1 Statement of the Problem

Extreme hydrological events associated with global warming are likely to produce an increasing number of flooding scenarios resulting in significant bridge inundation and associated damages. During large floods, the foundation of a bridge is subject to severe scour at the sediment bed which can cause bridge failure. Wardhana and Hadipriono (2003) studied over 500 bridge failures in the United States between 1989 and 2000, and showed that flood and scour were responsible for 53% of total bridge failures. This finding points out the importance of understanding the complex turbulent flow field which is responsible for scour during extreme hydrologic events. Estimation of the probable failure risks for existing bridges and better design of future bridges depend on this knowledge to improve the scour formulations which do not take into account the bridge submergence.

In nature it is not possible to see idealized rectangular channels. Instead, compound channels formed by a main channel and floodplains which are inundated during flooding are more common. For compound channels, it is essential to investigate the flow properties and complex momentum exchange between the main channel and flood plains. A considerable amount of experimental research on the hydraulics of compound open channels is available to study the velocity distribution and boundary shear stress using Pitot static and Preston tubes (Myers and Elsawy 1975, Rajaratnam and Ahmadi 1981,

Knight and Demetriou 1983). Detailed measurements of turbulence quantities in compound channels were obtained by using Laser Doppler Anemometers LDA (Shiono and Knight 1991, Tominaga and Nezu 1991). The latter studied the effect of channel geometry and floodplain roughness on the primary velocity, secondary flow, Reynolds stress distributions, bed shear stresses and momentum transfer. A number of analytical models based on the depth-averaged momentum equation were developed to predict depth-averaged velocity distributions in compound channels (Shiono and Knight 1991, or van Prooijen *et al.* 2005). However, these methods require empirical input. For instance, the Shiono and Knight Method (SKM) needs friction factor, horizontal eddy viscosity and secondary current parameter inputs, which are difficult to obtain experimentally. Accurate numerical studies can help to quantify these parameters. A few numerical studies of compound channel hydraulics, mainly based on the Reynolds-Averaged Navier Stokes (RANS) equations, have been reported to date. Krishnappen and Lau (1986), Naot *et al.* (1993), Pezzinga (1994), and Sofialidis and Prinos (1998) showed that their models are capable of predicting reasonably well the time-averaged primary flow and bed shear stress distributions for different compound open channel geometries. Pezzinga (1994) and Sofialidis and Prinos (1998) were able to reproduce the secondary flow quite well using non-linear turbulence closures. However, the bed shear stress predictions were less accurate (Pezzinga 1994), mainly because wall functions were employed. The majority of the RANS models do not provide detailed distributions of Reynolds stresses in compound channels, which are needed to quantify the apparent stress at the interface. An alternative to RANS modeling is Large Eddy Simulation (LES), a method that resolves the large scale turbulence and hence allows for an accurate computation of second-order

turbulence statistics. A number of successful LES of hydraulic interest have been published by Constantinescu *et al.* (2009), van Balen *et al.* (2010), Palau-Salvador *et al.* 2010, Stoesser *et al.* (2010) and Kang *et al.* (2011). Thomas and Williams (1995) were the first to employ LES to study the flow and turbulence characteristics in a compound open-channel. The study of Cater and Williams (2008) complements the work of Thomas and Williams (1995), but they only focus on one test case of Tominaga and Nezu (1991), and hence Cater and Williams (2008) did not examine the effects of floodplain depth on the flow in a compound channel.

During flood conditions, bridges become partially or fully submerged and hydrodynamic forces acting on the bridge become crucial leading to stability problems for the existing structure. In addition, the bridge and abutments which behave as obstacles cause backwater at the upstream part of the bridge. Backwater water surface profiles lead to changes in the flow field, especially around the bridge and abutment. Therefore, determination of free surface elevation is essential to understand the effect of the water surface profile on the flow characteristics. There are only a few studies reported in the literature on fluid-structure interaction and estimation of the water surface profiles for inundated bridges to understand this complex flow phenomenon. Picek *et al.* (2007) conducted experiments to derive equations for backwater and discharge for flows through partially or fully-submerged rectangular bridge decks. Malavasi and Guadagnini (2003) carried out experiments to examine the hydrodynamic loading on a bridge deck having a rectangular cross section for different submergence levels and deck Froude numbers. The experimental data were used to analyze the relationship between force coefficients, the deck Froude number and geometrical parameters. They extended their experimental

3

studies to analyze mean force coefficients and vortex shedding frequencies for various flow conditions due to different elevations of the deck above the channel bottom (Malavasi and Guadagnini 2007). Guo *et al.* (2009) investigated hydrodynamic loading on an inundated bridge and the flow field around it. An experiment was conducted for a six-girder bridge deck model and the experimental data was used to validate complementary numerical simulations. In the experiments, the PIV technique was used to obtain velocity distributions. The numerical data was analyzed for different scaling factors to determine the effects of scaling on hydrodynamic loading. Lee et al. (2010) focused on water surface profiles formed as a result of different bridge structures. They investigated three cases: a cylindrical pier, a deck, and a bridge (i.e. cylindrical pier and deck). Overtopping flow was considered only for the deck and bridge cases. In the experiment, the PIV method was used to measure the velocity. A 3D Reynolds-Averaged Navier Stokes (RANS) model with k-ε turbulence closure was used to simulate all the cases. The volume of fluid method was utilized for free surface modeling. Finally, comparisons of velocity distributions and water surface levels obtained from experiments and simulations showed that the model estimates velocity distributions very well. However, it underestimates the water level rise around the structure due to inability of the k-ε turbulence model to represent such a complex flow having significant streamline curvature and body force effects.

Bridges distribute their loads to piers and abutments. In the absence of piers, abutments are the only structure transferring the loads to the ground. Excessive scour around the abutments not only causes the collapse of the abutment but it also leads to bridge failure. Therefore, investigations of the flow properties for different channel

geometries, abutment shapes and alignments and, sediment sizes and distributions are needed. Melville (1992) conducted experiments to investigate the local scour around bridge abutments and his proposed scour prediction equation takes into account abutment length, flow depth, and abutment shape and alignment. Melville (1995) extended the experiments to the case of abutments extending into the main channel of compound channels and improved his previous scour formulations by including a correction factor in his scour prediction formulat to include channel geometry effects. Sturm and Janjua (1994) carried out experiments to examine clear-water scour around abutments situated in floodplains. In the experiments, main channel and floodplain were constructed as fixed-bed and movable-bed, respectively. Moreover, approach flow velocity distribution and scour depth around the abutment were measured for different flow conditions, channel geometries and abutment lengths. Finally, a dimensionless scour formulation which includes the ratio of the approach Froude number in the floodplain to the critical Froude number for initiation of motion (equivalent to the ratio of approach flow velocity to the critical velocity), and discharge contraction ratio was suggested. Oliveto and Hager (2002) conducted experiments for different sediment sizes, channel widths and flow depths to examine the temporal variation of clear-water scour for piers and abutments in a rectangular straight channel. They proposed a clear water scour equation which includes the shape factor for pier and abutment, standard deviation of the sediment size distribution, densimetric Froude number and dimensionless time variables. Sturm (2006) proposed a common clear water scour depth equation for bankline and setback abutments after examining the flow redistribution between main channel and floodplain in the bridge contraction section for different compound channel geometries, sediment size,

bridge backwater, abutment shape, approach velocity and depth. Ouillon and Dartus (1997) carried out a numerical simulation to examine the flow around a groyne. A 3D Reynolds solver with k-ε turbulence model employing porosity method to track the free surface was used for the study. The pressure field, turbulence and shear stress distributions were analyzed for the flow. The reattachment lengths obtained from simulations using free surface and rigid-lid boundary conditions were compared. This comparison showed that the free surface boundary condition reduced the underestimation in reattachment length arising from the deficiency of the k-ε turbulence model in reattachment zones. Biglari and Sturm (1998) used a 2D RANS model to determine the flow characteristics in a compound open channel with and without abutments in the floodplains. Chrisohoides *et al.* (2003) carried out experiments and numerical computations using a 3D RANS model with the rigid lid assumption for the free surface to examine 3D vortices in the presence of a bridge abutment. Their study showed that sediment transport models should take into account 3D characteristics of mean and turbulent flow in the presence of abutments. Paik *et al.* (2004) used unsteady Reynolds-averaged Navier-Stokes (URANS) model and detached-eddy simulations (DES) to study flow in a channel with a corner-mounted rectangular block. Paik *et al.* demonstrated that DES is able to capture the recirculating region in the upstream part of the block and the shear layer originating from the edge of the block. Although, the URANS model showed the unsteadiness in the shear layer, it was not successful in capturing the dynamics of the flow in the recirculating region of the upstream part. Koken and Constantinescu (2008) studied the flow around a vertical spur dike using LES. The rigid lid assumption was used for the free surface. It was reported that the horseshoe vortex system around the base of

the spur dike varies significantly in time, and it has its largest intensity around the tip of the spur dike. It was also noted that the horse shoe vortex oscillates between two modes (zero-flow mode and back-flow mode), and this causes large fluctuations in turbulent kinetic energy and pressure inside the system. High bed shear stress values were observed around the tip of the spur dike and beneath the upstream part of the detached shear layer. Teruzzi et al. (2009) analyzed the flow field around a trapezoidal abutment by means of LES. The free surface was approximated as a rigid lid in the study. First and second order statistics analyses around the abutment showed that local scour models should include the detachment force arising from pressure stresses and turbulent fluctuations.

This objective of this study is to investigate the hydrodynamics and turbulence properties of open-channel flow with and without the presence of bridge structures using the method of Large-Eddy Simulation (LES). Its main focus is to examine three types of flows, i) free flow (free-surface flow around a bridge abutment), ii) submerged orifice flow (pressure difference between upstream and downstream side of the bridge, where the bridge deck encloses the flow) and iii) bridge overtopping flow (i.e. a completely submerged bridge) with the goal of understanding complex three-dimensional flow mechanisms leading to scour at bridge structures. Whilst for the free flow case (i), there is some work already in the literature, past studies have not taken into account the local spatial variation of the water-surface elevations and hence there is the need for investigating the effects of the free-surface on flows around bridge abutments. Studies of flow types ii) and iii) are very rare and are mostly experimental. The water surface deformations are significant and numerical models require special treatment. In this work the Level Set Method is employed to determine the air-water interface at every time step,

which has not been used previously in the context of LES. The numerical results of flow types ii) and iii) presented here are the first of its kind and will provide unprecedented details of these two flows.

1.2 Research Objectives and Scope

In order to achieve the main objective of the present study, which is to characterize the flow field in an open-channel in the presence of bridge structures under extreme flow conditions in order to understand scouring phenomena, the following tasks were planned and carried out:

- Implement the Level Set Method based free surface algorithm into an existing in-house 3D LES code and validate the code using;

    1) Experimental and numerical data obtained from the literature for a travelling solitary wave and its run-up on a vertical wall.

    2) Experimental data obtained for an open channel flow in the presence of a lateral constriction at Cardiff University's hydraulics laboratory.

- Analyze the hydrodynamics of compound open-channel flow by employing high resolution 3D LES;

- Employ 3D LES to investigate the hydrodynamics of extreme flow conditions in an open channel for i) free-surface flow around a bridge abutment, ii) submerged orifice flow and iii) bridge overtopping flow and

validate the code with experimental data obtained at Cardiff University's hydraulics laboratory

1.3 Organization of Dissertation

The organization of this dissertation, which includes 7 chapters, is briefly described below:

Chapter 1 provides the background information and literature review on compound channel flow, flow around abutments and over submerged bridge decks. The research objectives and scope of the study are given in this chapter.

In Chapter 2, the basic fluid solver is described in detail. The governing equations, spatial discretization and time advancement schemes, boundary conditions for the numerical simulations, and parallelization of the code are documented. This chapter also presents the Level Set Method, which is a free surface algorithm used to determine the changes in the water surface level over the flow field at every time step. Two validation cases i.e. the simulation of a travelling solitary wave and the simulation of flow around a lateral channel constriction are presented in this chapter.

Chapter 3 is on compound channels with deep and shallow overbank flows. This chapter gives the computational setup for the simulation domain and discusses the results of time averaged flow properties, shear stresses, momentum balance, and origin of secondary currents.

Chapter 4 discusses the effect of free surface modeling on the flow and turbulence around a bridge abutment.

Chapter 5 presents details of flow over a wholly submerged bridge and provides new insights into its time-averaged and instantaneous turbulence characteristics.

Extreme flow conditions in the presence of hydraulic structures are discussed in Chapter 6. Results for free flow around an abutment, pressure flow with a partially submerged bridge deck, and overtopping flow over a bridge deck are discussed in a comparative manner in this chapter.

Chapter 7 summarizes the conclusions of this work, highlights the main results and findings obtained from this study and finally gives recommendations for future work.

CHAPTER 2

NUMERICAL METHODOLOGY

The purpose of this study is to develop a computational tool for numerical simulations using the technique of LES for immiscible, incompressible, two-phase turbulent flows. It solves the Navier-Stokes equations using finite difference discretization on a uniform Cartesian staggered grid. The Level Set Method (LSM) is employed to track the free surface between the two fluid phases which are water and air in this study. The mass conservation problem for the two phases is treated with reinitialization of the level set function using the signum function. All convective terms in Navier Stokes and LSM are discretized by a fifth-order weighted, essentially non-oscillatory (WENO) scheme. The code is parallelized with MPI based on domain decomposition.

2.1 Basic Navier-Stokes (NS) Solver

2.1.1 Formulation in Cartesian Coordinates

2.1.1.1 Governing Equations

In Cartesian coordinates, the governing equations for an unsteady, incompressible, viscous flow of a Newtonian fluid can be written as follows:

$$\frac{\partial u_i}{\partial x_i} = 0 \tag{2-1}$$

$$\frac{\partial u_i}{\partial t} + \frac{\partial (u_i u_j)}{\partial x_j} = -\frac{1}{\rho}\frac{\partial p}{\partial x_i} + \frac{\mu}{\rho}\frac{\partial^2 u_i}{\partial x_j \partial x_j} + \frac{1}{\rho}f_i \tag{2-2}$$

11

where u_i and u_j (i,j = 1,2,3) are the velocity vector components in the corresponding directions (i.e. u_1 = u, u_2 = v and u_3=w denoting the velocity components in x, y and z directions, respectively. See Figure 2-1 for the staggered variable arrangement), t is the time, p is the pressure, ρ is the density and μ is the dynamic viscosity of the corresponding phase at a given instant of time and spatial location. Similarly, x_i and x_j represent the spatial location vectors in global X, Y and Z axis directions, respectively. In equation 2-2, f_i represents the body force.

The Large Eddy Simulation (LES) approach to solving 3D turbulent flow cases introduces a spatial filtering operation in order to separate the large, energy carrying eddies that are directly resolved and modeled. The present finite difference solver uses a top-hat filter by discrete operators. In the LES approach, turbulent scales smaller than the grid size are not resolved but accounted for through the subgrid scale (SGS) tensor given by

$$\tau_{ij} = \overline{u_i}\,\overline{u} - \overline{u_i u_j} \qquad\qquad \tau_{ij} - \frac{1}{3}\tau_{kk}\delta_{ij} = -2\mu\overline{S}_{ij} \qquad (2\text{-}3)$$

where μ is the subgrid-scale turbulent viscosity, δ_{ij} is the Kronecker symbol and $\overline{S}_{ij}$ is the rate of strain tensor for the resolved scale and it is defined by

$$\overline{S}_{ij} = \frac{1}{2}\left(\frac{\partial \overline{u}_i}{\partial x_j} + \frac{\partial \overline{u}_j}{\partial x_i} \right) \qquad (2\text{-}4)$$

The resulting governing equations for evaluation of the large scales become:

$$\frac{\partial \overline{u}_i}{\partial x_i} = 0 \qquad (2\text{-}5)$$

$$\frac{\partial \overline{u}_i}{\partial t} + \frac{\partial (\overline{u}_i \overline{u}_j)}{\partial x_j} = -\frac{1}{\rho}\frac{\partial \overline{p}}{\partial x_i} + \frac{\mu}{\rho}\frac{\partial^2 \overline{u}_i}{\partial x_j \partial x_j} + \frac{\partial \tau_{ij}}{\partial x_j} \qquad (2\text{-}6)$$

12

where the overbar denotes an appropriately chosen low-pass filter and incompressibility is assumed. In this study, the WALE model (Nicoud and Ducros 1999) is employed to compute SGS stresses and to close the filtered Navier-Stokes equations. In the WALE model, the eddy viscosity is modeled by

$$\mu = L_s^2 \frac{\left(S_{ij}^d S_{ij}^d\right)^{3/2}}{\left(\overline{S}_{ij}\overline{S}_{ij}\right)^{5/2} + \left(S_{ij}^d S_{ij}^d\right)^{5/4}} \overline{S}_{ij} \tag{2-7}$$

where L_s is the mixing length for the subgrid scales and S_{ij}^d is defined as

$$S_{ij}^d = \frac{1}{2}\left(\overline{g}_{ij}^{\ 2} + \overline{g}_{ji}^{\ 2}\right) - \frac{1}{3}\delta_{ij}\overline{g}_{kk}^{\ 2} \quad \text{and} \quad \overline{g}_{ij} = \frac{\partial \overline{u}_i}{\partial x_j} \tag{2-8}$$

The WALE model is designed to return the correct wall asymptotic (y^{+3}) behavior for wall bounded flows, where y^{+3} is the distance to the wall expressed in wall units. The effects of subgrid scale turbulence on the free-surface treatment (to be introduced below) are deemed small and are therefore neglected.

The code utilized in this thesis is an in-house LES code that has been refined over the last ten years (Kara *et al.* 2014, Rodi *et al.* 2013, Kim *et al.* 2013, Bai *et al.* 2012, Papanicolaou *et al.* 2012, Kara *et al* 2012, Kim and Stoesser 2011, Bomminayuni and Stoesser 2011, Stoesser 2010, Stoesser and Nikora 2008, Stoesser *et al.* 2007, Stoesser, Fröhlich *et al* 2007, Stoesser and Rodi 2007).
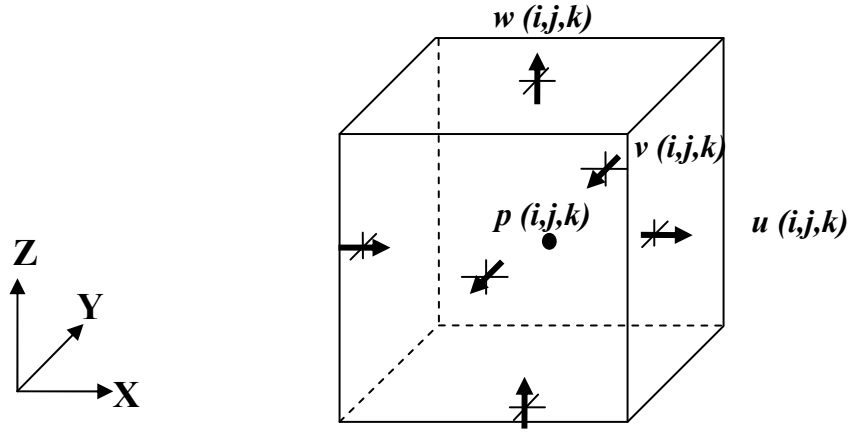
Figure 2-1 Schematic representation of a grid cell (i,j,k) in Cartesian coordinates and its staggered variable arrangement

2.1.1.2 Discretization Scheme

A fifth order WENO scheme (Shu 2009) is used for all convective terms in the momentum equation and transport equation of the level set function, ϕ, and also for re-initialization of the level set function. The WENO scheme improves the conservation properties by giving higher order approximations using a weighted combination of multiple stencils. It takes into account all stencils and assigns the largest weight to the smoothest stencil.

Herein, the WENO scheme is presented over the x component of the convective

term $\left(u_i \dfrac{\partial \phi}{\partial x_i} \right)$ of level set function equation 2-31 in the cell centers (i,j,k). Using the

upwind procedure:

$$\frac{\partial \phi}{\partial x}(i,j,k) = \begin{cases} \dfrac{\partial \phi^-}{\partial x}(i,j,k) & if \quad u > 0 \\[4mm] \dfrac{\partial \phi^+}{\partial x}(i,j,k) & if \quad u < 0 \\[4mm] 0 & otherwise \end{cases} \tag{2-9}$$

where $\dfrac{\partial \phi^-}{\partial x}(i,j,k)$ and $\dfrac{\partial \phi^+}{\partial x}(i,j,k)$ represents the left and the right-biased stencil, respectively.

These biased stencils are defined as follows:

$$\frac{\partial \phi^\pm}{\partial x}(i,j,k) = \omega_1^\pm \left(\frac{q_1^\pm}{3} - \frac{7q_2^\pm}{6} + \frac{11q_3^\pm}{6} \right) + \omega_2^\pm \left(\frac{-q_2^\pm}{6} + \frac{5q_3^\pm}{6} + \frac{q_4^\pm}{3} \right) + \omega_3^\pm \left(\frac{q_3^\pm}{3} + \frac{5q_4^\pm}{6} - \frac{q_5^\pm}{6} \right)$$

$$\tag{2-10}$$

where the $q^\pm$ terms are determined by:

$$q_1^- = \frac{\phi(i-2,j,k) - \phi(i-3,j,k)}{\Delta x}, q_2^- = \frac{\phi(i-1,j,k) - \phi(i-2,j,k)}{\Delta x},$$

$$q_3^- = \frac{\phi(i,j,k) - \phi(i-1,j,k)}{\Delta x}, q_4^- = \frac{\phi(i+1,j,k) - \phi(i,j,k)}{\Delta x}, q_5^- = \frac{\phi(i+2,j,k) - \phi(i+1,j,k)}{\Delta x}$$

and

$$q_1^+ = \frac{\phi(i+3,j,k) - \phi(i+2,j,k)}{\Delta x}, q_2^+ = \frac{\phi(i+2,j,k) - \phi(i+1,j,k)}{\Delta x},$$

$$q_3^+ = \frac{\phi(i+1,j,k) - \phi(i,j,k)}{\Delta x}, q_4^+ = \frac{\phi(i,j,k) - \phi(i-1,j,k)}{\Delta x}, q_5^+ = \frac{\phi(i-1,j,k) - \phi(i-2,j,k)}{\Delta x}$$

$$\tag{2-11}$$

and weights $\omega^\pm$ are given as

$$\omega_1^\pm = \frac{a_1^\pm}{a_1^\pm + a_2^\pm + a_3^\pm}, \quad \omega_2^\pm = \frac{a_2^\pm}{a_1^\pm + a_2^\pm + a_3^\pm}, \quad \omega_3^\pm = \frac{a_3^\pm}{a_1^\pm + a_2^\pm + a_3^\pm} \tag{2-12}$$

where

$$\alpha_1^\pm = \frac{1}{10} \frac{1}{(\tilde{\varepsilon} + IS_1^\pm)^2}, \quad \alpha_2^\pm = \frac{6}{10} \frac{1}{(\tilde{\varepsilon} + IS_2^\pm)^2}, \quad \alpha_3^\pm = \frac{3}{10} \frac{1}{(\tilde{\varepsilon} + IS_3^\pm)^2} \tag{2-13}$$

The regulation parameter, $\tilde{\varepsilon}$, is taken as 10^{-6}. Smoothness indicator values are estimated as:

$$IS_1^\pm = \frac{13}{12}(q_1 - 2q_2 + q_3)^2 + \frac{1}{4}(q_1 - 4q_2 + 3q_3)^2,$$

$$IS_2^\pm = \frac{13}{12}(q_2 - 2q_3 + q_4)^2 + \frac{1}{4}(q_2 - q_4)^2, \tag{2-14}$$

$$IS_3^\pm = \frac{13}{12}(q_3 - 2q_4 + q_5)^2 + \frac{1}{4}(3q_3 - 4q_4 + q_5)^2$$

There are not enough stencils close to the boundaries to carry out these calculations so that three extra ghost cells are introduced at the boundaries to solve this problem. A third order Lagrange interpolation scheme is used to approximate the velocities at the cell centers. For determination of the u velocity in x direction at the cell center, this scheme reads:

$$u(ijk) = \frac{1}{16}\left(-u(i-2,j,k) + 9u(i-1,j,k) + 9u(i,j,k) - u(i+1,j,k)\right) \tag{2-15}$$

For the boundaries, right and left weighted Lagrange interpolation reads as follows:

Left weighted: $u(ijk) = \dfrac{1}{16}\left(5u(i-1,j,k) + 15u(i,j,k) - 5u(i+1,j,k) + u(i+2,j,k)\right)$

Right weighted: $u(ijk) = \frac{1}{16}\left(u(i-3,j,k) - 5u(i-2,j,k) + 15u(i-1,j,k) + 5u(i,j,k)\right)$

(2-16)

2.1.1.3 Time Advancement Scheme

In the present work, there are several choices of time advancement schemes. The convective terms are advanced in time using either the second-order Adams-Bashforth (AB2) or the low-storage third-order explicit three-step Runge-Kutta (RK3) scheme in which the governing equations are discretized in time providing second-order accuracy in time where all terms in the right hand side of momentum equations are advanced explicitly, while the diffusive terms are discretized in time via the second-order Crank-Nicolson (CN) scheme. In particular, the momentum equation is solved to find the intermediate velocity and first guess of the velocity field by:

$$\frac{\hat{u}_i^k - u_i^{k-1}}{\Delta t} = \alpha_k C(u_i^{k-1}) + \beta_k C(u_i^{k-2}) + \frac{1}{2}\alpha_k D(u_i^{k-1} + \hat{u}_i^k) - \alpha_k \frac{\partial p^{k-1}}{\partial x_i}$$

(2-17)

$$u_i^k = \hat{u}_i^k - \alpha_k \Delta t \frac{\partial p^{k-1}}{\partial x_i}$$

(2-18)

where k is the substep index, which ranges from one to three for Runge-Kutta scheme (RK, RK2, RK3) and equals one for Adams-Bashforth scheme, $\hat{u}_i^k$ is the intermediate velocity, p^{k-1} is the pressure field. C and D are the spatial operators for convective, diffusive and SGS terms, respectively, and Δt is the time step. The RK3 coefficients are

$$\alpha_1 = \beta_1 = 1/3 \qquad \alpha_2 = \beta_2 = 1/2 \qquad \alpha_3 = \beta_3 = 1 \qquad (2\text{-}19)$$

and the AB2 coefficients are

17

$$\alpha_1 = 3/2 \qquad \beta_1 = -1/2 \qquad\qquad (2\text{-}20)$$

The following stability criterion, in other words the generalized Courant-Friedrichs-Levy (CFL) number, is a necessary condition for convergence. CFL takes into account the restrictions coming from convection, viscosity and gravity terms and, is given as follows for the x component of the velocity;

$$\delta t_{gcv}^u \leq 2 \left(\left(\frac{u_{max}}{\delta x} + V \right) + \sqrt{\left(\frac{u_{max}}{\delta x} + V \right)^2 + \frac{4|g_x|}{\delta x}} \right)^{-1} \qquad\qquad (2\text{-}21)$$

where $V = \max \left\{ \dfrac{\mu_l}{\rho_l}, \dfrac{\mu_g}{\rho_g} \right\} \left(\dfrac{2}{(\delta x)^2} + \dfrac{2}{(\delta y)^2} + \dfrac{2}{(\delta z)^2} \right)$ and, subscripts l and g stands for liquid

and gas, respectively. If Equation 2-21 is presented as $\delta t_{gcv}^u \leq 2 C_u$, overall time restriction

considering x,y, and z coordinates can be determined as $\delta t \leq 2 \xi \min_{\Omega}(C_u, C_v, C_w)$. Herein,

ξ is the safety factor taken as 0.1 throughout this study.

Although the theoretical limit for the three-step Runge-Kutta scheme is $\sqrt{3}$, the actual CFL number in the simulations is lower since the cross-terms are not included in the calculation of this criterion. A value of 0.3 for CFL is used in most of the simulations in this work. On the other hand, for the second order Adams-Bashfort scheme, the theoretical stability limit is CFL<1. However, the actual CFL number in the simulations has to be lower, CFL = 0.2, in order to prevent the code from crashing since higher CFL values cause instability in the simulations. In the present work, the three-step Runge-Kutta scheme is used for time advancement of both convective terms and diffusive terms.

2.1.2 Poisson Equation and the Solution Procedure

A parallel multigrid solver *mgd2* and *mgd3* originally written by Bunner (1998) is implemented in the present code which solves the non-separable Poisson equation:

$$\frac{\partial^2 \varphi}{\partial x_i \partial x_i} = \frac{1}{\Delta t}\frac{\partial u_i}{\partial x_i} \tag{2-22}$$

It uses a domain decomposition technique and employs staggered grids with cell-centered operations. It uses full weighting for the restriction and bilinear interpolation for the correction. The discrete form of the above equation in 3D Cartesian coordinates for uniform grid spacing can be written as:

$$(\frac{\delta^2}{\delta^2 x} + \frac{\delta^2}{\delta^2 y} + \frac{\delta^2}{\delta^2 z})\phi_{i,j,k} = \frac{1}{\Delta t}(\frac{u_{i,j,k} - u_{i-1,j,k}}{\Delta x} + \frac{v_{i,j,k} - v_{i,j-1,k}}{\Delta y} + \frac{w_{i,j,k} - w_{i,j,k-1}}{\Delta z})$$

$$\tag{2-23}$$

The solver developed for the calculation of the flow field utilizes the SIMPLE algorithm which stands for Semi-Implicit Method for Pressure-Linked Equations. The procedure adopted has been described in and used to integrate the governing equations in time. In particular, the important operations of the solution procedure in the order of their execution can be described in the following sequence of steps (*a* to *e*):

Step a: Store the velocity and pressure fields obtained at the end of previous time step.

Step b: The momentum equation is solved to find the intermediate velocity and first guess of the velocity field as in Eqs (2-17) and (2-18).

Step c: The pressure correction equation is solved to find the pressure scalar, φ.

Step d: The pressure and velocity field is corrected employing the following equations.

19

$$p^k = p* + \varphi^k \quad , \qquad u_i^k = \hat{u}_i^k - \alpha_k \Delta t \frac{\partial p^k}{\partial x_i} \qquad \text{(2-24)}$$

Step e: Treat the corrected pressure p^* as a new guessed pressure, return to *step c* and repeat the whole procedure until convergence for the momentum and pressure-correction equations is reached

2.1.3 Implementation of Boundary Conditions

In the current study, ghost cells are used to impose the proper external boundary conditions (i.e. inlet, outlet, south, north, top and bottom boundaries). Its advantage lies in the fact that grid spacing near the boundary is continuous and the software can have generalized form for all grid points at which the equations are solved. Moreover, it makes the domain decomposition technique easier for parallelization.

<u>2.1.3.1 Dirichlet and Neumann Boundary Conditions</u>

A schematic representation of the Dirichlet and Neumann boundary conditions and their layout is shown in Figure 2-2, in which the lower-left corner of a X-Y plane of the computational domain and the collocation of the variables such as streamwise, transverse directional velocities, *u*, *v* along with pressure and viscosity, *p and υ,* are given. At the boundaries there are three ghost cells so that computational domain indices start with four. For the sake of clearness, only one ghost cell is shown in the Figure 2-2. For the given velocity component which is normal to the wall, e.g., *u* to the lower boundary and *v* to the left boundary in Figure 2-2, the Dirichlet condition can be written as

$$u_{3,j,k} = u_b \quad \text{and} \quad v_{i,3,k} = v_b \qquad \text{(2-25)}$$

where u_b and v_b are the prescribed normal velocity components on the lower wall and left wall, respectively.

The no-slip conditions for the wall-tangential components are directly enforced through the use of ghost cells:

$$u_{i,3,k} = -u_{i,4,k} \quad \text{and} \quad v_{3,j,k} = -v_{4,j,k} \tag{2-26}$$

On the other hand, a homogeneous Neumann boundary condition for an arbitrary variable, φ, can be implemented as

$$\frac{\partial \varphi}{\partial n} = 0 \quad , \quad \varphi_{3,j,j} = \varphi_{4,j,j} \tag{2-27}$$
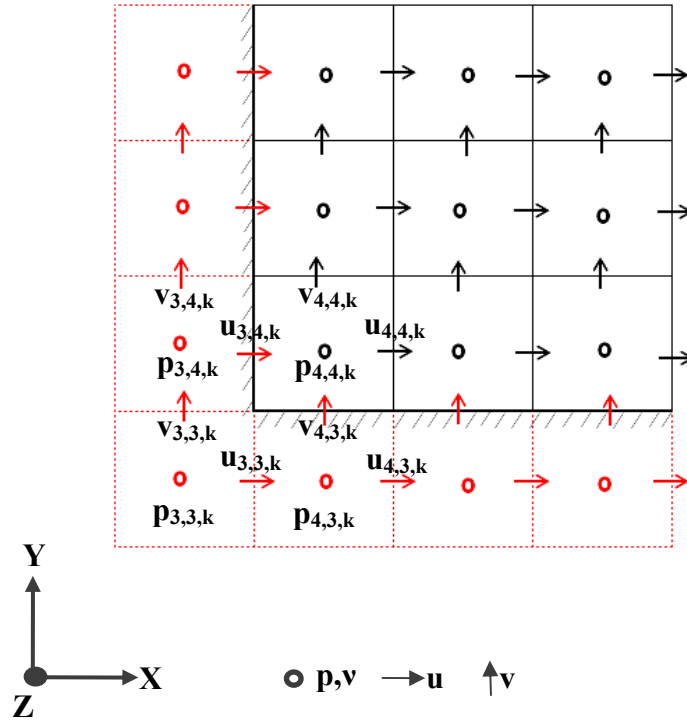
Figure 2-2 The implementation of proper Dirichlet and Neumann boundary condition on XY plane of the computational domain

2.1.3.2 Periodic Boundary Condition

As shown in Figure 2-3, the periodic boundary condition through ghost cells is implemented simply by copying values such as velocities (u,v,w) and pressure (p) on the left side directly to the ghost cells on the right side of the local domain and vice versa in such a way that:

$$u_{ni-2,j,k} = u_{4,j,k} \quad , \quad v_{ni-2,j,k} = v_{4,j,k} \quad , \quad w_{ni-2,j,k} = w_{4,j,k} \quad , \quad p_{ni,j,k} = p_{2,j,k}$$

$$u_{3,j,k} = u_{ni-3,j,k} \quad , \quad v_{3,j,k} = v_{ni-3,j,k} \quad , \quad w_{3,j,k} = w_{ni-3,j,k} \quad , \quad p_{1,j,k} = p_{ni-1,j,k} \quad (2\text{-}28)$$

where n_i stands for the number of cells in X,Y and Z directions of the computational domain.
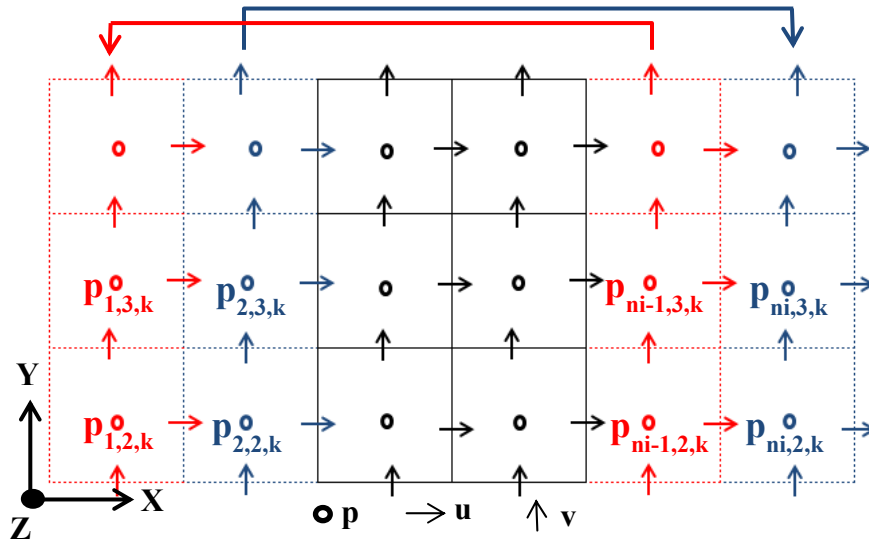
Figure 2-3 The implementation of proper periodic boundary condition on XY plane of the computational domain for pressure cells. Arrows show the directions of data duplication.

<u>2.1.3.3 Convective Boundary Condition</u>

Free surface flow under the bridge deck, pressure flow with a partially submerged bridge deck, and overtopping flow over a bridge deck studies utilize Orlanski (1976)'s proposed convective boundary condition for outflow boundaries. He found a very successful method in convecting coherent structures such as vortices out of the domain without distorting the flow in the computational domain. In other words, mass is conserved through the whole computational domain. In that case, the following equation can lead to a conservative boundary velocity as follows:

$$\frac{\partial u_i}{\partial t} + U_\infty \frac{\partial u_i}{\partial x_i} = 0 \qquad\qquad (2\text{-}29)$$

in which u_i is any velocity component, and U_∞ is the convective velocity which is set to the mean streamwise velocity at the exit plane. The proposed equation is discretized using an explicit Euler scheme in time with a one-sided difference for the streamwise velocity component and central difference for the other two velocity components in space. In addition, the streamwise velocity component is adjusted every time step to globally conserve mass.

2.2 Free Surface Treatment

There are a number of methods in the literature to compute fluid dynamic problems with free surfaces. The basic methods can be given as Marker and Cell Method (MAC), Volume of Fluid Method (VOF), and Level Set Method (LSM). LSM is employed to determine the free surface level in this study.

The MAC method developed by Harlow and Welch (1965) identifies the flow domain and its free surface by employing massless marker particles. Particles moving with the velocity field help to track the free surface. The method is extended to two-phase flow by Daly (1967). Then it is improved to solve the difficulties in explicit reconstruction of the interface and extensively used by many researchers such as Chen *et al.* (1997), Glimm *et al.* (1998), Griebel *et al.* (1998), Tryggvason *et al.* (2001).

VOF method developed by DeBar (1974) employs the volume fraction function. This function shows the volume fraction of one fluid in a discretization cell. In this method, the interface is reconstructed and propagated implicitly with the help of the volume fraction function. VOF does not have any difficulty in explicit reconstruction of the interface. However, it is hard to get a high accuracy with VOF due to discontinuities in the volume fraction function. To solve this problem, a number of interface reconstruction methods were developed such as the Simple Line Interface Calculation (SLIC) by Noh and Woodward (1976), and the Piecewise Linear Interface Calculation (PLIC) by Hirt and Nichols (1981), and by Youngs (1982).

LSM developed by Osher and Sethian (1988) uses a level set function ϕ assigned as a signed distance function. It has zero value at interface Γ and fluids on either side of the interface can be identified by the sign of $\phi.$ LSM is a very powerful method in the description of complicated boundaries and it gives continuous approximations. However, it has difficulties in conserving mass due to numerical dissipation introduced in discretization of the level set equation. This problem is solved by using higher order advection schemes which is WENO in this study. Another reason causing the mass

conservation problem is distortion of the level set function. Level set function assigned as signed distance function does not maintain its property of $|\nabla \phi| = 1$ as time proceeds. Sussman *et al.* (1994) introduced a re-initialization technique to solve this problem and improve the mass conservation. This technique will be discussed in detail at section 2.2.2.

2.2.1 Level Set Equation and Smoothing

Level set function ϕ uses a signed distance function such that

$$\phi(x,t) \begin{cases} < 0 & if \quad x \in \Omega_{gas} \\ = 0 & if \quad x \in \Gamma \\ > 0 & if \quad x \in \Omega_{liquid} \end{cases} \tag{2-30}$$

where Ω_{gas} and Ω_{liquid} represent the fluid domains for gas and liquid, respectively and Γ is the interface. The interface moves with the fluid particles, expressed through a pure advection equation of the form (Sethian and Smereka 2003):

$$\frac{\partial \phi}{\partial t} + u_i \frac{\partial \phi}{\partial x_i} = 0 \tag{2-31}$$

Since density and viscosity are constant along the particle paths for immiscible fluids, discontinuities in these properties at the interface will cause numerical instabilities. This is avoided by the introduction of a transition zone in which density and viscosity switch smoothly between water and air. The transition zone is defined as $|\phi| \le \varepsilon$ where ε is the half thickness of the interface, which in this study is two grid spacings. A

25

Heaviside function, $H(\phi)$ accomplishes the transition as follows (Zhao et al. 1996, Osher and Fedkiw 2002):

$$\rho(\phi) = \rho_g + (\rho_l - \rho_g)H(\phi) \quad \text{and} \quad \mu(\phi) = \mu_g + (\mu_l - \mu_g)H(\phi) \tag{2-32}$$

where

$$H(\phi) = \begin{cases} 0 & \text{if} \quad \phi < -\varepsilon \\ \dfrac{1}{2}\left[1 + \dfrac{\phi}{\varepsilon} + \dfrac{1}{\pi}\sin\left(\dfrac{\pi\phi}{\varepsilon}\right)\right] & \text{if} \quad |\phi| \leq \varepsilon \\ 1 & \text{if} \quad \phi > \varepsilon \end{cases} \tag{2-33}$$

In this study, surface tension is ignored for the free surface treatment because it s effect is deemed negligibly small for open channel flows.

2.2.2 Re-initialization of Level Set Function

The level set function assigned as a signed distance function does not maintain its property of $|\nabla\phi| = 1$ as time proceeds. Sussman *et al.* (1994) introduced a re-initialization technique to satisfy signed distance property at every time step. The re-initialized signed distance function d is obtained by solving the partial differential equation given by (Sussman *et al.* 1994)

$$\frac{\partial d}{\partial t_a} + s(d_0)(|\nabla d| - 1) = 0 \tag{2-34}$$

where $d_0(x,0) = \phi(x,t)$, t_a is the artificial time and $s(d_0)$ is the smoothed signed function given as

$$s(d_0) = \frac{d_0}{\sqrt{d_0^2 + (|\nabla d_0| \varepsilon_r)^2}} \qquad (2\text{-}35)$$

This re-initialization is applied throughout the transition zone within several iteration steps, $\dfrac{\varepsilon_r}{\Delta t_a}$, where ε_r represents one grid spacing. Those adjustments to the level set function are employed only for computational cells lying on the interface, so that there is no need to solve this partial differential equation for the whole domain.

2.2.3 LSM Validation Cases

2.2.3.1 A Travelling Solitary Wave

The proper implementation of the LSM and the validation of its accurate treatment of the free water surface are carried out for a travelling solitary wave and its run-up on a vertical wall, which is simple to setup but challenging as a validation case. The setup is shown in Figure 2-4. The dimensions of the channel are 20*h*×*h*×2*h* in *x*,*y* and *z* directions, respectively. Different grid resolutions were tested to assess mesh independence, and it is found that the results are not very sensitive to the grid resolution once LES-adequate grids are employed. The finest grid, results of which are reported below, consisted of 320×16×160 uniformly spaced points in the *x*,*y* and *z* directions, respectively. The no-slip boundary condition is employed at the left, right, bottom, and top walls of the domain and the slip boundary condition is used for the spanwise

27

boundaries of the domain. The quantities, A_0, A_c, and A_{run-up} represent the wave amplitude released from the left vertical wall, the wave amplitude at the center, and the wave amplitude at the right vertical wall, respectively. The theoretical wave speed is $C_w = (gh)^{1/2} = 1.0$ m/s and non-dimensional time is $T = t/(h/C_w)$. The dynamic viscosity of water and air are taken as 1×10^{-3} kg/(ms) and 1.8×10^{-5} kg/(ms), respectively. The density of water and air are 1000kg/m³ and 1kg/m³, respectively. The acceleration due to gravity is g=9.81m/s². Initially, a still water surface having a Boussinesq profile with zero velocity is released from the left vertical wall,

$$A(x, y, t = 0) = A_0 / \cosh^2\left(\frac{\sqrt{3A_0}}{2}x\right) \qquad (2\text{-}36)$$

The water moves in the horizontal direction due to gravity and after reaching $X\approx6h$ it behaves as a solitary wave, and T=0 is set at X=6h.
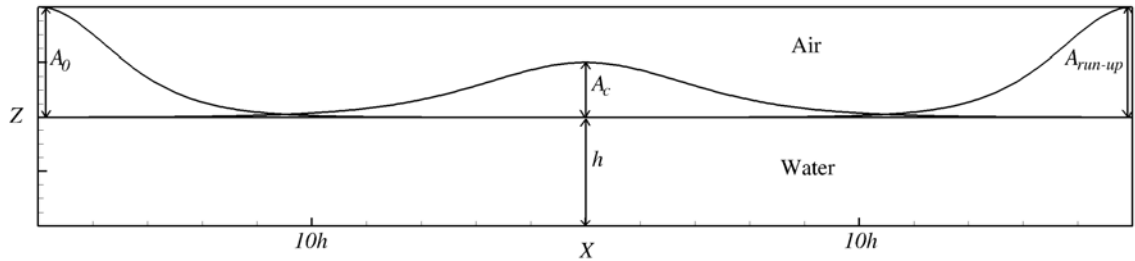
Figure 2-4 Computational domain for travelling solitary wave test case.

Travelling solitary waves of different initial amplitudes are simulated and their water surface profiles are obtained at different normalized time values T (see Figure 2-5 a-i). The assessment of the accuracy of the LSM implementation is accomplished in two ways: first the computed wave speed is compared with the theoretical one. The wave

28

speed for the initial wave amplitude of A_0/h=0.4 is computed to be 1.05m/s which is within 5% of the theoretical value suggesting minimal viscous damping of the wave. The second method of assessment is the computation of the wave run-up (the highest point at the right vertical wall) and its comparison with experimental (Chan and Street 1970) and numerical data (Yue *et al*. 2003) for several initial wave amplitudes. Figure 2-6 presents the wave run-up values for experiments and numerical computations, and the very good agreement indicates that the LSM is capable of accurately predicting free surface deformation for relatively steep water surface profile gradients.

(a)

(b)

(c)

(d)

(e)

30

(f)

(g)

31

(h)

(i)
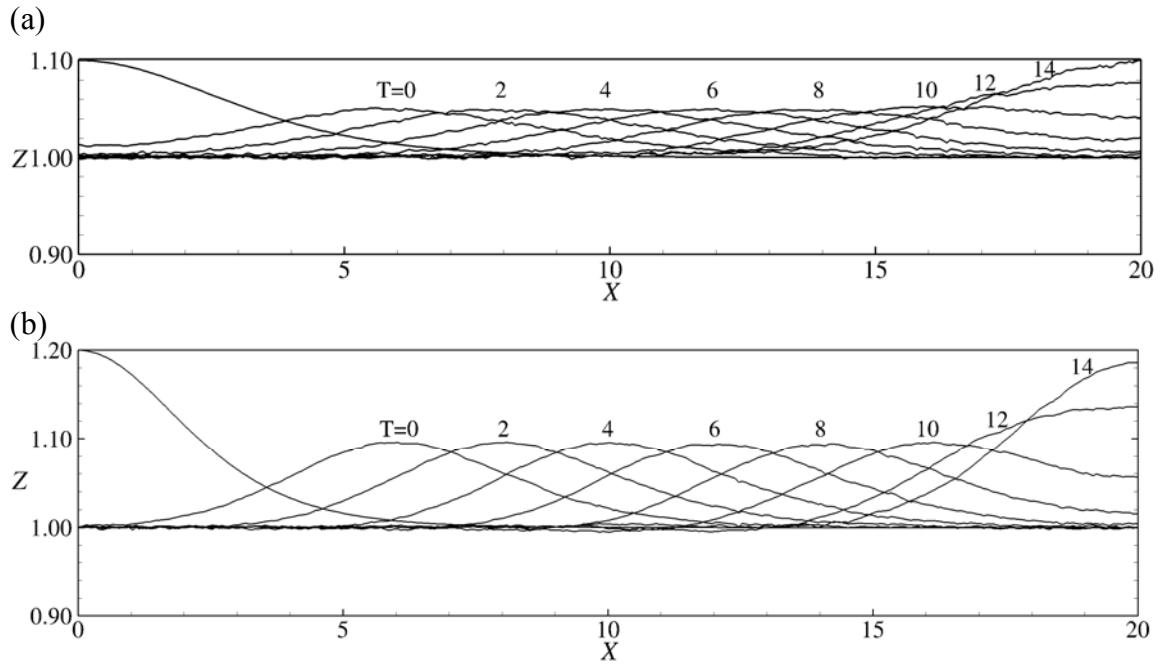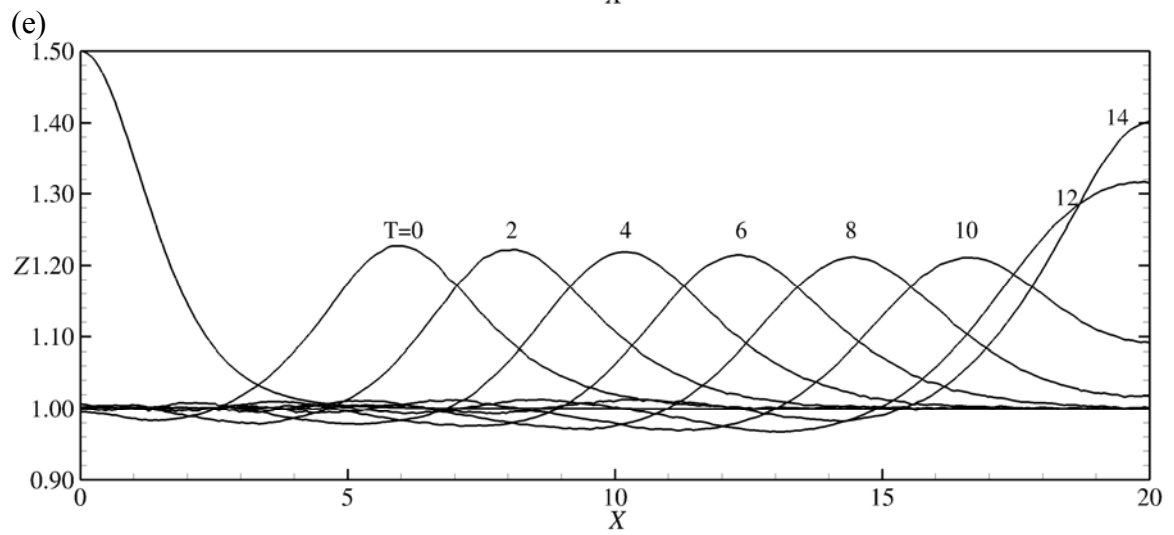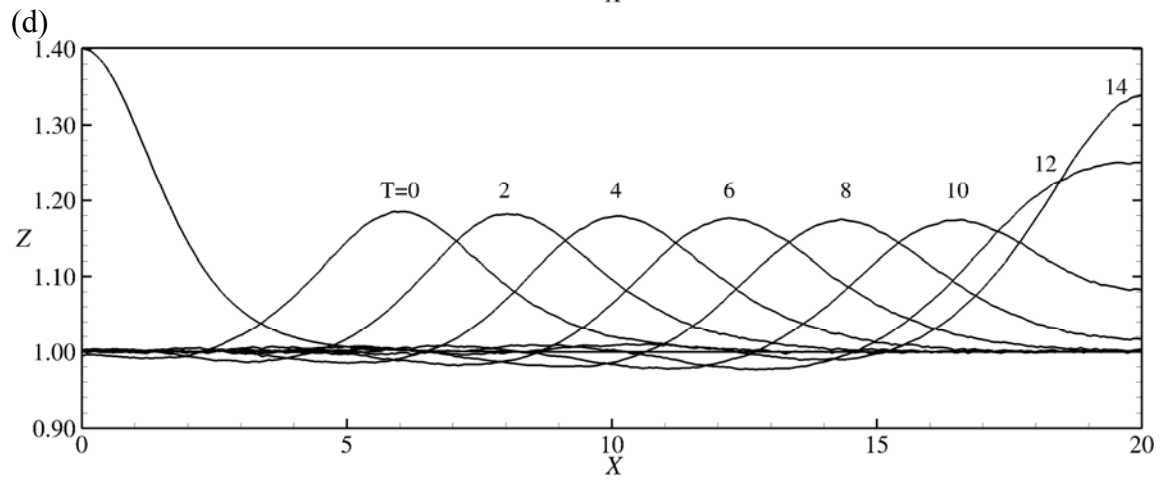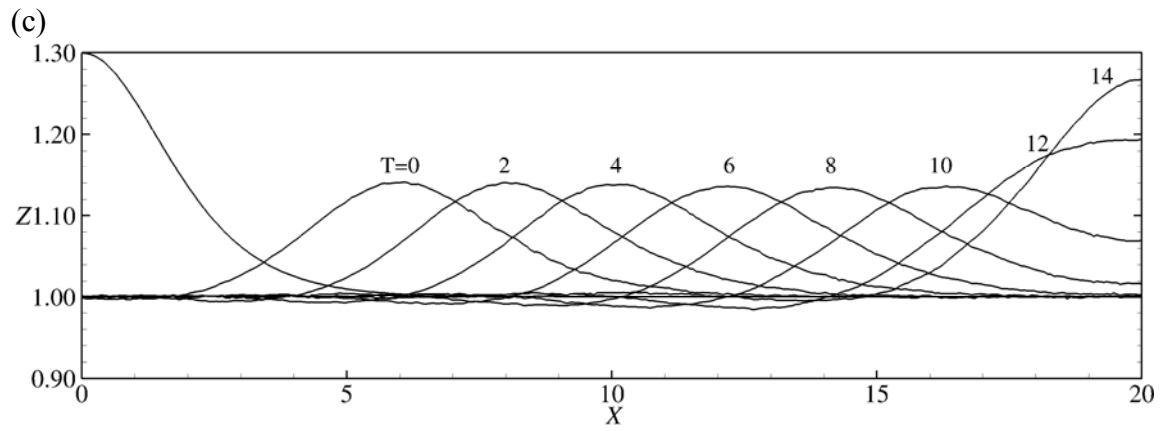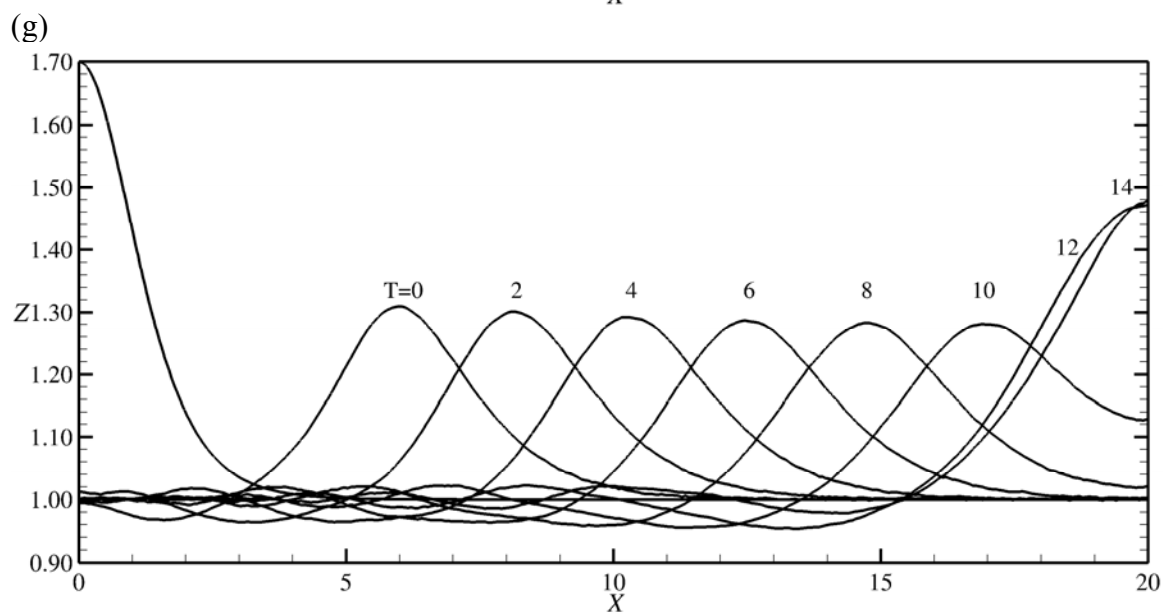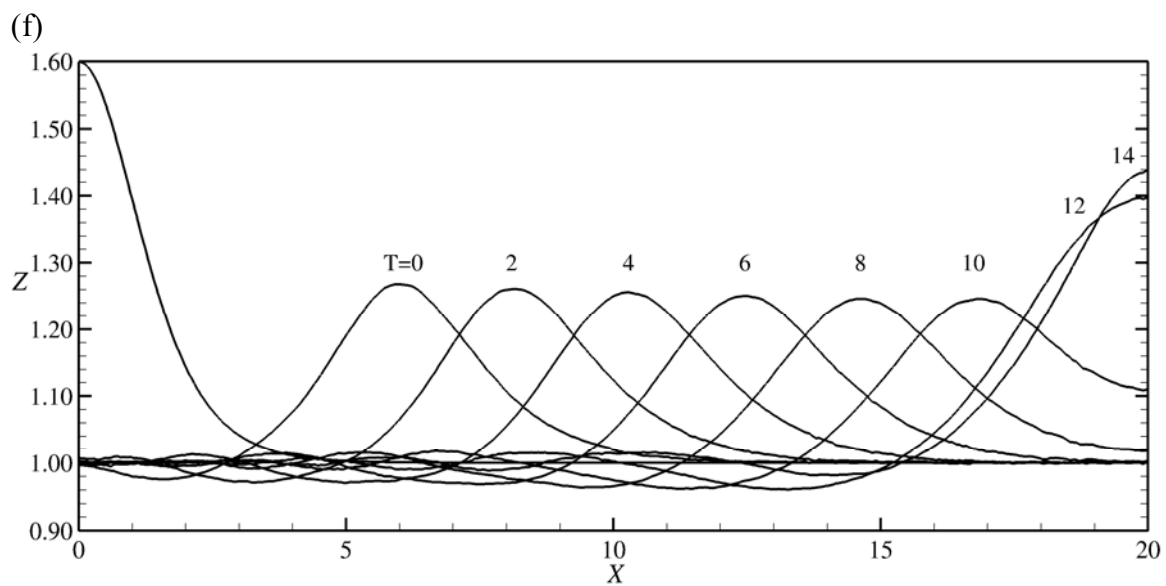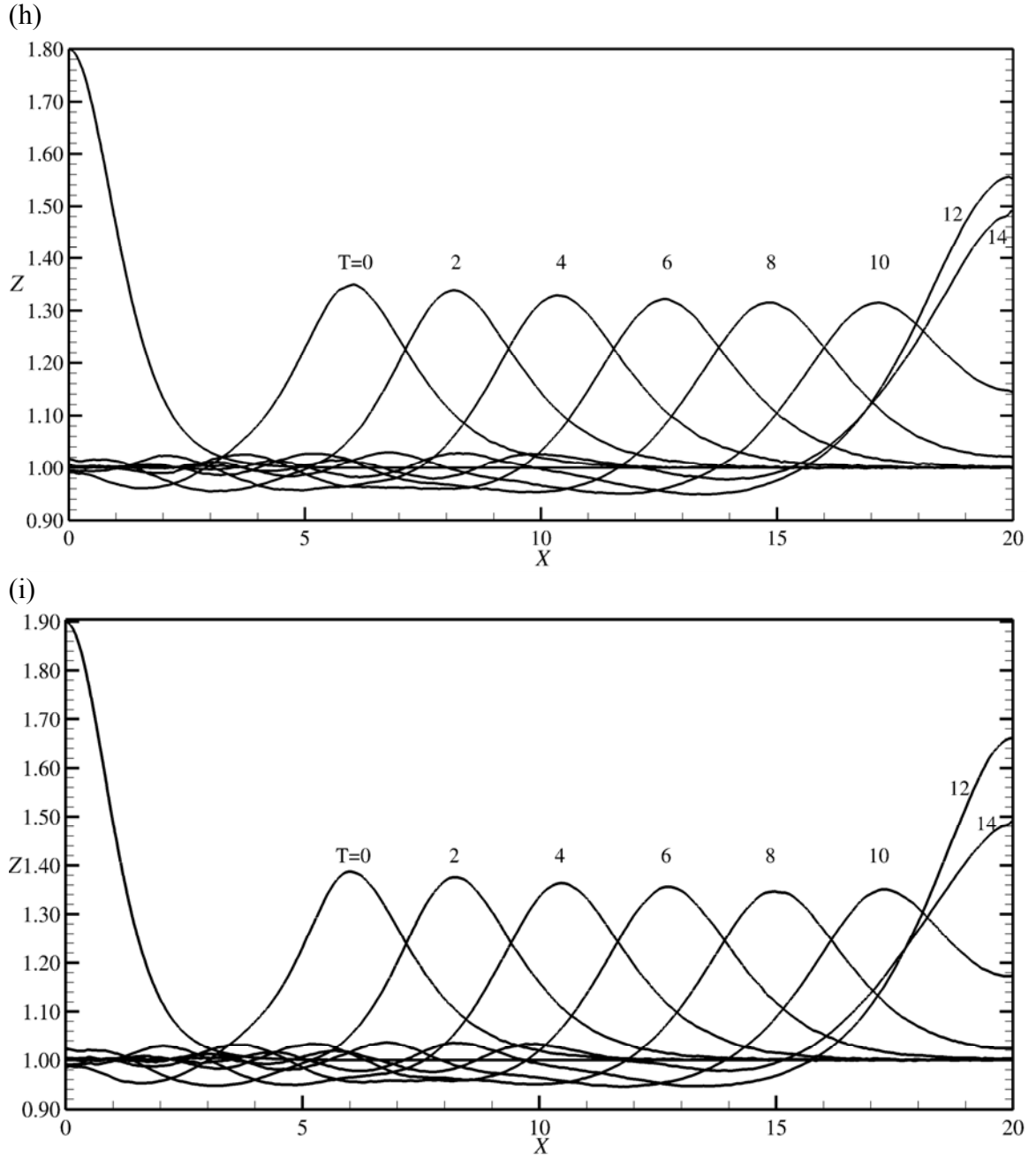
Figure 2-5 Travelling solitary waves with initial wave amplitudes of (a) A_0/h=0.1, (b) A_0/h=0.2, (c) A_0/h=0.3, (d) A_0/h=0.4, (e) A_0/h=0.5, (f) A_0/h=0.6, (g) A_0/h=0.7, (h) A_0/h=0.8, and (i) A_0/h=0.9.
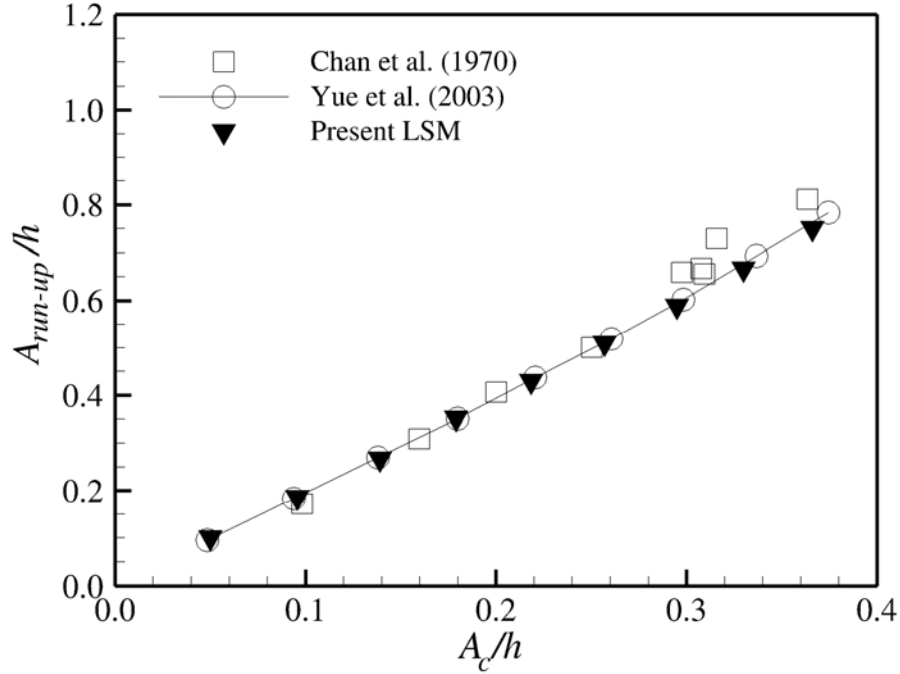
Figure 2-6 Wave run-up versus wave amplitude at the center.

2.2.3.2 Flow around a Lateral Channel Constriction

Investigation of turbulent flow mechanisms around lateral channel constrictions such as spur dikes or abutments is crucial in terms of the design of these hydraulic structures. The complex behavior of the flow with coherent vortical structures induced due to the constriction leads to sediment erosion around the hydraulic structure and causes its failure. There are a number of studies carried out in the literature to enlighten the effects of these coherent vortical structures on the scouring process. Chrisohoides *et al*. (2003) performed experimental and numerical studies to investigate large-scale vortices formed due to presence of bridge abutments in a flat bed. A visualization technique was used to examine these vortices at the free surface. Reynolds-averaged Navier-Stokes (RANS) equations with $k - \omega$ turbulence model were employed in numerical computation with the rigid lid assumption for the boundary condition at the

33

free surface. Effects of the large-scale vortices on the scouring process were discussed in detail. Nagata *et al*. (2005) employed RANS and a morphological model to simulate bed deformation around hydraulic structures (spur dike and bridge pier). They resolved the free surface with highly simplified mark-and-cell (HSMAC) method. Comparison of the results with the experimental data showed that the model was able to reproduce the flow and scour hole geometry with sufficient accuracy. Paik and Sotiropoulos (2005) used an experimental technique and a complementary Detached Eddy Simulation (DES) to visualize and deduce the free surface upstream of a long, rectangular side wall in a shallow open channel at Reynolds number **R** = 420,000 and Froude number **F** = 0.35. The free surface was approximated as a rigid lid due to the low **F** number suggesting that the gravity force is able to suppress vertical free surface fluctuations. Koken and Constantinescu (2009) carried out DES to examine the dynamics of coherent structures and sediment entrainment mechanisms for a turbulent channel flow with a vertical sidewall obstruction. The free surface was treated as a rigid lid in the simulation. They also examined scaling effects by comparing the high Reynolds number, **R** = 500,000 DES results with the low Reynolds number, **R** = 18,000 LES results.

This study aims to contribute to existing literature in understanding the turbulent flow mechanism and effects on scouring around lateral channel constrictions by examining the data from experimental and numerical simulations. As distinct from the other studies, this study is performed for a relatively small width channel having a constriction that extends up to half of the channel width. The wall effect is more pronounced for this flow condition. Even though flow is subcritical in the inlet part, it transitions to the supercritical condition around the lateral constriction. During the

transition of the flow from supercritical to subcritical in the downstream section, an undular hydraulic jump occurs. This situation makes it impossible to use the rigid lid boundary condition for the free surface and requires the employment of a free surface algorithm in the simulations.

Experiments were conducted in Cardiff University's hydraulics laboratory in a $2W$=30cm wide tilting flume that featured a L=29cm long and W=15cm wide lateral constriction. Computational setup in Figure 2-7 was determined corresponding to this experimental geometry. The discharge was chosen as Q=4.92l/s for which the uniform flow depth was H=4.3cm. This resulted in a bulk velocity of U_b=0.38m/s and mean shear velocity of u_*=0.018 m/s. The Reynolds number based on U_b and the hydraulic radius, R was R = 50,000 and the Froude number was F=0.59. The flow through the constriction and downstream of it is characterized by very strong variation of the water surface featuring standing waves and local depressions. Water surface measurements were carried out using a point gage to validate the free surface algorithm of LES code. For the numerical simulation, the inflow velocity distribution was obtained from a preliminary periodic channel simulation for the same Reynolds number at every time step. Then the velocity distributions were fed in to the present domain thorough the inflow section. This method provided a realistic description of the inflow condition having unsteady eddies at the inlet section close to a lateral constriction. For smooth walls, the no-slip boundary condition was used. The computational domain was discretized with a uniform mesh having 200×80×32 cells in the streamwise, spanwise, and vertical directions, respectively. The dynamic viscosity of water and air are taken as 1×10^{-3} kg/(ms) and

1.8075×10⁻⁵ kg/(ms), respectively. The density of water and air are 1000kg/m³ and

1.205kg/m³, respectively. The acceleration due to gravity is g=9.81m/s².
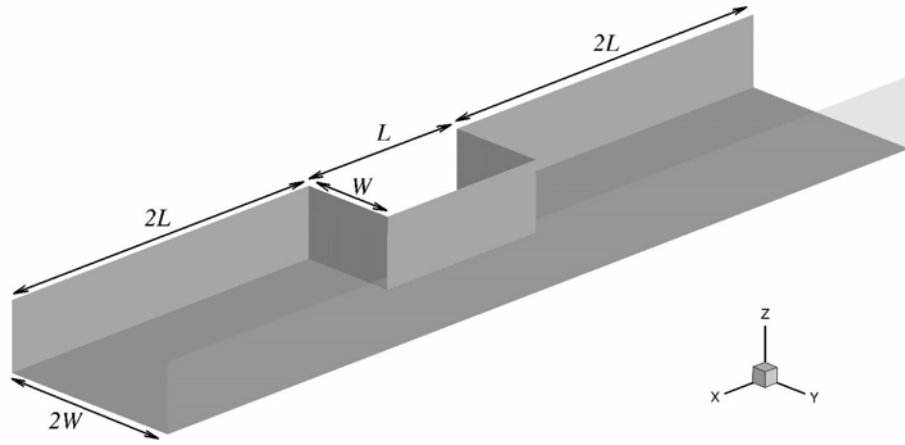
Figure 2-7 Computational setup for LES.

Water surface profiles are compared with the experimental data for different

sections given in Figure 2-8. Profiles A-D starting close to the constriction and going

towards the main channel are the longitudinal profiles extending all the way throughout

the domain length. Profiles a-e compare the water surface profiles in cross section across

the domain width.
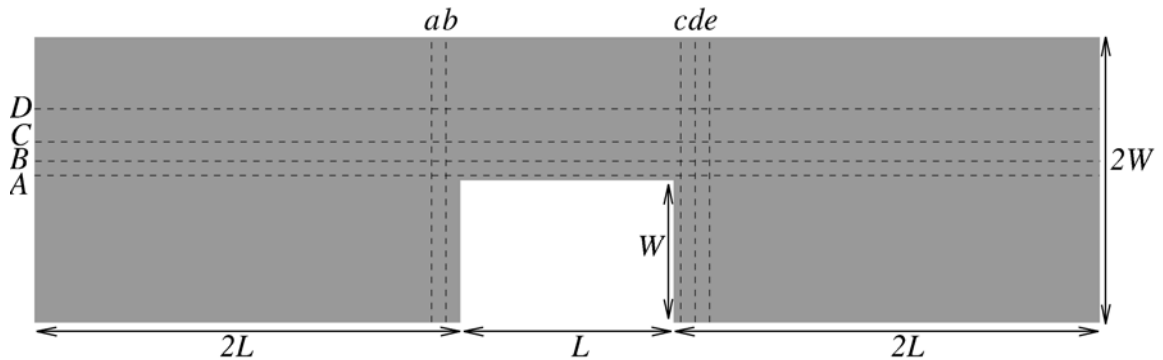
Figure 2-8 Longitudinal and cross sectional sections for water surface profile comparisons.

Figure 2-9 presents cross-sectional water surface profiles immediately before (profile a-b) and after (profile c-d) the constriction as obtained from experiment and LES. The water surface elevations are normalized with H. The match between simulation and experiment upstream of the constriction is quite satisfying and the lateral gradient is reproduced very well. However, the minimum points in the water surface profiles c-e observed throughout the experiment need finer grid resolution to be exactly captured. This gradient reflects the acceleration of the fluid in the non-constricted area due to the presence of a recirculation zone just upstream of the constriction. The gradient in water surface elevation increases closer to the constriction. The cross-sectional profiles downstream of the constriction exhibit a very significant jump in the water surface. The recirculation zone downstream of the constriction is at a significantly lower elevation than the rest of the channel. The water that rushes out of the constricted area has a significant amount of streamwise momentum prohibiting the filling of the recirculation zone with fluid.
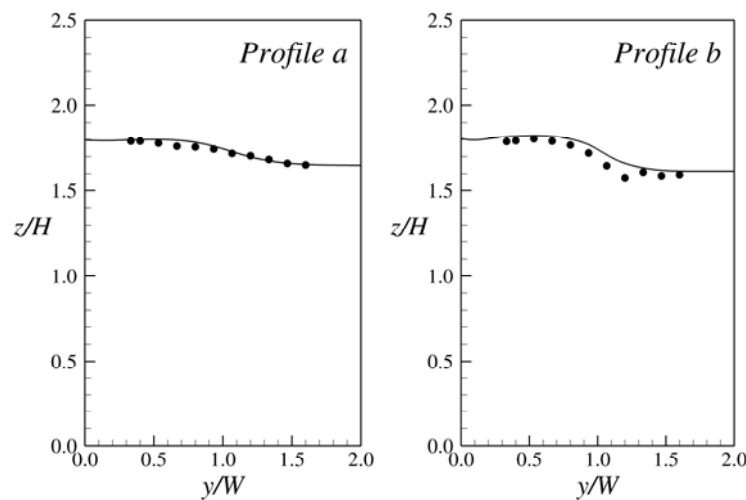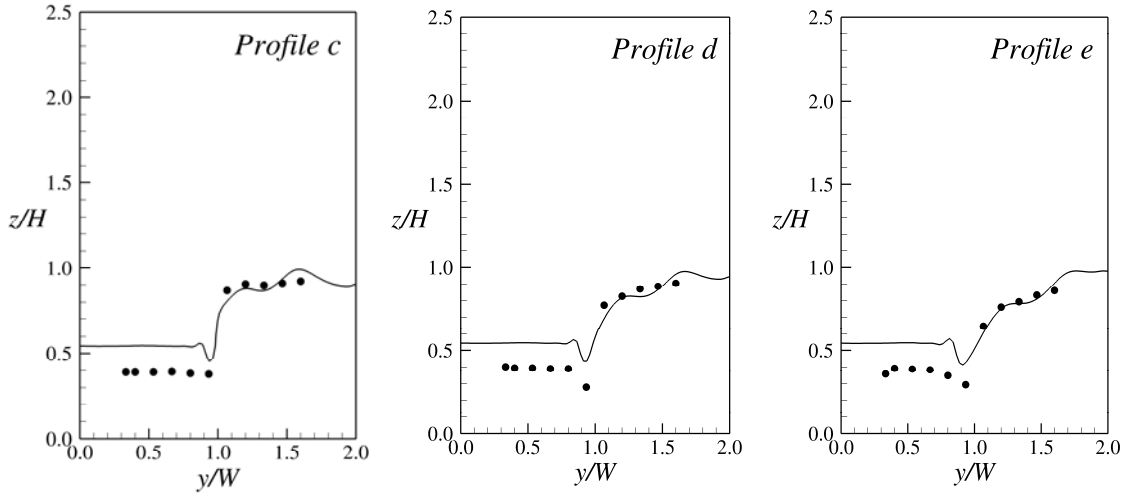
Figure 2-9 Water surface profile comparisons for cross sections (Dots represent the experimental data. Solid black lines represent LES results)

The water surface profiles in longitudinal Profiles A-D are presented in Figure 2-10. Overall, the profiles obtained from the LES show reasonable agreement with the experimental data. The water is backed up by a significant amount upstream of the structure and the LES predicts this quite well. A bit upstream of the structure the flow starts to accelerate and the water surface drops rapidly and significantly. The flow creates a very distinct local dip in the area of local recirculation as a result of flow separation at the leading edge of the constriction. The water surface recovers markedly approximately halfway through the constriction in the form of a standing wave. The simulation is reproduces this fairly well away from the structure (Profiles C and D); however, very close to the structure (e.g. Profile A) the agreement is not so good. This can be attributed to the lack of mesh resolution of the simulation and apparently the LES cannot resolve the steep gradients well enough. Near the end of the constriction the water surface drops further quite significantly. The flow downstream of the constriction is subjected to a large

very shallow recirculation zone just behind the abutment which contracts and accelerates the flow. The LES reproduces this part of the water surface response quite well.
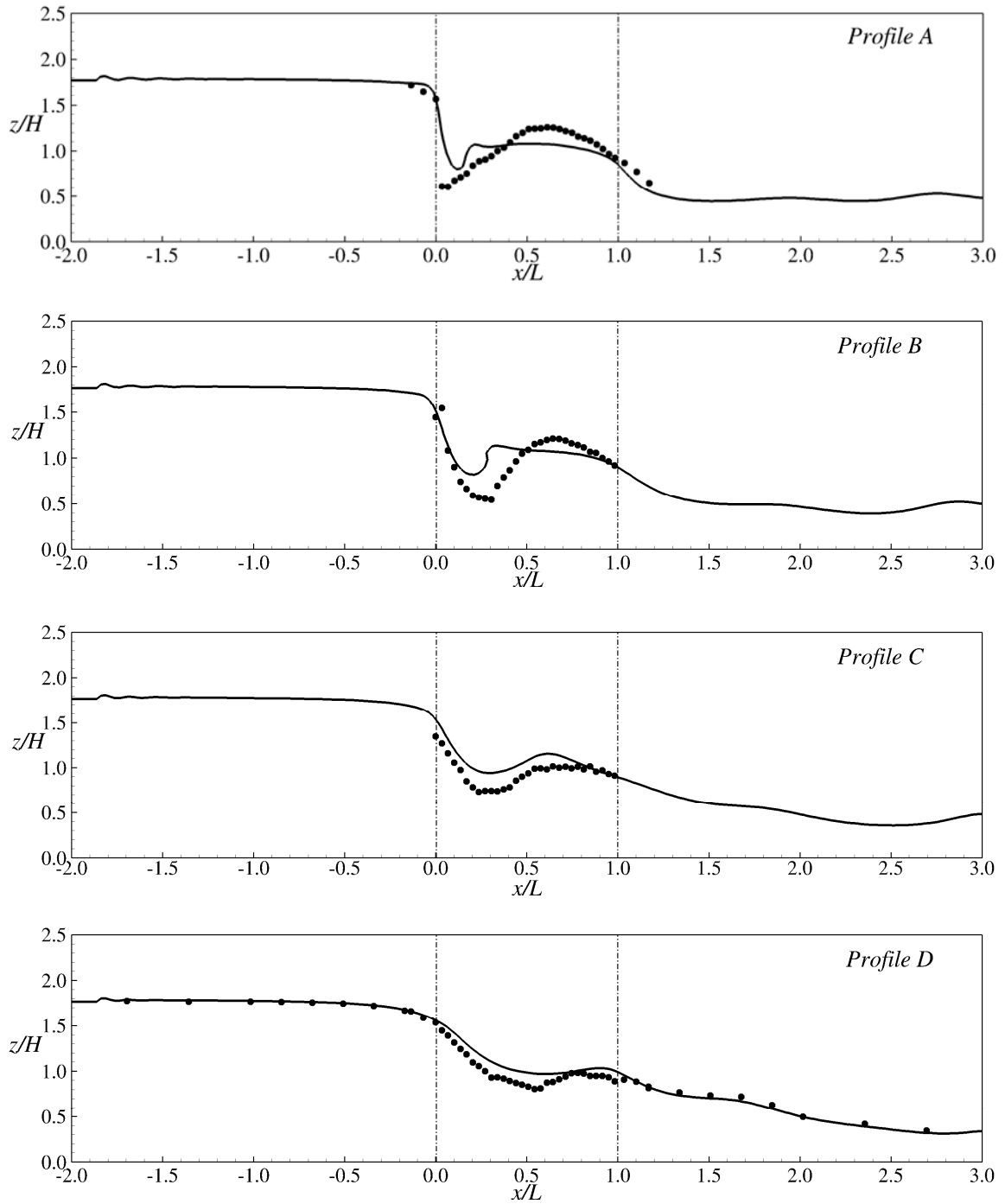
Figure 2-10 Longitudinal water surface profiles (Dots represent the experimental data. Solid black lines represent LES results)

39

The water surface features described in conjunction with Figures 2-9 and 2-10 can be observed in Figure 2-11, which depicts a photograph looking from downstream of the constriction. Afore-mentioned water surface features are highlighted in the photograph and also in the visualized large-eddy simulation. The local depression at the leading edge of the constriction is marked with a black arrow; the recovery of the depressed water in the constriction is highlighted by yellow arrows and the recirculation zone is denoted RZ. All these features are predicted well qualitatively by the LES. Moreover, there is a small ridge in the water surface between the depressed recirculation zone and the elevated flow out of the constriction, which is not picked up in the measurements (see Profiles c, d, e) but is clearly visible in the photograph and in the simulation (highlighted by a thin orange line).
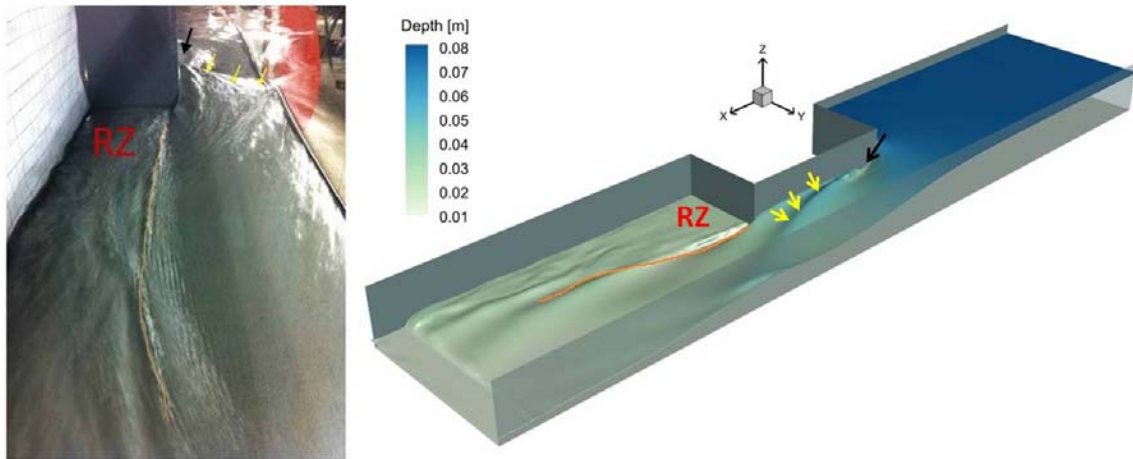
Figure 2-11 Snapshots of the instantaneous water surface from experiment and as predicted by the LES

The flow in the constriction changes its flow regime; it is supercritical for approximately 6-8L downstream of the constriction before the flow returns to subcritical

40

in a weak hydraulic jump. In the LES this happened very close to the domain exit and posed a challenging task in terms of numerical stability.

Figure 2-12 shows the horizontal vorticity contours for the horizontal plane $z/H=$ 0.17. Two necklace vortices initially parallel to the constriction in the upstream section follow the flow direction close to the structure in the constricted area. Then tails of these vortices are shed in the downstream section of the constriction.
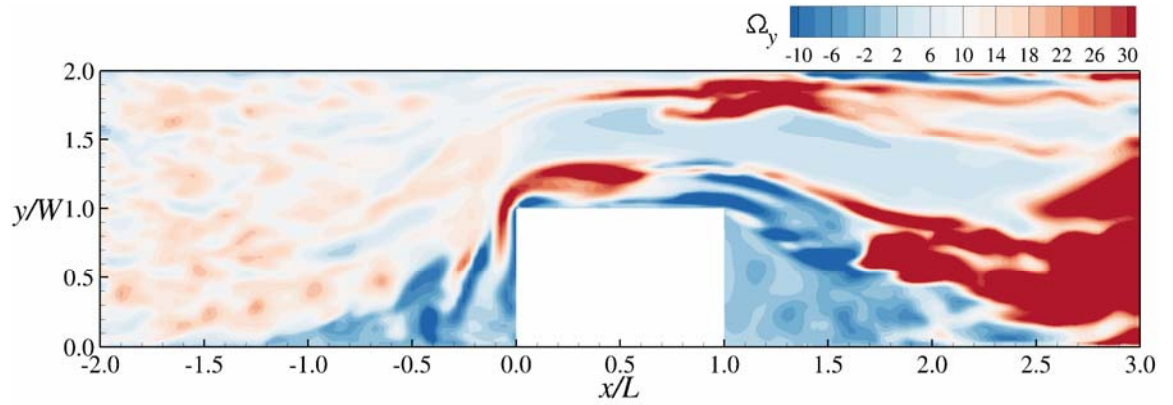
Figure 2-12 Horizontal vorticity for the horizontal plane at $z/H=$ 0.17

Figure 2-13 represents the 3D visualization of the vortical structures of the instantaneous flow using Q-criterion. All structures are colored according to their position in the vertical direction. Herein, two necklace vortices discussed for the Figure 2-12 are more identifiable on the bed around the constriction. These highly turbulent 3D vortices likely have a strong impact on the scour mechanism.
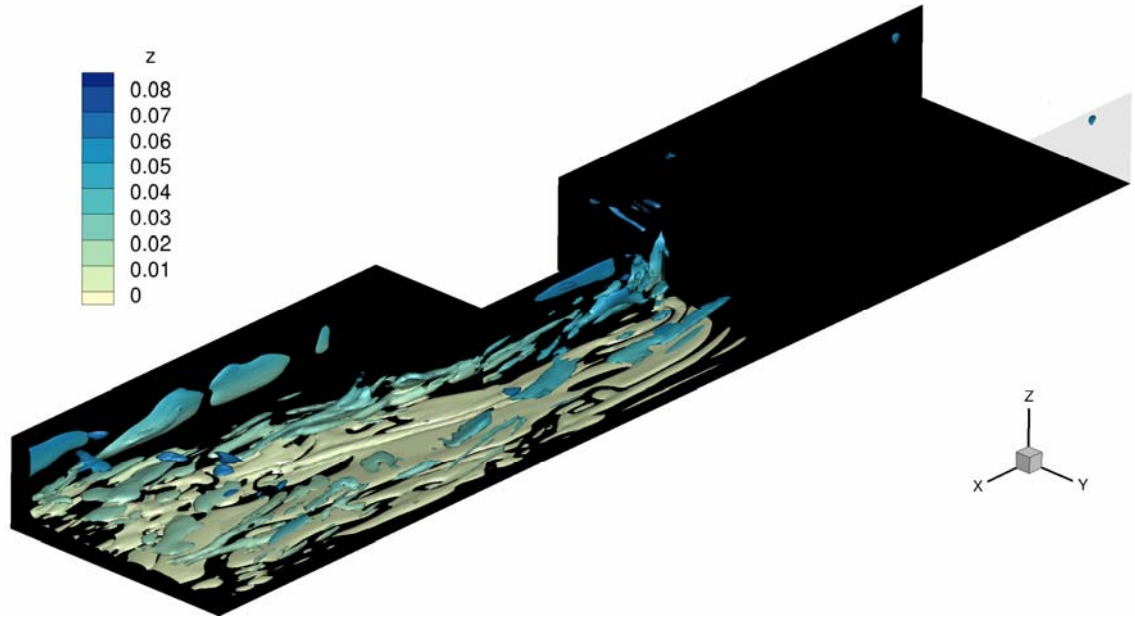
Figure 2-13 Visualization of the vortical structures of the instantaneous flow using Q-criterion

Figure 2-14 presents the normalized time-averaged streamwise velocity contours for a horizontal plane at z/H=0.17. Flow separations in the upstream and downstream sections of the constriction lead to very low mean velocity in these sections. Velocity of the flow entering the constricted area increases rapidly. Two necklace vortices having relatively lower velocities are identified around the constriction. In the downstream part, high velocity is still in the main channel section due to the shear effect of flow separation extending to the outlet.
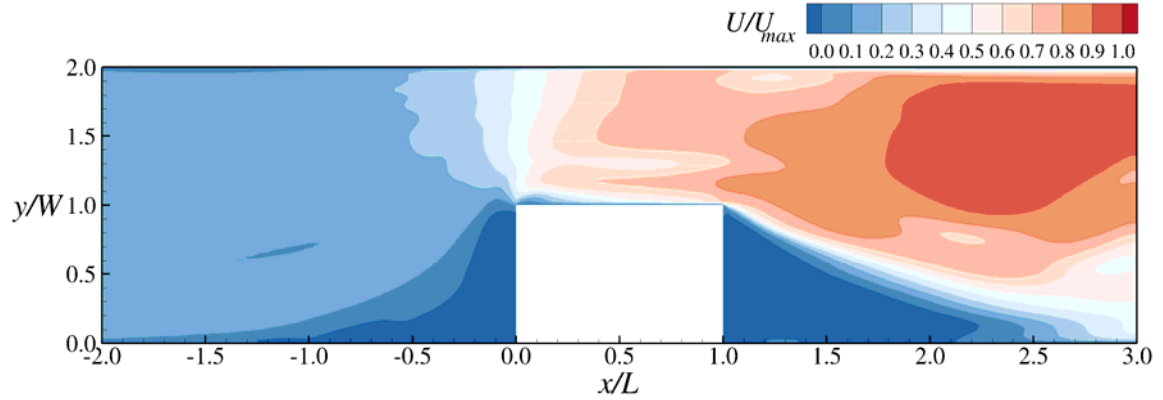
Figure 2-14 Normalized mean velocity, U/U_{max} for the horizontal plane at $z/H=$ 0.17

Figure 2-15 presents the normalized time-averaged, streamwise velocity contours for different cross-sections from the starting section of the constriction to the downstream section. In these figures, the black solid line represents the interface between water and air. For the cross-section at $x/L=0.136$, a dip in the water surface level and high velocity contours are observed very close to the constriction due to flow separation. The main necklace vortex is identified as a corner vortex at the constriction side of the abutment. Another counter-rotating necklace vortex becomes visible next to the main one for the cross-sections at $x/L=0.332$ and 0.668. It convects high momentum fluid to the corner vortex and leads to its expansion. Two opposite rotations, in the corner vortex and the main channel flow, lead to a peak point in the water surface elevations in the constriction. It is observed for the cross-section at $x/L=0.668$ that the counter-rotating vortex expands towards the corner and decreases the effects of the corner vortex on the peak water surface elevation. The cross-section at $x/L=1.5$ shows the direction of high velocity flow escaping from the constriction influence. Herein, another corner vortex is identified behind the constriction (downstream side). This corner vortex size decreases while

43

moving towards the downstream section due to the effect of flow coming from the main

channel (See the plot for the cross-section of x/L=2.5).
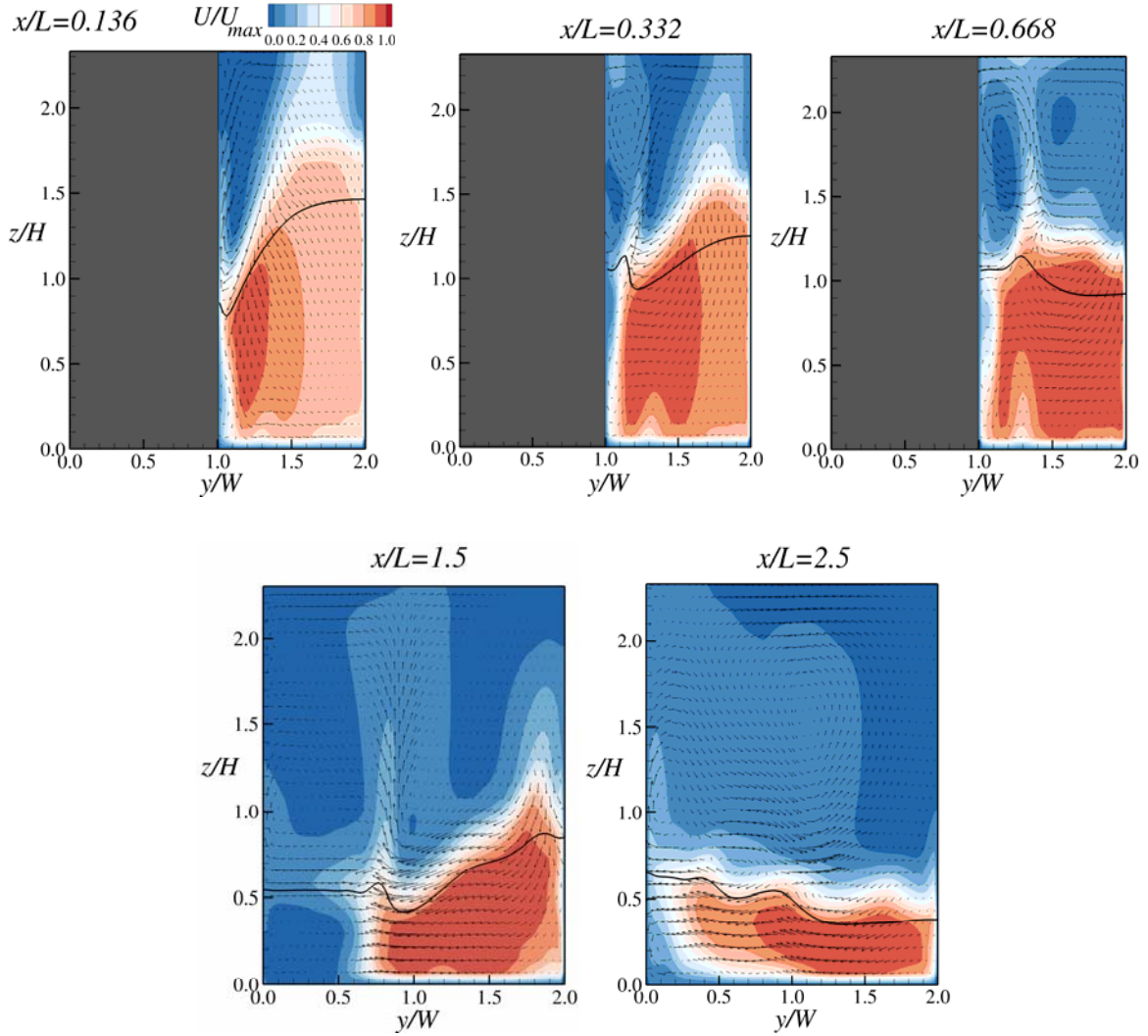
Figure 2-15 Contours of normalized time-averaged streamwise velocity, U/U_{max} for cross-sectional planes with velocity vectors showing secondary flow (looking upstream; x increases in the downstream direction)

Figure 2-16 represents *tke* contours normalized with the squared uniform-depth

shear velocity, u_*^2, for the horizontal plane at z/H= 0.17. Starting from the upstream tip of

the constriction, *tke* increases in the downstream direction. Two necklace vortices and

their tails, whose positions are identified as being very close to constriction in the flow direction have very high *tke* values. The highest value of *tke* is seen in the downstream section.
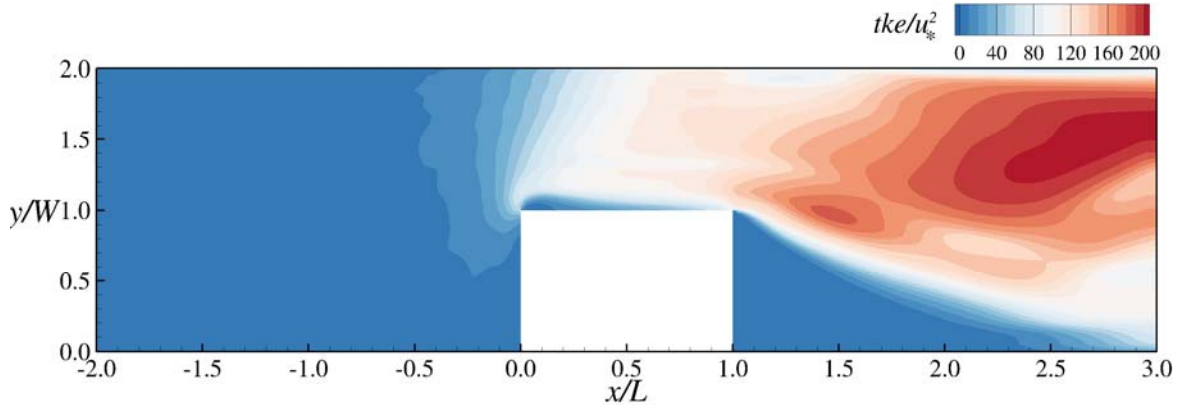
Figure 2-16 Turbulent kinetic energy contours for the horizontal plane at *z/H*= 0.17

Figure 2-17 represents the bed shear stress contours normalized with the uniform-depth integral shear stress, $\langle\tau\rangle$, for the horizontal plane at *z/H*= 0.17. The shear layer in the downstream separation region leads to higher velocity and *tke* values at the downstream main channel section. This causes the formation of the highest bed shear stress region in that area.
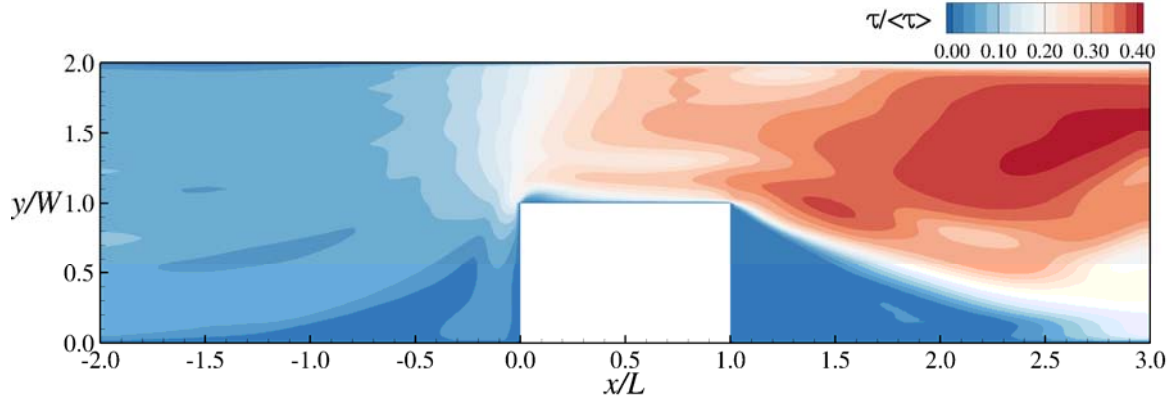
Figure 2-17 Normalized bed shear stress for the horizontal plane at z/H= 0.17

Herein, the bed shear stress due to the necklace vortices is the focus of concern. The effect of these vortices on the bed shear stress is clearly identifiable in Figure 2-17. These vortices with high turbulent kinetic energy increase the shear stresses beneath them. Their high sediment entrainment capacity likely leads to scouring around the constriction and may cause stability problems for the structure. Bed shear stresses obtained from these simulations can be used to determine the riprap sizes that will be placed around the structures to protect them from instability issues due to excessive scouring.

2.3 Parallelization

Large Eddy Simulation (LES) on such scales requires a three-dimensional computational domain with extremely high resolution. Therefore, a large amount of computer memory and computing time is necessary to run these simulations. Hence, usage of massively parallel high-performance computers is a must for these problems in three space dimensions, especially for high Reynolds numbers.

Parallelization of the present software is based on a classical domain decomposition method using the Message Passing Interface (MPI). The exchange of relevant information during the computation between different processors is obtained through one ghost cell slice as shown in Figure 2-18. As each domain has uniform grids only, the decomposition of the computational domain and the resulting communication is straightforward and can be found in Croce et al. (2004). However, the communication volume is dependent purely on the employed finite difference method. The width of the finite difference stencils employed in the software is one and three grid cells for the pressure and velocity fields, respectively. This requires attaching one slice of boundary ghost cells to each neighboring subdomain for pressure and three slices for the velocity field. These values are not directly available to the processors performing the computations. They are sent to the neighboring processors in a communication phase inside the time-stepping loop. Hence, the values for all ghost cells are communicated in the fluid solver.
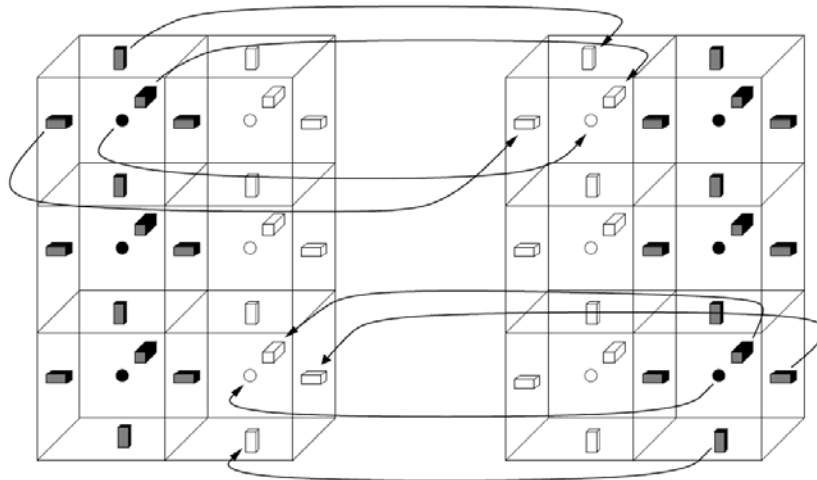
Figure 2-18 Exchange of pressure and velocity values for one ghost cell slice. White bricks denote ghost cell values and black bridges refer to subdomain values

CHAPTER 3

COMPOUND CHANNELS WITH DEEP AND SHALLOW

OVERBANK FLOWS

Compound channels consist of a main channel that carries the bank-full, more frequent discharges and a floodplain that is inundated during flood flows; this channel morphology is ubiquitous in the natural environment. Their detailed distribution of flow and turbulence properties has recently found renewed attention due to an increase in flood extent and frequency and the concomitant flood damages. In compound open channel flow, momentum transfer occurs at the interface between deep and shallow channel portions due to the prevailing cross-stream gradient in streamwise velocity and the resulting shear layer, producing additional energy losses and reducing the overall discharge capacity of the system. Further, primary (streamwise) and secondary (cross-stream) velocities, bed shear stresses and turbulence characteristics in the entire cross-section are altered (e.g. Prinos *et al*. 1985, Tominaga and Nezu 1991).

The objective of this chapter of the thesis is to use LES to examine the effects of floodplain depth on the turbulence statistics, bed- and apparent shear stress distribution, and turbulence anisotropy and subsequent streamwise vorticity generation. Comparisons are made with the data of Tominaga and Nezu (1991). In addition, the numerical results are analyzed to investigate the contributions of secondary currents and turbulence to the streamwise momentum transport. Furthermore, the high resolution numerical data are used to obtain empirical input parameters required in existing analytical models to predict the depth-averaged velocity distribution.

3.1 Computational Setup

The computational LES setup was chosen to correspond to the experiments by Tominaga and Nezu (1991), thereby allowing for the validation of sub- and super-grid modeling of the LES method for the present compound channel flows. Two different floodplain depths were considered, i.e. h/H = 0.5 and 0.25, where h is the variable floodplain depth and H the main channel depth of 0.080m. The main channel width of B =0.20 m and the floodplain width were equal, and B/H = 2.5. The Reynolds numbers **R** = $4U_bR/v$ based on the bulk velocity $U_b = Q/A$ and the hydraulic radius R were **R** = 54,500 and 45,600, respectively. Figure 3-1 shows the computational setup and the boundary conditions for h/H = 0.5. The length of the domain in the streamwise direction was 12H, i.e. nearly twice the recommended value of $2\pi H$ for straight smooth channels. This ensures the capture of all relevant large-scale turbulence structures, as confirmed by two-point correlations (not shown here). In LES, the flow is statistically homogenous in the streamwise direction and cyclic boundary conditions are employed in this direction. For smooth walls, the no-slip wall boundary condition is used. The free surface is set as a frictionless rigid lid and treated as a plane of symmetry. The computational domain is discretized with a fine uniform grid 601×161×251 grid points for the main channel and 601×81 (41 for h/H = 0.25) ×251 grid points for the flood plain in the streamwise, wall normal and spanwise directions, respectively. The grid spacing in wall units are $\Delta x^+ \approx 26$, $\Delta y^+ \approx 6$ and $\Delta z^+ \approx 13$, in which u_* is determined from the pressure gradient dp/dx driving the flow, which unambiguously provides the squared global shear velocity u_*^2. The simulation was initially run for a period of 12 eddy turn-over times ($t_e = h/u_*$) to develop the flow, and was then continued for another 23t_e to acquire flow statistics and

49

finally averaged in the longitudinal direction for a smoother distribution of the computed quantities. In addition to the smooth bed floodplains, simulations for a roughened floodplain bed (analogous to the experiments reported in Tominaga and Nezu (1991)) were studied, however the roughness was quite small, and turbulence statistics are similar to these reported herein.
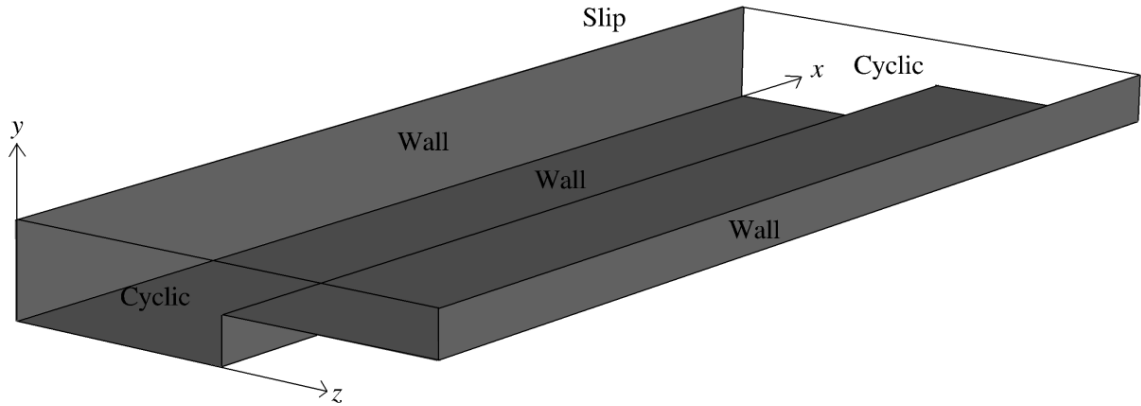
Figure 3-1 Computational setup and boundary conditions for LES

3.2 Results and Discussions

3.2.1 Time-Averaged Flow

Figure 3-2 shows vectors of the secondary flow from the LES and from the experiments of Tominaga and Nezu (1991). A vortex pair forms at the interface between the main channel and the floodplain, regardless of the floodplain depth. Overall, the agreement of the predicted vortex pairs with these measured is satisfying. The small differences in terms of location and shape of the secondary cells at the interface may be a result of measurement uncertainty (note that the secondary flow is only $\cong 5\%$ of the primary flow), LES modeling (SGS modeling, rigid lid assumption) or due to limited

flow development (finite domain in the experiment, infinite domain in the LES). Obviously, the size of the interface vortex pair is determined by the floodplain depth. The deeper the floodplain flow depth, the larger the floodplain vortex occupying the entire floodplain depth, and the larger the vortex in the main channel. The experiments did not resolve the secondary vortices forming in the channel corners; however, LES provides a good overall picture of the entire secondary flow in the cross-section.

The main channel vortex size at the interface controls the size of the counter-rotating corner vortex underneath. For $h/H = 0.25$ the main channel vortex at the interface is flat and the corner vortex is considerably larger than for the $h/H = 0.5$ case. A counter-rotating vortex pair is also observed on the left hand side of the main channel. It is asymmetric with respect to the corner bisector and the free-surface vortex is located on top of the corner vortex. This is a result of the mixed boundary condition at the free surface corner. The size of the free surface vortex in the main channel is identical in both cases; hence the floodplain depth does not affect the secondary flow near the left sidewall. In addition to the secondary vectors, contours of streamwise vorticity are plotted in Fig. 3-2. The color-coding was chosen to highlight only areas of significant positive (red) and negative (blue) streamwise vorticity. The overall distribution is similar for the two flows, and vorticity magnitudes are greatest in the channel corners and at the interface vicinity, where the secondary currents are generated (as shown below). There are areas of increased vorticity near the channel walls and the water surface, where the vertical velocity is reduced to zero over a short distance.
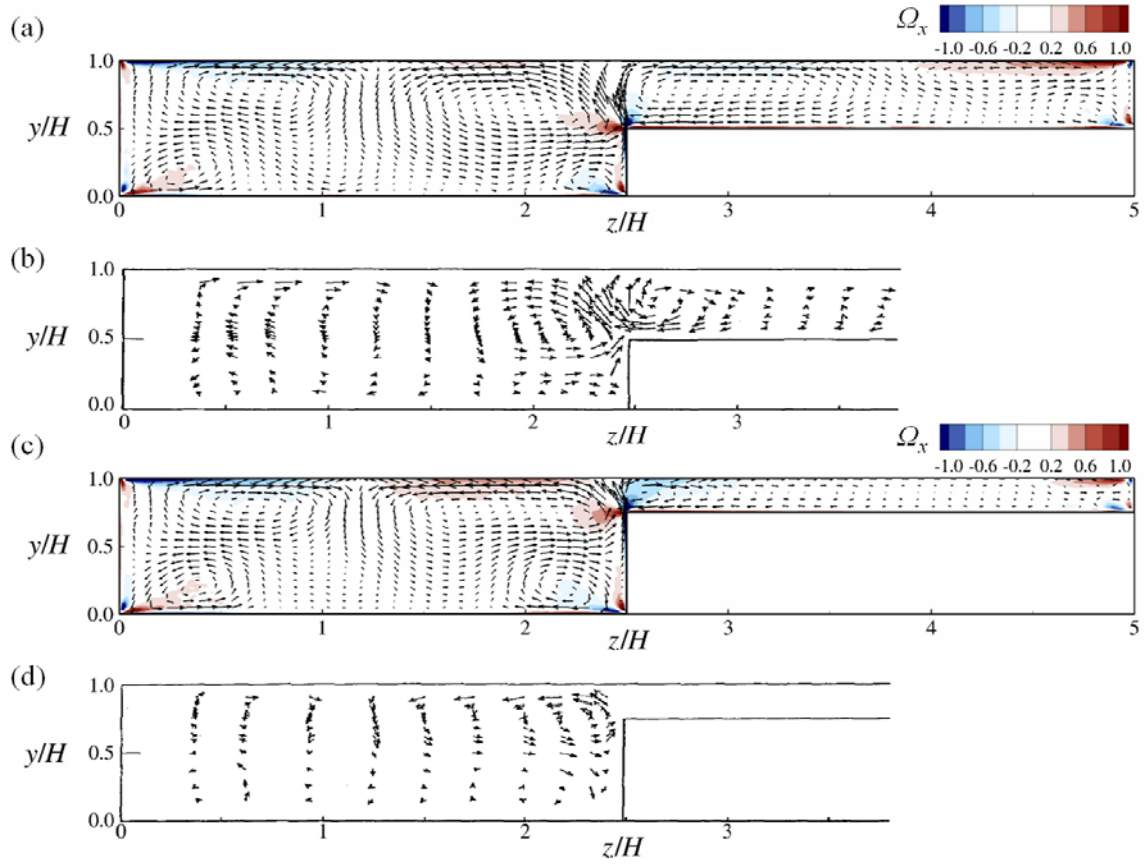
Figure 3-2 Streamwise vorticity Ω_x and secondary current velocity vectors for (a) LES, (b) experiment for h/H=0.5, (c) LES, (d) experiment for h/H=0.25. Experimental results from Tominaga and Nezu (1991)

Figure 3-3 shows simulated and measured isotachs of the time-averaged primary velocity U, normalized with the maximum streamwise velocity U_{max}. The LES predictions agree well with the experiments, especially in the main channel. However, the LES slightly underestimates the velocities on the floodplain, probably due to insufficient flow development in the experiment. There is a substantial velocity gradient between main channel and floodplain flows, with a steeper gradient in the shallow floodplain case than in the two deeper floodplain cases. The primary velocity is influenced strongly by

the prevailing secondary currents, most visibly in the contour lines of the primary velocity close to the interface where they bulge at an inclined angle from the floodplain corner toward the free surface in the main channel. This velocity bulge is more pronounced in the deep floodplain cases, because the angle of inclination of the secondary vectors is smaller in the deep than in the shallow floodplain flow.

The second important influence of secondary currents on the streamwise velocity is the velocity dip in the main channel, i.e. the shift of location of the maximum velocity below the water surface. This is due to secondary currents convecting low momentum fluid at the surface toward the channel center while its high-momentum fluid is transported toward the bed. The contours of the primary flow also bulge in the direction of the three main channel corners by the prevailing corner vortices. The flow near the free surface corner of the main channel is decelerated visibly, resulting from side wall fluid convected to the surface by the corner vortex. These phenomena are well predicted by the LES.

(a)

(b)

(c)

(d)
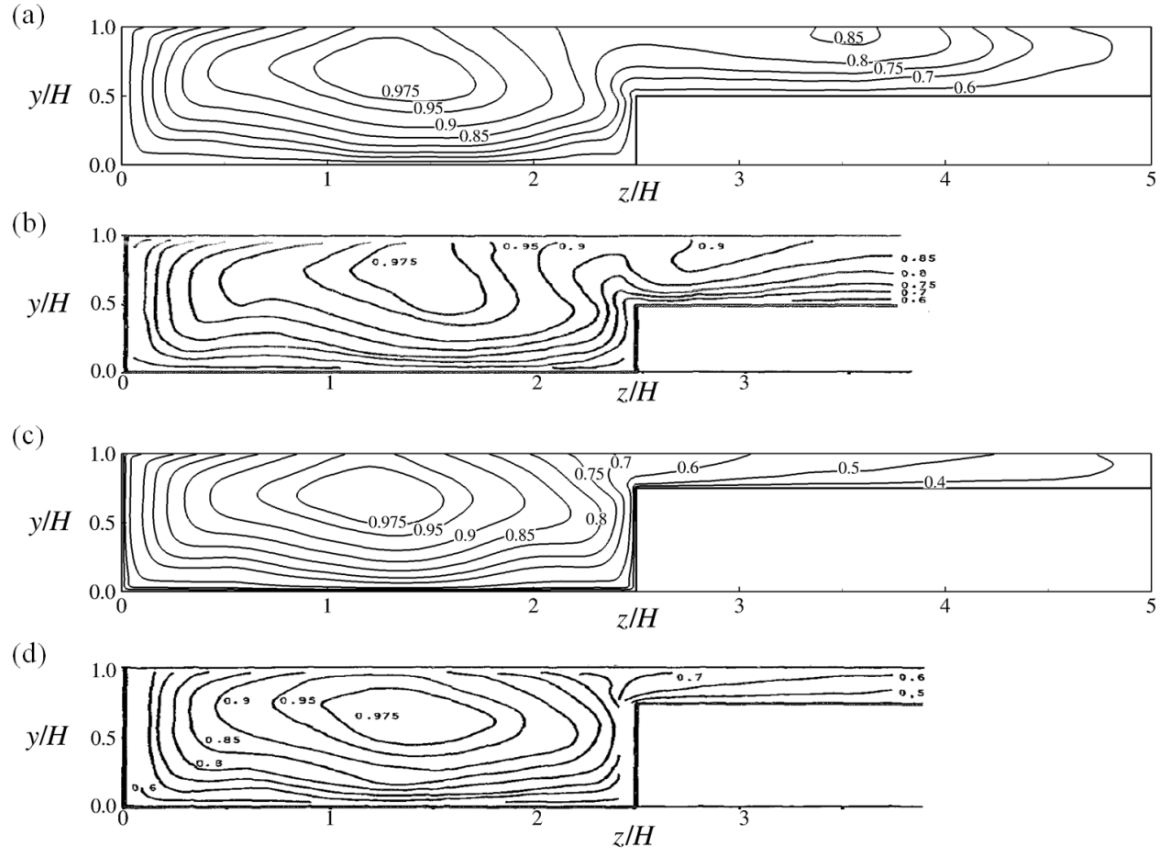
Figure 3-3 Contours of time-averaged streamwise velocity U/U_{max} (a) LES, (b) experiment with h/H=0. 5, (c) LES, (d) experiment with h/H=0.25. Experimental results from Tominaga and Nezu (1991)

3.2.2 Shear Stresses

Figure 3-4 shows contours of the normalized primary shear stress $-u'v'/u_*^2$, the normalized spanwise shear stress $-u'w'/u_*^2$, and the normalized cross-plane shear stress $-v'w'/u_*^2$. For the sake of brevity, only the $h/H = 0.25$ case is discussed. Also plotted are vectors of the secondary flow to illustrate the strong interconnection between shear stresses and secondary currents. The primary shear stress $-u'v'$ peaks near the bed and the largest values occur in the main channel. The black line indicates changes of sign of

$-u'v'$ indicating that there is a relatively large area of negative primary shear stresses near the water surface. This is a result of the secondary-current driven velocity dip producing negative wall-normal primary velocity gradients, i.e. dU/dy. The effect of floodplain depth is significant, especially at the interface of the main channel and the floodplain. There, an area of strong negative shear occurs, which indicates that quadrant I (i.e. outward interaction) and III (inward interaction) turbulent events dominate the shear stress. The primary stress on the floodplain is markedly smaller in the shallow floodplain flow. The distribution of the secondary or spanwise shear stress $-u'w'$ exhibits high values near the side wall of the main channel, but also near the interface. The magnitude of $-u'w'$ is of the same order as $-u'v'$. This provides quantitative evidence that the interface acts as a virtual (permeable) wall, with considerable momentum transfer caused by turbulence and secondary currents. The fact that the wall is permeable results in momentum transfer that exceeds the shear at the sidewalls, because at the interface the spanwise velocity does not decrease to zero as at an impermeable wall. The increased interfacial shear stress leads to a reduction of discharge capacity of compound channels.

This effect is further quantified and discussed below. Note that the interfacial shear stress $-u'w'$ does not extend substantially across the interface, which is discussed in the context of Fig. 3-6. The shape of the contours of $-u'w'$ for $h/H = 0.5$ (not discussed) are skewed at an angle toward the free surface, indicating that convective transport of streamwise momentum due to secondary currents affects the turbulent transport.

The cross-plane shear stresses $-v'w'$ attain local extremes of only some 10% of the squared global shear velocity in the channel corners and the junction area. Knowledge of the distribution and magnitude of the cross-plane stress is important because it

contributes to the generation of secondary currents, term C in Eq. (3-3). Maxima are associated with the location where secondary currents originate; however, the main contribution to the generation of secondary currents is due to turbulence anisotropy of the normal Reynolds stresses, whose order of magnitude are higher than $-v'w'$ (Fig. 3-10). Their magnitude and distribution are similar among the two cases.
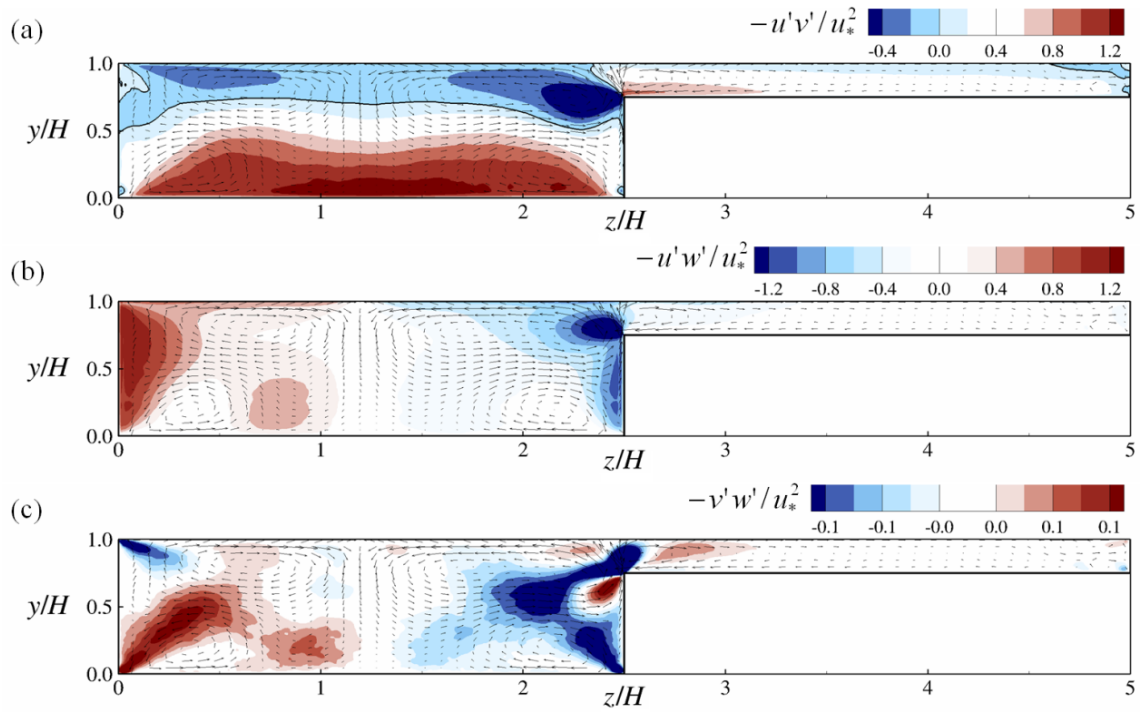
Figure 3-4 Distribution of normalized (a) primary $-u'v'$, (b) spanwise $-u'w'$, and (c) cross-plane $-v'w'$ shear stresses for shallow floodplain flow

3.2.3 Lateral Distributions

The lateral distribution of normalized, depth-averaged streamwise velocities U_d/U_b for the two cases is shown in Fig. 3-5. In addition to the LES data, model predictions using the SKM are plotted, for which a number of empirical input parameters

are required, i.e. bed friction factor f, dimensionless eddy viscosity coefficient λ and a secondary flow parameter Γ. The latter two require calibration (or reliable estimates) for the method to produce accurate predictions. In this study, the spatially-rich LES data were used to provide estimates of the empirical input parameter λ. Two distributions of the SKM predictions are plotted. For the SKM1 calculation, f was estimated from the Darcy-Weisbach equation for a smooth channel; further $\lambda = 0.07$ was selected, which is referred to as the standard value (Tang and Knight 2008), and Γ was within their recommended range. For the SKM2 distribution the friction factor was kept unchanged; the λ value was estimated from the LES data (Fig. 3-6 and Table 3-1); and Γ was then adjusted to provide the best fit to the LES-calculated depth-averaged streamwise velocity distribution. All selected and computed input parameters for SKM1 and SKM2 are provided in Table 3-1.

The discontinuity of depth-averaged velocity at the interface is an artifact of the averaging process for this specific compound channel geometry, because different depths occur on either side of the vertical interface. This discontinuity disappears for natural geometries. Regardless of these differences, important conclusions can be drawn. For SKM1, it appears that the 'standard' value of $\lambda = 0.07$ is too high (Fig. 3-6), in particular for the main channel and at the interface, leading to a SKM-computed velocity gradient that is significantly less steep than the one from LES. The lateral distribution of the depth-averaged primary velocity, using standard values, differs therefore markedly from that computed by LES, irrespective of the floodplain depth. The LES data were further analyzed to compute explicitly the lateral eddy viscosity parameter using dU/dz and $-u'w'$. For the cases investigated herein, the λ value calculated by LES is almost an order

of magnitude smaller than the 'standard' SKM value (Table 3-1) for both cases. As a result of λ adjustment, the SKM2 distribution in comparison with SKM1 agrees better with the simulation data; in particular, the gradients at the main channel sidewall and at the interface match better to the LES data. However, Γ had to be adjusted outside the range found in previous studies (e.g. Tang and Knight 2008), demonstrating the empiricism involved in estimating Γ.
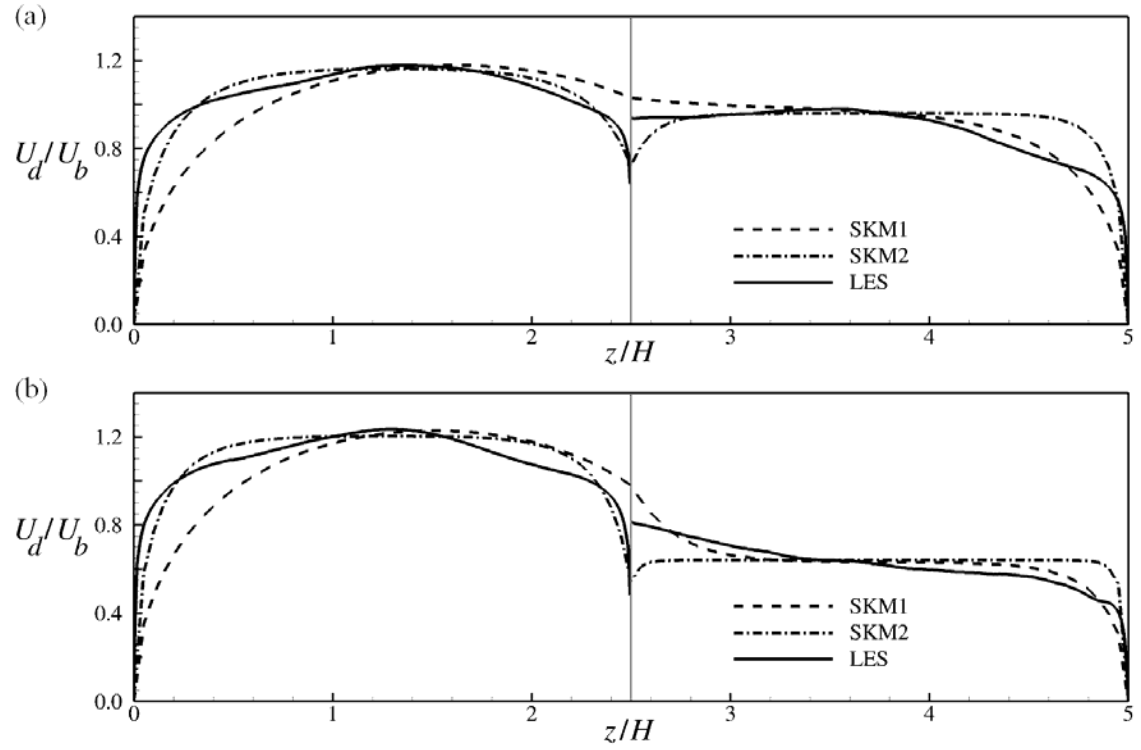
Figure 3-5 Lateral distribution of depth-averaged velocity calculated by LES and predicted using SKM for (a) $h/H = 0.50$, (b) $h/H = 0.25$

Figure 3-6 shows LES results for the lateral distributions of U/U_{max}, normalized spanwise shear stress $-u'w'/u_*^2$, spanwise velocity gradient dU/dz, and the resulting λ values taken at half of the floodplain depth. Here, only data of the shallow floodplain flow case are shown, because they are similar for the deep floodplain flow case. The above-mentioned feature, i.e. elevated interfacial shear stress $-u'w'$, that decreases abruptly at the interface is substantiated in Fig. 3-6 and results from the sudden decrease in velocity gradient right at the interface ($z/H = 2.5$). The lateral eddy viscosity parameter remains constant in the main channel with $\lambda \approx 0.0035$, peaks at the interface, and gradually decreases on the floodplain. The case $h/H = 0.5$ is similar but not shown, and λ in the main channel is fairly constant with $\lambda = 0.006$, but an order of magnitude lower than the 'standard' value.
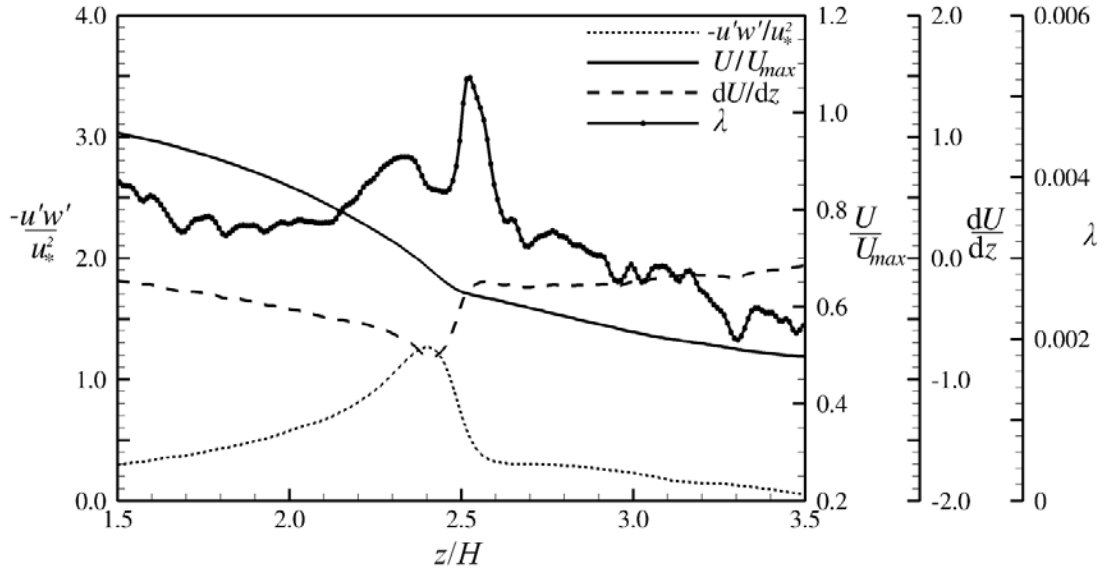
Figure 3-6 Spanwise profiles of U/U_{max}, normalized spanwise shear stress $-u'w'/u_*^2$, spanwise velocity gradient dU/dz, and resulting lateral eddy viscosity parameter λ near interface for $h/H = 0.25$

Table 3-1 Input parameters used for the computation of depth-averaged velocity distribution using the SKM

CASE	Friction factor f		Eddy viscosity λ		Secondary currents Γ	
	Main channel	Floodplain	Main channel	Floodplain	Main channel	Floodplain
SKM1:*h/H*=0.5	0.0196	0.0224	0.070	0.070	0.3	-0.20
SKM2:*h/H*=0.5	0.0196	0.0224	0.006	0.006	1.7	-0.05
SKM1:*h/H*=0.25	0.0198	0.0283	0.070	0.070	0.1	-0.01
SKM2:*h/H*=0.25	0.0198	0.0283	0.004	0.004	2.0	-0.05

Figure 3-7 shows the lateral distributions of calculated normalized bed-shear stress for the two cases. Also plotted are the experimental data of (Tominaga and Nezu 1991). The advantage of a wall-resolved LES, as is the case here, is that for the smooth walls the local bed-shear stress can be calculated exactly with the predicted time-averaged primary velocity at the first grid point using the viscous stress formula (e.g. Nezu and Nakagawa 1993). The local bed-shear stress is normalized with the spatially-averaged bed-shear stress of the entire wetted perimeter $< \tau >$. The LES-calculated bed-shear stresses in the main channel, obtained from the viscous stress formulation, are similar to the experimental values in terms of their magnitudes, especially in the main channel. Although the vertical distribution of the primary flow is influenced by secondary currents, it is obvious that for $h/H = 0.5$ the use of the log-law (as done in the experiment) to predict the wall shear stress seems to work reasonably well. However, the use of the log-law can lead to erroneous predictions, particularly in areas where the primary velocity deviates from a logarithmic distribution, explaining differences between measured and observed values. Clearly, on the floodplain and close to the interface for $h/H = 0.25$, LES (using the viscous formulation) predicts consistently higher the shear

stresses than the experiment. There, applying the log-law to the experimental data may not provide reliable shear stress predictions. Regardless of the case, there is a significant discontinuity of bed shear stresses at the interface between main channel and floodplain with the bed-shear stress substantially greater on the floodplain side than on the main channel side. This is attributed to the water depth discontinuity at the interface (i.e. the compound channel geometry); however, it is also a result of the floodplain interface vortex, which transports high momentum fluid from the free surface to the bed. As a result of this mechanism, there are elevated levels of wall normal turbulent shear stress at the floodplain bed in the vicinity of the interface (Fig. 3-4a). Note that the bed-shear stresses close to the interface on the floodplain side are of the same magnitude as the maxima observed in the main channel, even for the shallow floodplain flow.
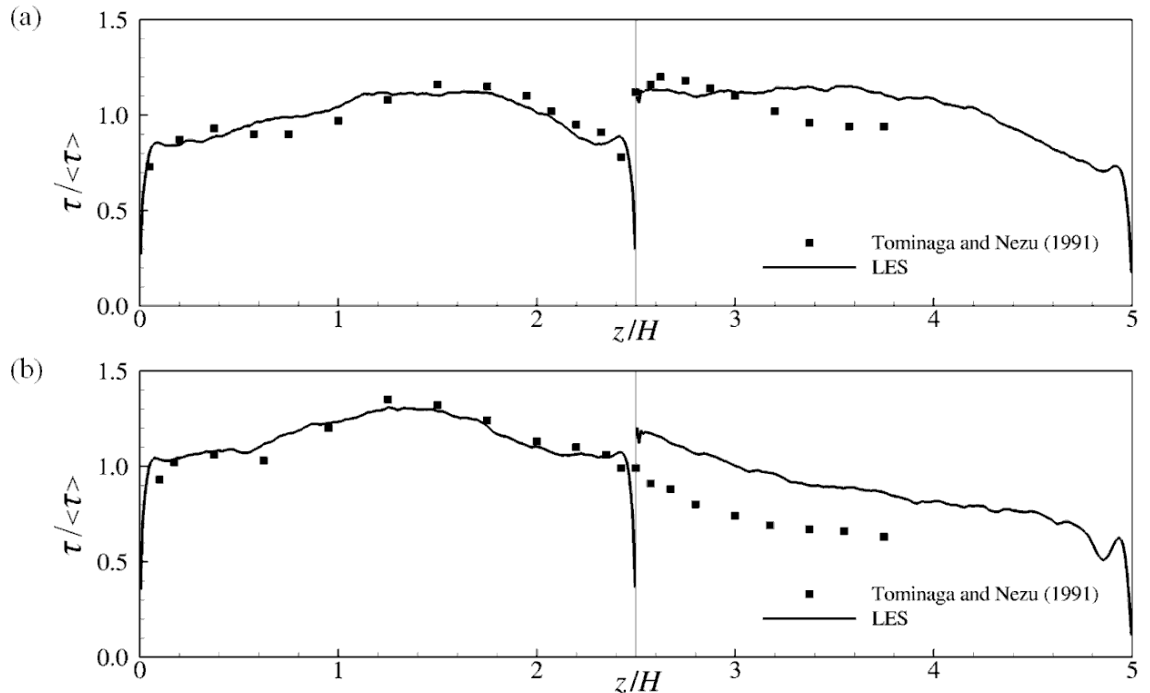
Figure 3-7 Spanwise distribution of dimensionless bed-shear stress ($\tau / <\tau>$): (a) $h/H = 0.50$, (b) $h/H = 0.25$ (gray vertical line is main channel-floodplain interface)

3.2.4 Momentum Balance and Apparent Shear Stress

To examine the terms contributing to the lateral momentum transport, the streamwise momentum equation for fully-developed open channel flow is

$$V\frac{\partial U}{\partial y}+W\frac{\partial U}{\partial z} = gS_0 + \underbrace{\frac{\partial(-u'v')}{\partial y}+\frac{\partial(-u'w')}{\partial z}}_{R_{uv}+R_{uw}}+\underbrace{(\nu+\nu_{SGS})\left(\frac{\partial^2 U}{\partial y^2}+\frac{\partial^2 U}{\partial z^2}\right)}_{Viscous} \tag{3-1}$$

$$\underbrace{\phantom{V\frac{\partial U}{\partial y}+W\frac{\partial U}{\partial z}}}_{A_v+A_w}$$

where A_v and A_w are the advection terms due to secondary currents, R_{uv} and R_{uw} are the primary and spanwise Reynolds stress terms and *Viscous* corresponds to the viscous term, which is negligible except extremely close to the wall.
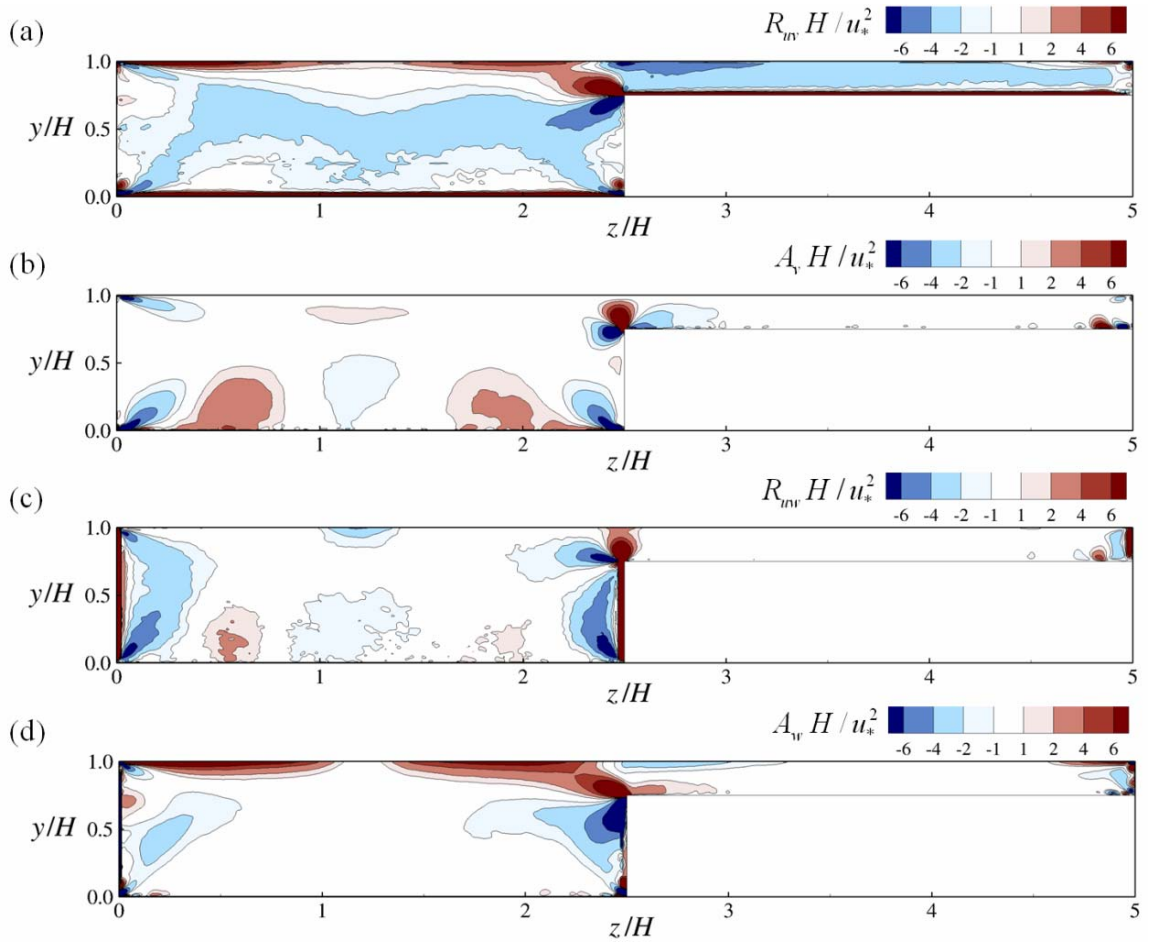
Figure 3-8 Magnitude of terms in streamwise momentum equation for *h/H*=0.25

Figure 3-8 provides the magnitudes of the terms in the momentum equation for the smooth channel with $h/H = 0.25$, and the shallow floodplain case, with the deep floodplain flow exhibiting similar features. The contour colors are selected so that small contributions are invisible and only major contributions to the streamwise momentum transport are visualized. Close to the bed and the sidewalls, the turbulent components R_{uv} and R_{uw} attain their peak values and contribute to the streamwise momentum transfer by virtue of the walls and are mainly balancing the gravity term. Figure 3-8 demonstrates the importance of secondary currents on the streamwise momentum, which is expressed by the fact that all four terms are of the same order of magnitude in locations where the secondary currents originate, i.e. at the main channel corners and, in particular, close to the interface. At the interface, the vertical and spanwise convective transport A_v and A_w are balanced by wall-normal and spanwise turbulent transport (R_{uv}, R_{uw}). At the free surface, the spanwise convective transport A_w is compensated for by turbulent transport by the wall normal primary shear stress R_{uv}. Due to the two large secondary cells in the upper half of the channel, low momentum fluid is transported to the free surface from the sidewall and the junction toward the channel center. This transport is balanced mainly by turbulent fluctuations (i.e. through R_{uv}) in inward or outward motions (i.e. $u' < 0$, $v' > 0$ and $u' > 0$, $v' < 0$), leading to positive shear stresses and to negative streamwise velocity gradients.

Integrating Eq. (3-1) over the water depth yields the depth-averaged momentum equation for fully-developed open channel flow as (Shiono and Knight 1991):

$$\frac{\mathrm{d}}{\mathrm{d}z}\underbrace{\int UW\mathrm{d}y}_{J} + \frac{\mathrm{d}}{\mathrm{d}z}\underbrace{\int u'w'\mathrm{d}y - \int (v + v_{SGS})\left(\frac{\mathrm{d}U}{\mathrm{d}z} + \frac{\mathrm{d}W}{\mathrm{d}x}\right)\mathrm{d}y}_{T} + \frac{\tau_b(z)}{\rho} = gS_o h(z) \qquad (3\text{-}2)$$

in which τ_b is the local bed-shear stress, ν_{SGS} the sub-grid viscosity and the term on the right-hand side represents the gravity term. The term T represents the turbulent diffusive transport and J quantifies the secondary flow transport, while $T+J$ is also called the apparent shear stress that results from the total lateral transport of streamwise momentum. This equation is used to quantify the relative contributions of secondary currents and transverse shear stresses in comparison to the gravity term.

Figure 3-9 shows the spanwise distribution of turbulent diffusive transport, secondary flow transport and the sum of the two, which is the total lateral momentum transport, normalized by the global shear velocity for the two cases. In the main channel, most of the lateral transport is due to turbulent diffusion, peaking near the interface. The total lateral transport profile has a constant slope in the main channel and it changes sign at $z/H \cong 1.2$ for $h/H = 0.5$. For the shallow floodplain case, the total lateral transport distribution features a steeper slope than the deep floodplain case and it changes sign already at $z/H = 1.1$, suggesting increased spanwise momentum transfer for the shallow floodplain flow. This is due to increased shear at the interface as a result of larger spanwise gradients of the primary velocity (quantified in Fig. 3-6). Interestingly, not only the turbulent shear component T is greater in the $h/H = 0.25$ case but also the J component. As already discussed in the context of Fig. 3-6, the turbulent stress drops almost to zero right at the interface, i.e. at $z/H = 2.5$, and as a result, on the floodplain the majority of the apparent shear stress is comprised of the secondary flow term except close to the side wall of the floodplains. On the main channel side of the interface, the turbulent shear is the dominant contributor to apparent shear stress. The total lateral transport profile is linear but asymmetric with respect to the main channel center line due to the

interfacial shear, and a change of sign occurring for $z/H < 1.25$ indicates that the shear at the interface is greater than that at the main channel side wall.

(a)

(b)
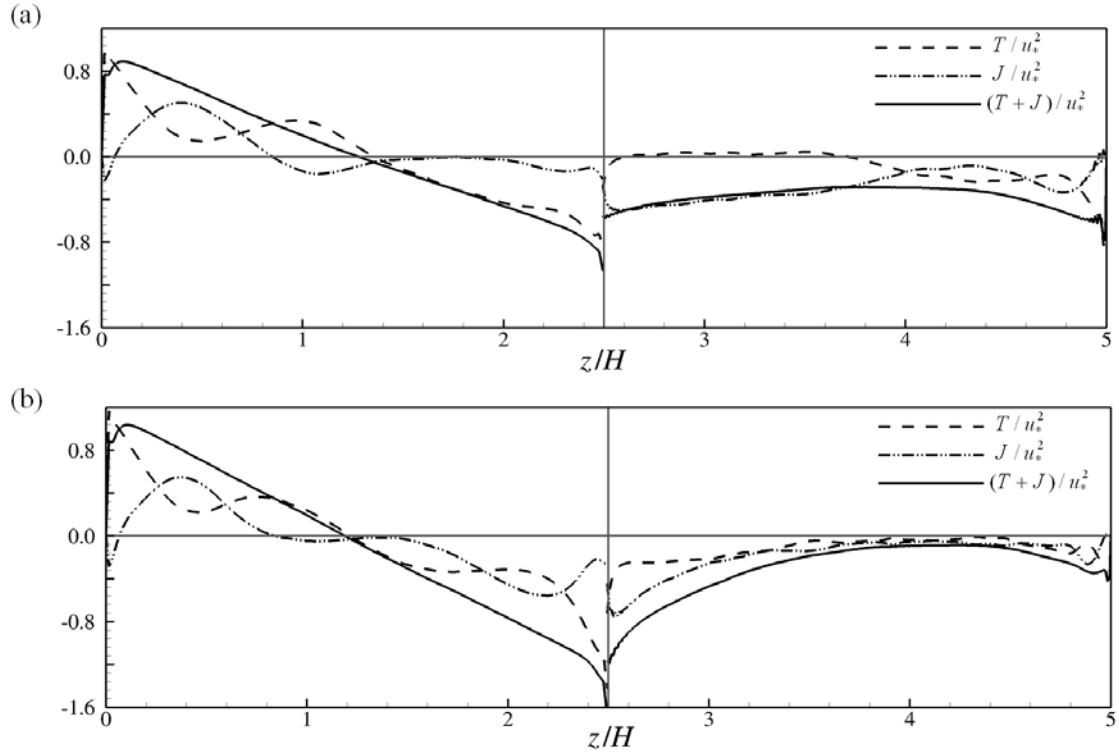
Figure 3-9 Spanwise distribution of apparent stress T and J: (a) $h/H = 0.5$, (b) $h/H = 0.25$ (grey vertical line represents main channel–floodplain interface)

3.2.5 Origin of Secondary Currents

The origin of secondary currents was explained already by Prandtl (1925) who suggested that the secondary motion in straight channels is caused by the anisotropy of turbulence. To describe the origin of turbulence-driven secondary currents, the streamwise vorticity equation for steady, incompressible, uniform and turbulent flow in a straight channel has the exact form (Nezu and Nakagawa 1993)

$$V\frac{\partial\Omega_x}{\partial y} + W\frac{\partial\Omega_x}{\partial z} = \underbrace{\frac{\partial^2}{\partial y\partial z}\left(w'^2 - v'^2\right)}_{B} - \underbrace{\left(\frac{\partial^2}{\partial z^2} - \frac{\partial^2}{\partial y^2}\right)v'w'}_{C} + \underbrace{v\left(\frac{\partial^2\Omega_x}{\partial y^2} + \frac{\partial^2\Omega_x}{\partial z^2}\right)}_{D} \tag{3-3}$$

in which the streamwise vorticity is defined as

$$\Omega_x \equiv \frac{\partial V}{\partial z} - \frac{\partial W}{\partial y} \tag{3-4}$$

Term A in Eq. (3-3) represents the convection of streamwise vorticity by the mean flow and D the viscous diffusion of Ω_x. Terms B and C are generation of streamwise vorticity terms and both involve turbulent Reynolds stresses. The origin of secondary currents was argued amongst researchers; Broglia *et al.* (2003) provided evidence that in straight and narrow open channels the turbulence anisotropy of the normal stresses (i.e. $w'^2 - v'^2$) term dominates the secondary shear stress term. Figure 3-10(a,b) shows contours of $(w'^2 - v'^2)$ normalized by the squared shear velocity for the deep and shallow floodplain cases. The turbulence anisotropy levels are of considerable magnitude, and exhibit local extremes, respectively, near the walls, the free surface and particularly near the interface. For compound channels, the anisotropy at the interface leads to the formation of the vortex pair. Generally, $(w'^2 - v'^2)$ values are an order of magnitude greater than the cross-plane shear stresses (Fig. 3-4). In addition, in the channel corners and particularly at the main-channel–floodplain-junction, $(w'^2 - v'^2)$ are of opposite sign, indicating that the cross-partials are of significant magnitude. This is further quantified and confirmed in Fig. 3-10(c,d), where the normalized generation term, i.e. term B in Eq. (3-3), is quantified. Extremes are found on either side of the interface, underlining the significance of the turbulence normal stress anisotropy there. The generation term is more significant at the interface of the shallow floodplain case, where the peak values extend all the way to the

free surface, suggesting that the angle of inclination of secondary currents depends on the extent and magnitude of the secondary current generation term. There are also elevated levels of the generation term in the wall corners of the main channel and the floodplain and in the wall-free-surface corners, supporting that secondary currents originate in channel corners.
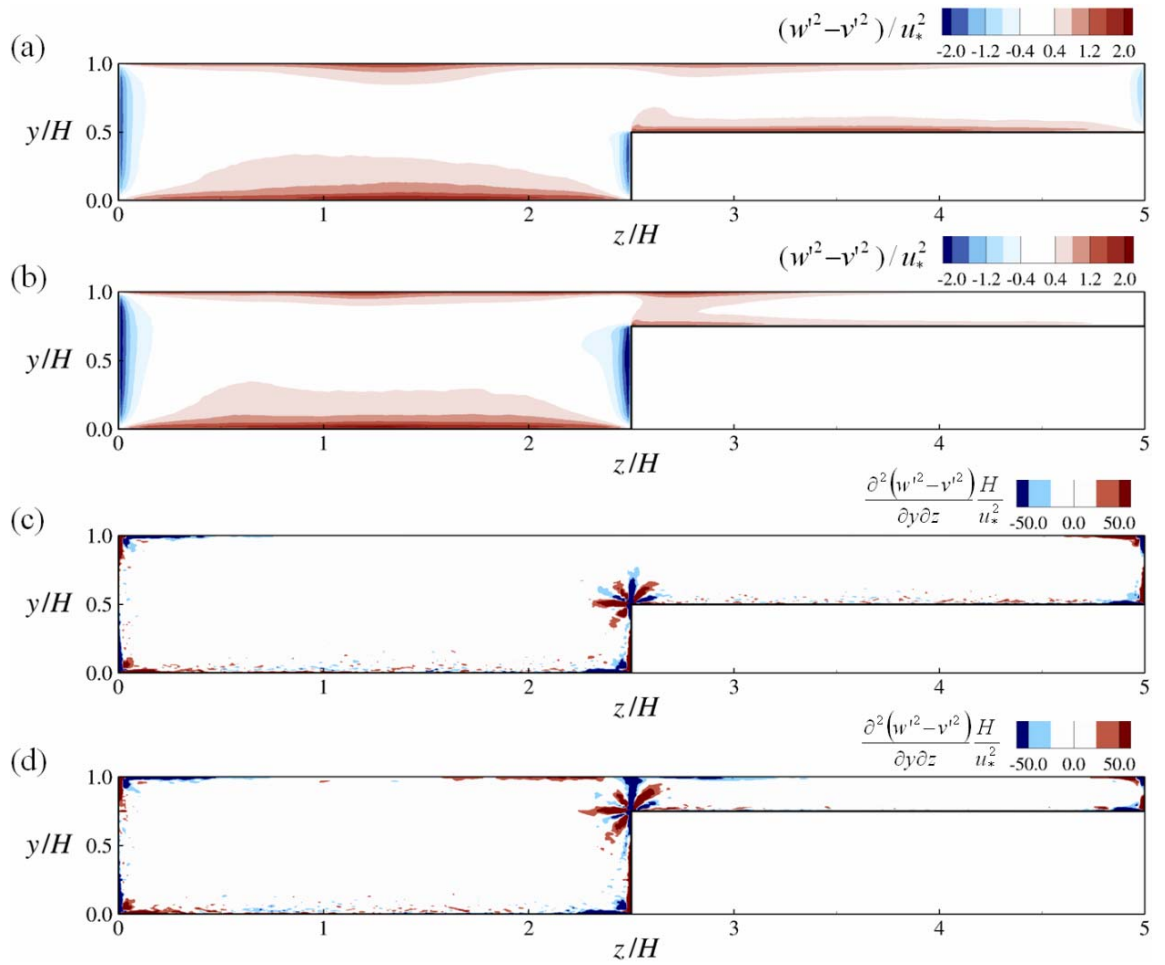
Figure 3-10 Contours of $(w'^2 - v'^2)$ normalized by squared shear velocity for deep and shallow floodplain cases (a) $h/H = 0.50$, (b) $h/H = 0.25$; and contours of normalized generation terms of streamwise vorticity (c) $h/H = 0.50$, (d) $h/H = 0.25$

3.2.6 Conclusions

The results of Large Eddy Simulations of turbulent flow in compound open channels of different floodplain depths are presented. The effects of floodplain to main channel water depth ratio on the primary and secondary flows, the second-order turbulence statistics and the anisotropy of turbulence and subsequent secondary current generation are investigated. Experimental data were used to validate the Large Eddy Simulations. Overall a good agreement between the measured and simulated data was obtained, confirming the accuracy of the method for these flows. A counter-rotating vortex pair with horizontal axes aligned with the primary flow was observed at the main channel-floodplain interface. These vortices produce a velocity bulge at the main channel-floodplain interface. As a result of secondary currents, significant spanwise Reynolds stresses occur, which are of the same order of magnitude as the primary Reynolds stress. Both secondary currents as well as primary and secondary Reynolds stresses contribute to the streamwise momentum transport. At the interface, convective momentum transport is, in large parts, balanced by transport due to turbulence; nonetheless, when depth-averaged a considerable stress contribution, the apparent shear stress, is found to take effect at the interface. The apparent stress is greater in the shallow floodplain case, resulting from a larger streamwise velocity gradient in comparison with the other case caused by both turbulent diffusion and secondary currents in the main channel and floodplain. Comparisons of the Large Eddy Simulations results with an analytical solution of the depth-averaged streamwise momentum equation illustrate that the analytical approaches to the problem require specific calibration of the lateral eddy viscosity coefficient and the secondary current parameter as a function of the compound

channel geometry and its roughness properties. It is also demonstrated from the evaluation of the terms of the streamwise vorticity equation that anisotropy of the normal Reynolds stresses dominates the effect of the cross-plane shear stresses with respect to the origin of the secondary currents.

CHAPTER 4

FREE SURFACE VS. RIGID LID LES COMPUTATIONS FOR

BRIDGE ABUTMENT FLOW

Bridge abutments are bluff obstacles in open channel flow and they trigger a highly turbulent flow field including 3D complex coherent structures (e.g. Koken and Constantinescu, 2009). These energetic coherent structures possess high sediment entrainment capacity which increases scouring around abutments and can cause bridge failure. There are quite a few experimental and numerical studies investigating the hydrodynamics and scour mechanism around bridge abutments in the literature. Most of the numerical studies in the literature rely on the rigid lid assumption for the free surface of flow around bridge abutments, however very close to the leading edge of the abutment the flow undergoes significant acceleration and the water surface drops appreciably locally. This study investigates the validity of the rigid lid assumption for such flows by comparing the results of two separate high-resolution large-eddy simulations of the flow around an abutment. The first simulation employs the rigid lid boundary condition at the free surface and the second simulation utilizes the Level Set Method (LSM) to predict the position of the free water surface. The LSM has been proven to be an accurate method within LES to predict multi-phase boundaries (e.g. Yue et al. 2003, Croce et al. 2004, Kang and Sotiropoulos 2012).

4.1 Computational Setup and Boundary Conditions

The computational setup corresponds to complementary experiments that were carried out in Cardiff University's hydraulics laboratory. A 10m long, W=0.30m wide tilting flume (bed slope 1/2000) was equipped with a model abutment which extended through the flume height. The abutment had length by width dimensions of L=0.1m. The discharge was chosen as Q=2.6l/s for which the uniform flow depth was H=3.8cm. This resulted in a bulk velocity of U_b=0.2m/s and a mean shear velocity of u*=0.012m/s. The uniform-flow bed shear stress, $<\tau>$=0.15N/m², was calculated from the hydraulic radius and the bed slope of the flume. The Reynolds number based on U_b and four times the hydraulic radius, R was $\mathbf{R}$ = 27,200 and the Froude number was $\mathbf{F}$ = 0.37. In the experiment, detailed water surface profiles were measured using a point gage. The laboratory and numerical setups are presented in Figure 4-1, in which all dimensions are normalized with the length and width of the abutment, L.
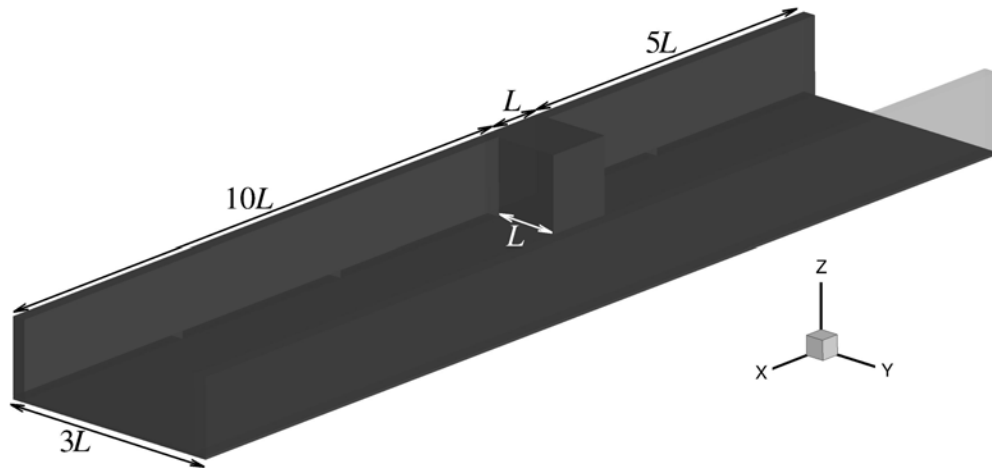
Figure 4-1 Computational domain and dimensions of the flow around an abutment

In the LES, a constant discharge was introduced into the system at the inlet section, a simplified inlet treatment, which is necessary due to the fact that the water surface elevation is unknown at the inlet. The convective boundary condition was used at the outlet to make sure that coherent structures leave the system without creating unphysical oscillations. The no-slip boundary condition was employed for smooth side walls and bottom of the flume as well as for the walls of the abutment. For the rigid lid simulation, the water surface was treated with a von-Neuman slip condition for tangential velocities and zero velocity for the velocity normal to the lid. For the simulation with moving water surface the level set method is employed to predict the water surface elevation at every time step.

The computational domains are discretized with fine uniformly spaced grids. A coarse mesh free-surface simulation is carried out to investigate the grid resolution effects on determination of water surface profile, only minor differences are found and only the fine mesh results are shown. The details of the grid spacing in wall units are given in Table 4-1. The flow is driven by gravity, g=9.81 m/s^2 and the dynamic viscosity and density of water (air) are $1\times10^{-3}(1.8075\times10^{-5})$kg/(ms) and $1000(1.205)$kg/m^3, respectively. The air phase is only taken into account for the free surface simulations so that air properties are only important for these simulations. All simulations are initially run for a period of 27 eddy turn-over times ($t_e = H/u_*$) to develop the flow, and then they are continued for another $54t_e$ to obtain flow statistics.

Table 4-1 Grid resolution

CASE	Δx	Δy	Δz	Δx^+	Δy^+	Δz^+
Free Surface (Coarse Mesh)	0.006250	0.006250	0.003000	76	76	18
Free Surface (Fine Mesh)	0.003125	0.003125	0.001125	38	38	7
Rigid Lid	0.003125	0.003125	0.000945	38	38	6

4.2 Results and Discussions

Figure 4-2 presents an overall impression of the time-averaged water surface of this flow as predicted by the LSM-based LES on the fine grid. The water surface upstream of the abutment is fairly calm; however, there is a marked dip around the leading edge of the abutment, a couple of well-pronounced standing waves slightly downstream of that edge, and a rough and wavy water surface downstream of the abutment. The zoomed-in area at the bottom right of the figure visualizes the water surface dip and the standing waves.
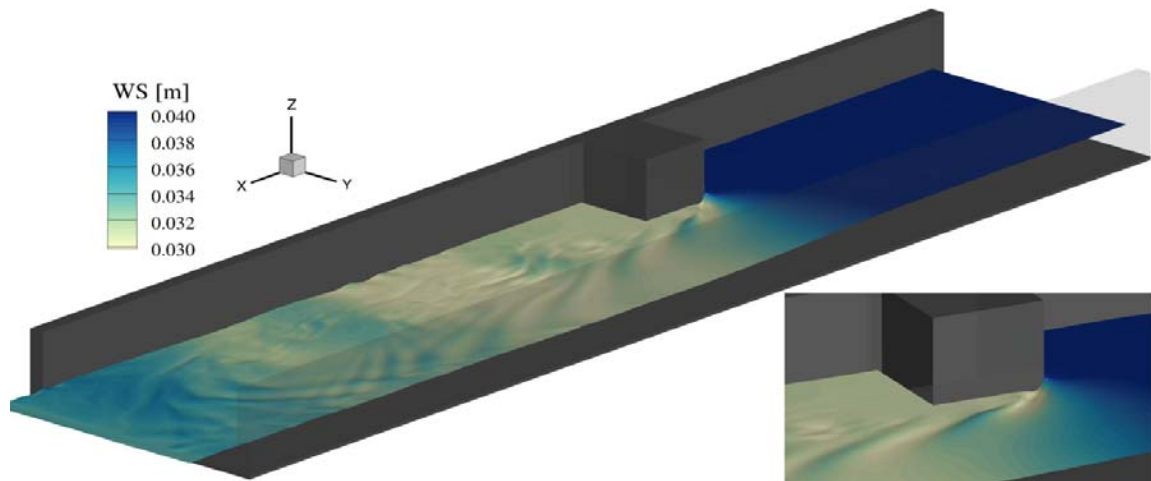
Figure 4-2 3D view of the water surface and blow-up of the area around the abutment

A quantitative assessment of the predictive capabilities of the water-surface resolved large-eddy simulation is provided in Figures 4-3 and 4-4, which depict measured (dots) and simulated (solid lines for free surface and dashed line for rigid lid) longitudinal (Figure 4-3) and cross-sectional profiles (Figure 4-4) of the water surface. The simulated longitudinal profiles (Figure 4-3) along A and B are in very good agreement with the observed data. The water surface is above the uniform flow depth in an M1 profile immediately upstream of the abutment due to the backwater effect. Flow acceleration around the abutment leads to a depression of the water surface before it recovers slowly towards uniform flow depth. The standing wave seen in Profile A appears overpredicted by the numerical simulation; however, this feature was also observed in the laboratory experiment but was not detected by the point gage measurements.
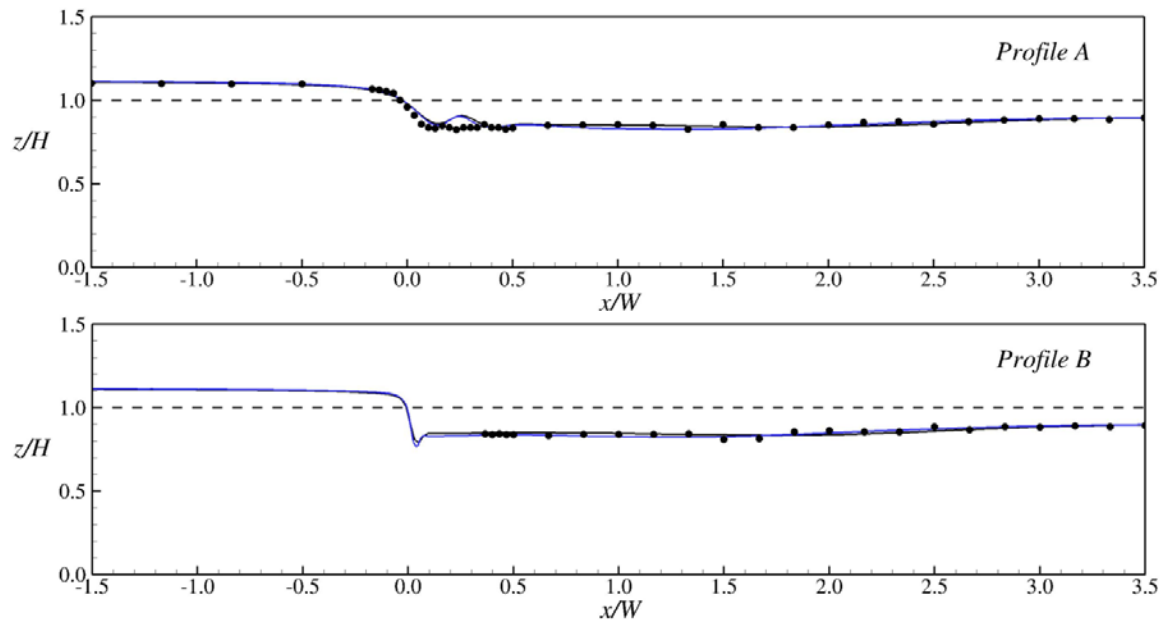
Figure 4-3 Longitudinal water surface profiles at two locations. Solid dots are experimental data, the blue line is the simulated profile on the fine grid, the black line is the simulated profile on the coarse grid. See Figure 4-4 (bottom right) for profile location.

The numerically-predicted cross-sectional water surface profiles are in very good agreement with the measured ones. The slight overestimation of the standing wave seen at Profile A is also noticed in Profiles c, d' and d; however, the differences are very subtle and the accuracy of the point gage is probably not high enough to resolve such features. The local Froude number is Fr=0.78 at the point where the water surface level dip is maximum (see Profile b'), which is more than twice its original value. This finding points out that the rigid lid assumption used for flows with Fr number lower than 0.4 is not applicable for the free flow around an abutment.
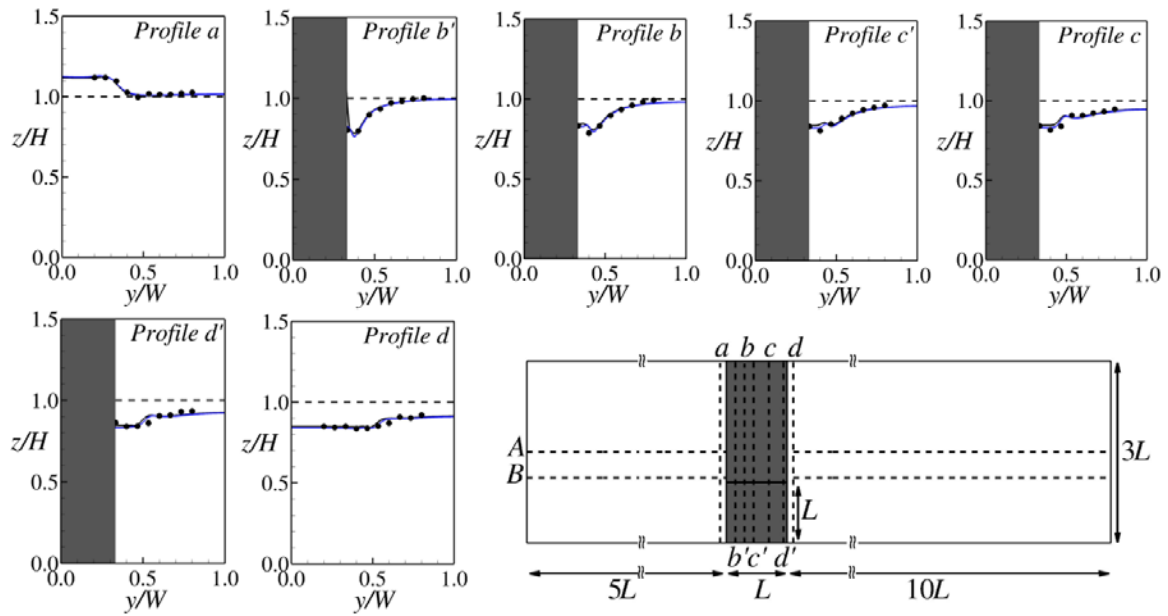
Figure 4-4 Cross-sectional water surface profiles at seven locations. Solid dots are experimental data, the blue line is the simulated profile on the fine grid, the black line is the simulated profile on the coarse grid. See bottom right for profile location.

Figure 4-5 presents LES calculated time-averaged streamwise velocities in a horizontal plane at z^+=100 for both simulations. The flow separation at the leading edge of the abutment is more pronounced in the rigid lid simulation leading to a larger

recirculation zone in the contracted area. Less obvious differences in the streamwise velocity distribution are the result of the differences in water levels. In the free-surface simulation, the velocities are slightly lower upstream of the abutment and slightly higher downstream of the abutment compared to velocities from the rigid lid simulation, which is to be expected.
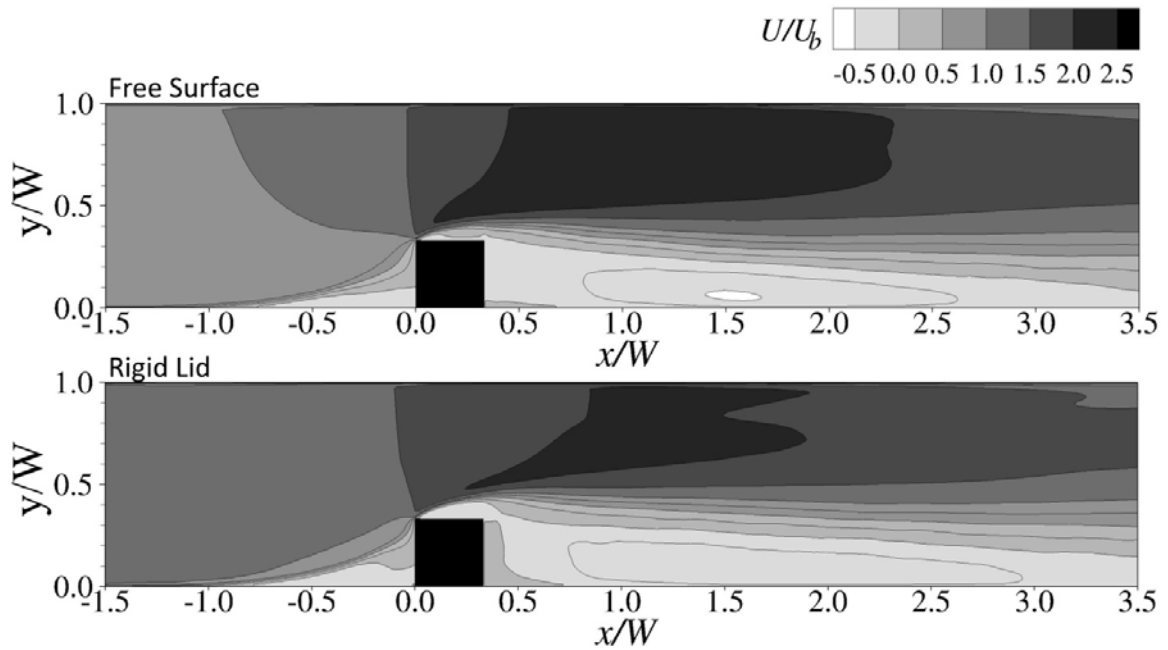
Figure 4-5 Distribution of streamwise velocity in a horizontal plane near the bed at $z^+=100$ computed from free-surface-resolved (top) and rigid lid (bottom) simulations

Figure 4-6 presents distribution of bed shear stress, τ (calculated as $\tau=\mu dS/dz$, where $S=\sqrt{U^2+V^2}$ at $z^+\approx6$) normalized with the mean uniform flow shear stress $\langle\tau\rangle$, for free surface and rigid lid simulations. High values of bed shear stress are observed close to the leading edge of the abutment where the horseshoe vortex system is present and in the contraction which is where the flow accelerates. Overall, the distribution is very

76

similar. Figure 4-7 provides a more quantitative comparison of bed shear stress distributions presenting profiles for free surface and rigid lid simulations at different locations. At the leading edge of the abutment ($x/W=0$), the rigid lid simulation yields higher bed shear stresses. There the backwater effect of the free-surface simulation causes lower velocities before acceleration due to the water surface dip occurs.
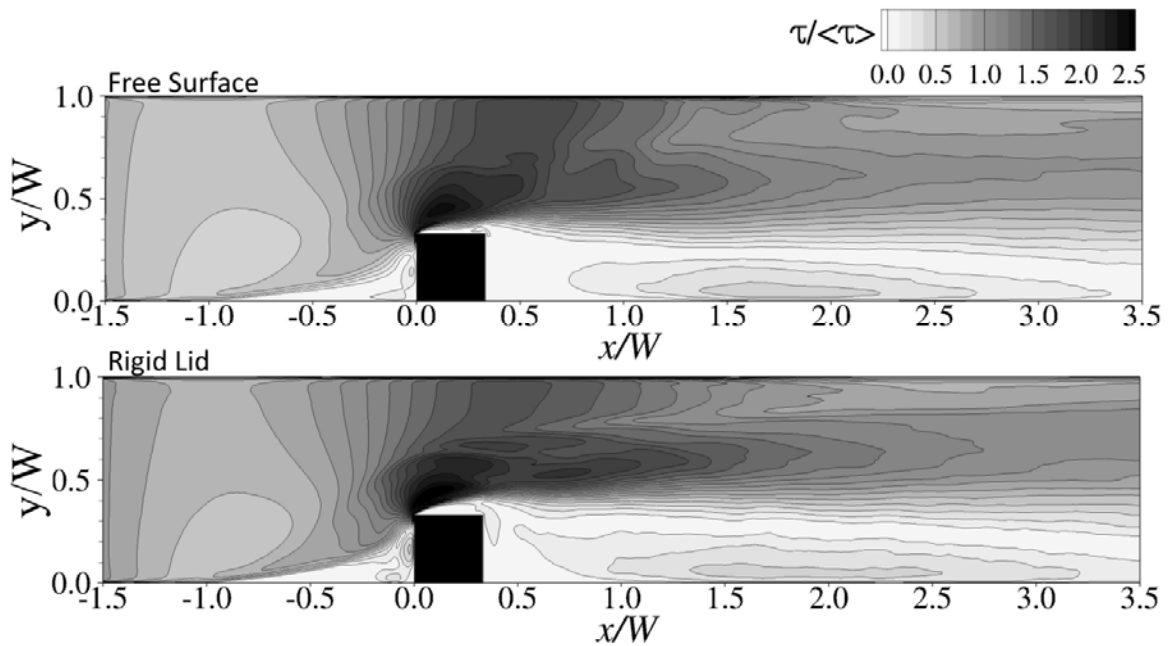
Figure 4-6 Distribution of bed shear stress as computed from free-surface-resolved (top) and rigid lid (bottom) simulations
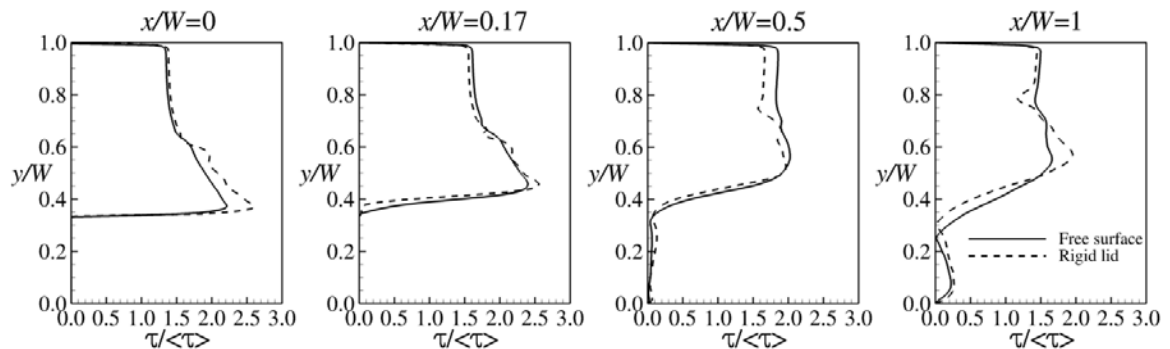
Figure 4-7 Bed shear stress profiles at selected locations

77

Figure 4-8 depicts the spatial distribution of normalized turbulent kinetic energy (*tke*) in a horizontal plane near the bed at $z^+=100$ for free surface and rigid lid simulations. Overall, the free surface simulation computes similar magnitudes of *tke* values in the flow compared with the rigid lid simulation. Areas of high *tke* occur immediately before and at the leading edge of the abutment and in the shear layer of the flow separation zone in the contracted region and downstream of the abutment. There are a few significant differences, which are quantified with help of Figure 4-9, which presents *tke* profiles at different locations (locations are provided in Figure 4-11). Remarkably, the *tke*-profile at $x/W=0$ shows that the free surface simulation computes six times higher *tke* than the rigid lid simulation, and at $x/W=0.17$ the maximum *tke* is nearly three times higher. Downstream of the abutment, e.g. *tke* profiles for $x/W=0.5$ and 1.0, differences in *tke* distribution between free surface and rigid lid simulation vanish, and the profiles at $x/W=2.0$ are almost identical (not shown for brevity).
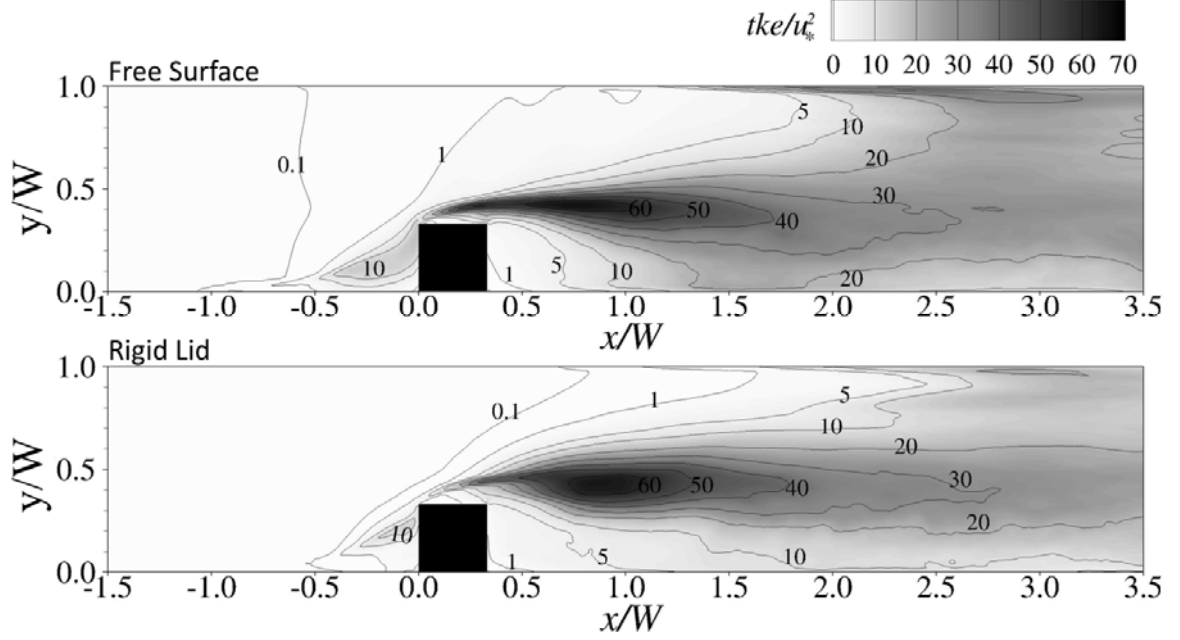
Figure 4-8 Distribution of normalized turbulent kinetic energy in a horizontal plane near the bed at $z^+=100$ as computed from free-surface-resolved (top) and rigid lid (bottom) simulations
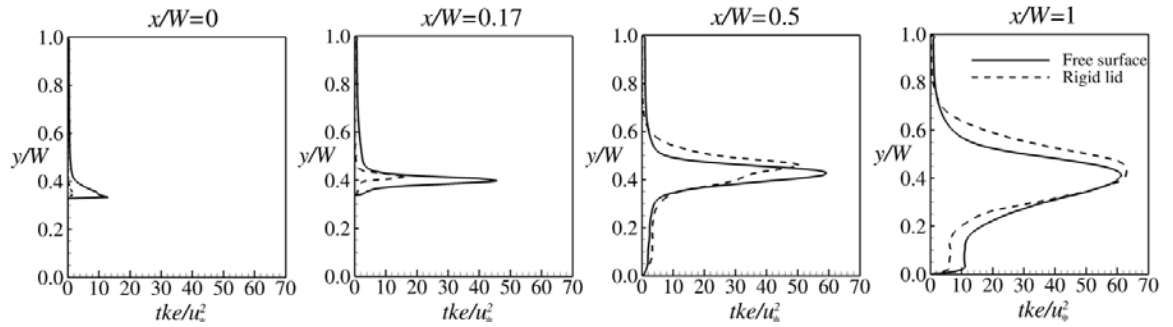
Figure 4-9 Near-bed normalized turbulent kinetic energy profiles at selected locations

Figure 4-10 depicts the vorticity magnitude for free surface and rigid lid simulations at the horizontal plane at $z^+=100$. Areas of high vorticity magnitude are observed within the horseshoe vortex system and in the shear layers of the separation zones upstream of the abutment and in the contracted area. The area of high vorticity

79

magnitude downstream of the abutment extends a bit further for the rigid lid simulated flow. The overall distribution however is very similar for both cases.
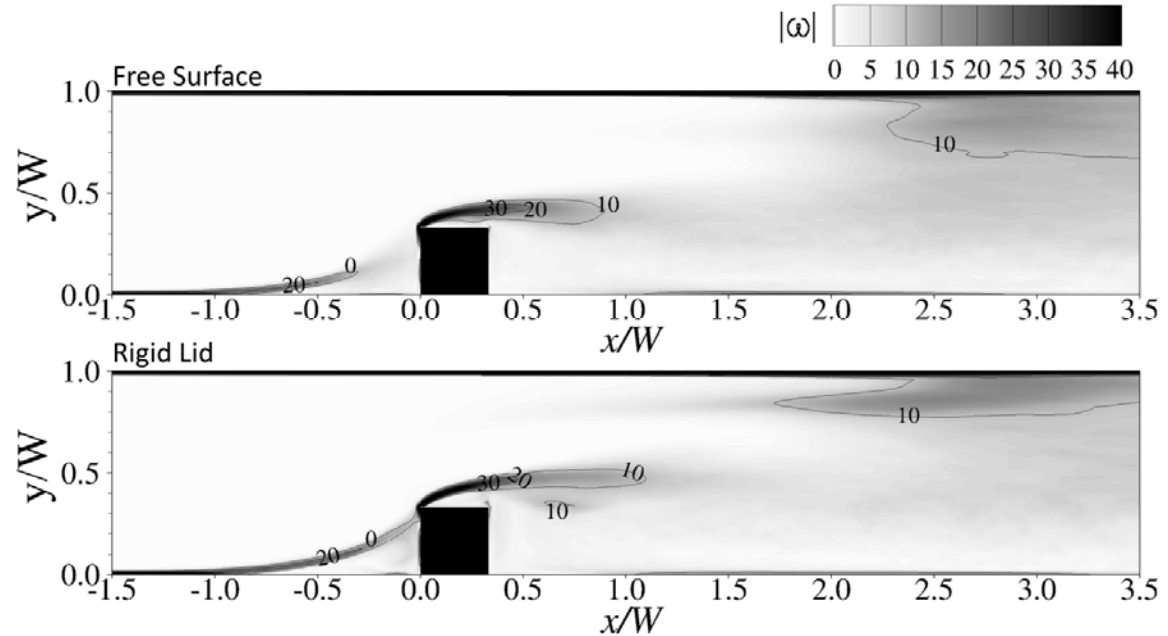
Figure 4-10 Distribution of vorticity magnitude in a horizontal plane near the bed at $z^+=100$ as computed from free-surface-resolved (top) and rigid lid (bottom) simulations

Figure 4-11 shows a top view of turbulence structures represented by isosurfaces of the Q-criterion, a scalar that highlights regions in the flow where rotation dominates over strain, shaded by the instantaneous streamwise velocity, here Q=75 for both simulations. The instantaneous turbulent structures observed in Figure 4-11 are also confirmed throughout the animations for both simulations. The multi-component horseshoe vortex system upstream of the abutment is similar in size and coherence in both flows; however downstream of the leading edge of the abutment marked differences are noticeable. First of all, the turbulence structures that are springing of from the leading edge of the abutment of the rigid lid simulation appear to be much more coherent, and

individual horizontal vortices are more distinguishable than in the free-surface resolved simulation, where they appear to be more elongated.
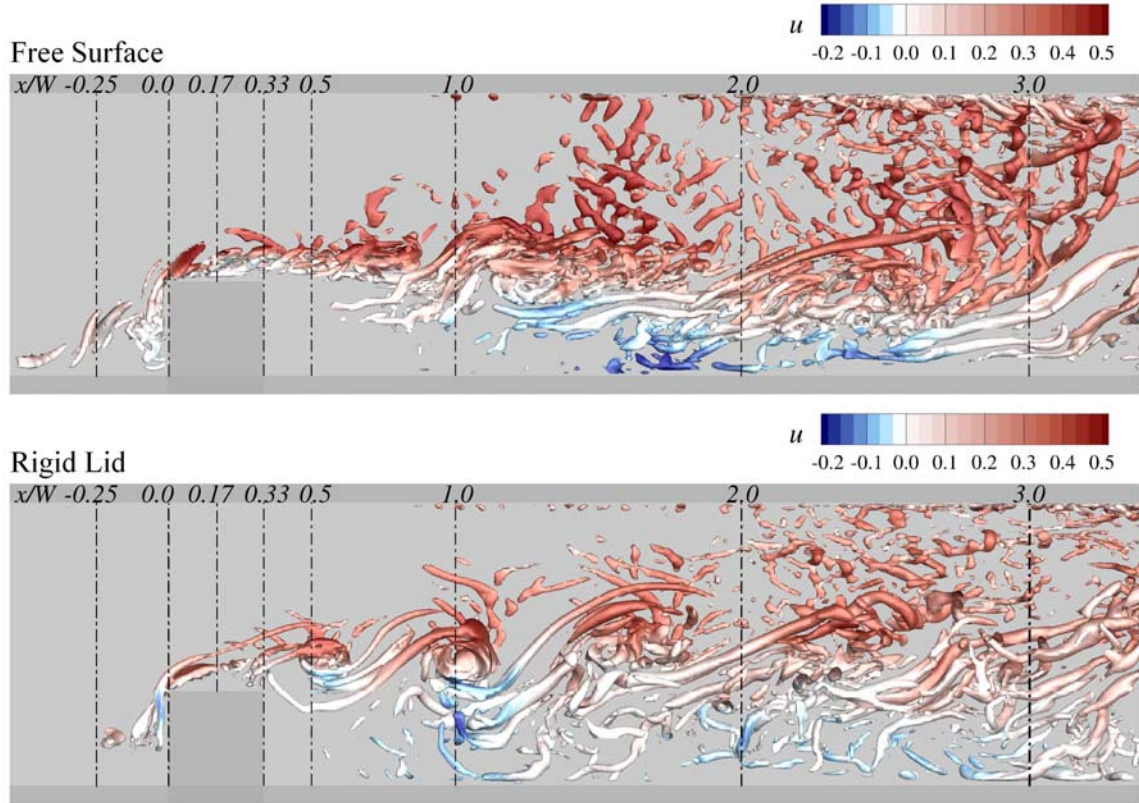
Figure 4-11 Turbulence structures educed through isosurfaces of the Q-criterion as computed from free-surface-resolved (top) and rigid lid (bottom) simulations

The stretching of the separated vortices in the free surface simulation is instigated at the water surface dip, where a strong local acceleration takes place. Due to the strong acceleration, which is documented by the color-shading of the isosurfaces, the detached vortices are advected downstream where they either re-attach or move relatively close along the abutment wall. In the rigid lid simulation they are advected away from the leading edge of the abutment into the contracted area and no re-attachment takes place.

For both simulations, the horseshoe vortices around the leading edge of the abutment are responsible for the highest bed shear stresses.

Figures 4-12 and 4-13 quantify the structural changes of the turbulence due to different treatment of the water surface boundary and that have been observed with the help of Figure 4-11. They present contours of the normal Reynolds stresses $u'u'$ and $v'v'$ normalized with the squared shear velocity of the uniform flow at a horizontal plane close to the bed ($z^+=100$) for free surface and rigid lid simulations. Figure 4-12 demonstrates the effect of local flow acceleration and vortex stretching (as identified in Figure 4-11) as normal streamwise Reynolds stresses, $u'u'$, are significantly larger in the free surface simulation than in the rigid lid simulation. The maximum of $u'u'$ is almost 100 times the squared shear velocity, while for the rigid lid simulation the maximum is "only" $u'u'/u_*^2 \approx 50$. In the free-surface simulation elevated levels of streamwise turbulence are also found near the sidewalls downstream of the abutment, e.g. at x/W≈1.5 on the right sidewall and x/W=2.2 on the left sidewall, which is where the flow decelerates apparently aided by the sidewall shear while attempting to return to uniform flow. This entails the production of turbulence structures (see Fig 4-11), a feature that is absent in the rigid lid simulation, due to the fact that the flow remains "uniform" along the channel.
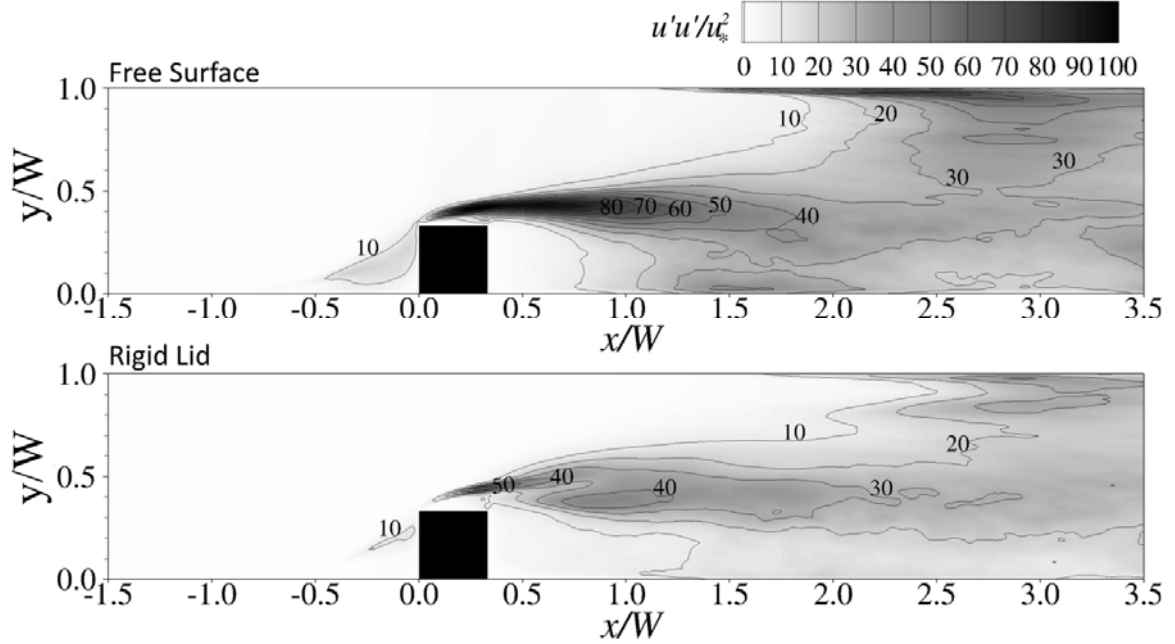
Figure 4-12 Distribution of streamwise normal stresses in a horizontal plane near the bed at $z^+=100$ as computed from free-surface-resolved (top) and rigid lid (bottom) simulations

Figure 4-13, showing the near-bed distribution of the normal spanwise Reynolds stress $v'v'/u_*^2$, demonstrates why the *tke*-levels of both simulations are similar in magnitude downstream of the abutment. The rigid lid simulated flow attains much higher $v'v'$ values than the free-surface simulated flow and while in the former the maximum $v'v'/u_*^2 \approx 80$, the maximum in the latter case is approximately half of that. The reason for this is the structural differences in the instantaneous flow. In the rigid-lid simulated flow the turbulence structures exhibit a much more pronounced rotational behavior (see Figure 4-11), i.e. they entrain fluid laterally and hence promote spanwise exchange and thus spanwise normal stresses are high. The free-surface simulated flow is dominated by streamwise stretching vortices and hence the lateral entrainment capacity is reduced. The values of the wall-normal Reynolds stress $w'w'$ are very similar for both simulations (not shown for brevity).
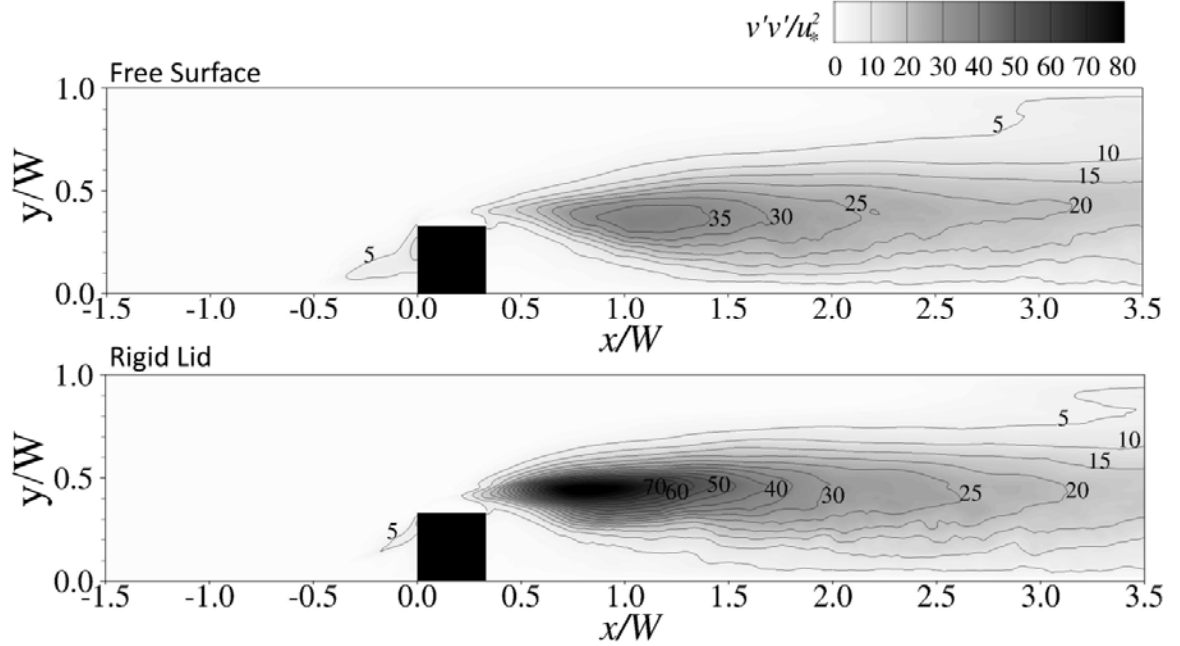
Figure 4-13 Distribution of cross-streamwise normal stresses in a horizontal plane near the bed at $z^+=100$ as computed from free-surface-resolved (top) and rigid lid (bottom) simulations

## 4.3 Summary and Conclusions

This chapter of the thesis has investigated the effects of the free surface on the flow around a bridge abutment by comparing and discussing the results of two separate Large Eddy Simulations (LES). The first LES employed the level set method (LSM) to capture accurately the water surface deflection as a result of the flow and the second used the rigid lid boundary condition at the water surface, i.e. no water surface deflection, which is the most common treatment in CFD of open-channel flow. The water surface profiles obtained from the LSM-based simulation were validated with data from a complementary physical experiment carried out under analogous geometrical and flow conditions. Predicted water surface profiles showed very good agreement with the measured data. Investigation of the time-averaged and instantaneous flow properties

obtained by the two showed that the first order statistics such as primary velocity and bed shear stresses are very similar in both cases; however 3D turbulent structures are markedly different and they lead to differences in the second order statistics such as turbulent kinetic energy and Reynolds stresses. It is shown that turbulence structures are stretched due to local flow acceleration caused by strong deformations of the water surface, particularly near the leading edge of the abutment. There, the turbulent kinetic energy attains maximum values in the free surface simulation, a feature that is not picked up in the rigid lid simulation. Turbulence structures of the rigid lid simulation are more coherent and show pronounced rotation, whilst the turbulence structures of the free-surface resolved LES are dominated by streamwise vortex stretching exhibiting less coherence. These differences in the turbulent structures result in higher streamwise and lower spanwise normal Reynolds stresses in the free-surface LES than in the rigid-lid simulation.

CHAPTER 5

FLOW DYNAMICS THROUGH A SUBMERGED BRIDGE

OPENING WITH OVERTOPPING

During extreme hydrological events, existing bridges may become fully submerged with submerged orifice flow occurring through the bridge opening and overtopping of the bridge deck. In 1994, tropical storm Alberto dumped as much as 71 cm of rainfall over widespread areas of Georgia which resulted in damage to more than 500 bridges. The primary cause of damage to bridges was scour around abutments and approach embankments accompanied by bridge overtopping in many cases. The flood of 1993 in the midwestern U.S. paralyzed a nine-state area with flood recurrence intervals varying from 100 to 500 years. Two months after the flood, a scour hole with a depth of 17 m was mapped near the abutment of an interstate bridge on the Missouri River (Parola et al. 1998). Epic flooding with flood recurrence intervals in excess of 500 years occurred in Georgia in 2009 in the Atlanta metropolitan area with extensive damage to bridge abutments and embankments due to overtopping (Gotvald and McCallum 2010). These examples of bridge abutment and embankment failures highlight the need for additional research in this area. Currently, no formula for abutment scour is widely applicable, nor has the term itself been distinctly defined because of difficulties in understanding the complicated hydrodynamics that lead to scouring near bridge abutments.

The objectives of this chapter of the thesis are to quantify the mean and instantaneous flow through a bridge opening with overtopping, to elucidate the complex three-dimensional hydrodynamics and discuss their potential effects on the local scour mechanism. An existing large-eddy simulation approach is refined with a level-set

method to compute the free surface variation and the simulation provides unprecedented details of the water surface deformation and turbulence characteristics. The simulations are complemented with an analogous laboratory experiment, and the data are used to validate the LES.

5.1 Computational Setup and Boundary Conditions

The computational setup shown in Figure 5-1 is chosen to correspond to the complementary physical experiments carried out in Cardiff University's hydraulics laboratory. A 10m long, W=0.30m wide tilting flume (bed slope 1/2000) was equipped with a model bridge consisting of a square abutment with length and width of L=0.1m, and height of h_a=0.05m. The rectangular bridge deck had a girder thickness of h_d=0.024m, and it extended across the channel. The geometric contraction ratio of bridge opening width to channel width was 0.67. In the simulation the deck thickness was taken as h_d=0.025m which allowed for more efficient grid generation and code parallelization. Before inserting the bridge model into the flume, the stage-discharge relationship for uniform flow was established for which the flow depth was controlled via a weir at the downstream end. With the bridge in place, the water backed up and caused an increase of water depth upstream of the bridge. The discharge, chosen as Q=8.5l/s corresponds to an extreme flood event and the corresponding uniform flow depth was H=9.2cm. This resulted in a bulk velocity of U_b=0.3m/s and a mean shear velocity of u_*=0.017m/s. The Reynolds number based on U_b and four times the hydraulic radius, R, was **R** = 70,250, and the Froude number of the uniform flow was **F** = 0.32. In the experiment, detailed water surface profiles were measured using a point gage. The laboratory and numerical

87

setups are presented in Figure 5-1, in which all dimensions are normalized with the length/width of the abutment, L.
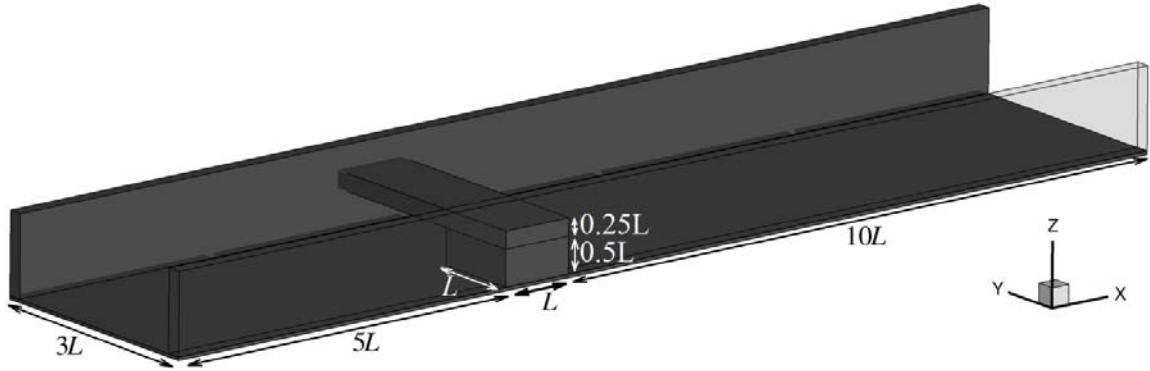
Figure 5-1 Computational setup

In the LES, a constant discharge is introduced into the system at the inlet section, a simplified inlet treatment, which is necessary due to the fact that the water surface elevation is unknown initially at the inlet. The convective boundary condition is used at the outlet ensuring that coherent structures leave the system without creating unphysical numerical oscillations that reflect into the domain. The no-slip boundary condition is employed for all walls including the bridge abutment and deck. The computational domain is discretized with a uniform mesh and several resolutions are tested. The grid resolution in wall units is provided in Table 5-1. The flow is driven by gravity, g=9.81 m/s^2 and the dynamic viscosity and density of water (air) are 1×10-3(1.8075×10-5)kg/(ms) and 1000(1.205)kg/m^3, respectively; hence, Reynolds number, **R**, and Froude number, **F**, of the simulation are the same as in the experiment. The simulation is run initially for a period of 10 eddy turn-over times ($t_e = H/ u_*$) to develop the flow and establish the correct water surface elevation, and is then continued for another $51t_e$ to obtain turbulence statistics.

Table 5-1 Grid resolution of the two LES simulations

Grid Resolution	Δx (m)	Δy (m)	Δz (m)	Δx^+	Δy^+	Δz^+
Coarse Grid	0.006250	0.006250	0.0031250	104	104	26
Fine Grid	0.003125	0.003125	0.0015625	52	52	13

5.2 Results and Discussions

Figure 5-2 (top) presents an overall three-dimensional view of the time-averaged water surface of this flow as predicted by the numerical simulation. Also plotted (bottom right) is a close-up photograph of the corresponding flow over the bridge in the experiment. The flow accelerates over the bridge causing a marked drop of the water surface. The flow plunges downstream of the bridge, which results in a standing wave or an undular hydraulic jump. Downstream of the standing wave the flow recovers gradually, exhibiting wavy motion, to the uniform flow condition. In general, Figure 5-2 shows very good qualitative agreement between the numerical results and the conditions observed in the laboratory experiment.
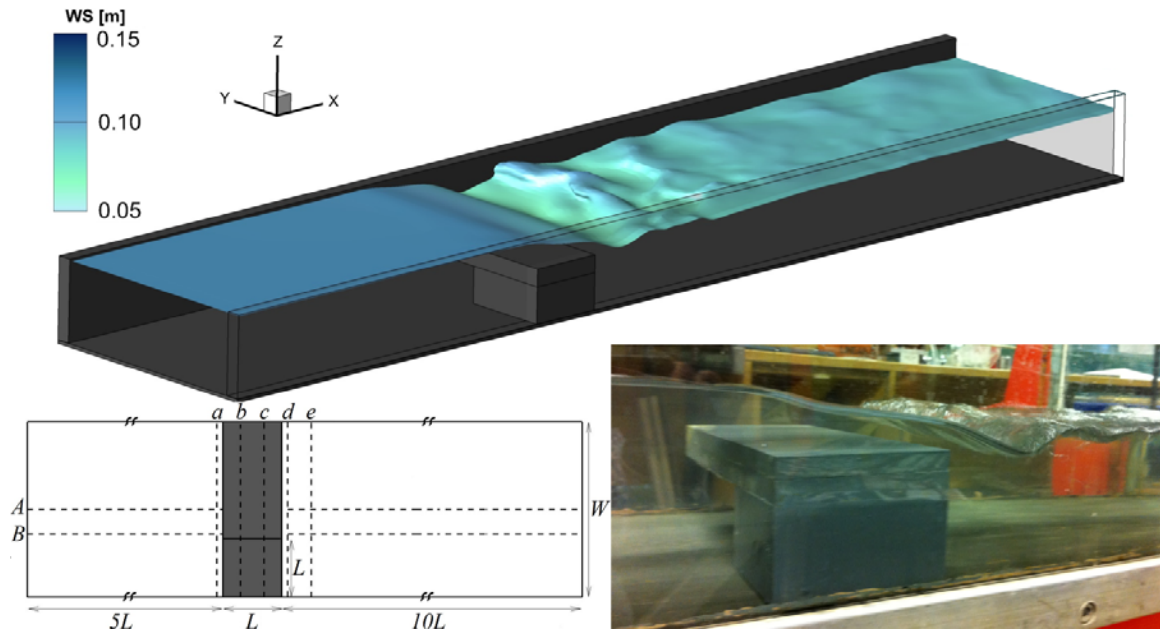
Figure 5-2 Simulated water surface (top), measurement locations (bottom left) and close-up photograph of the laboratory experiment (bottom right)

A more quantitative assessment of the predictive capabilities of the simulation results is provided in Figures 5-3 and 5-4, which depict measured (dots) and simulated (lines) longitudinal (Figure 5-3) and cross-sectional profiles (Figure 5-4) of the water surface. The simulated longitudinal profiles (Figure 5-3) along A and B (see sketch in the lower left of Figure 5-2) are in very good agreement with the observed data irrespective of grid resolution (blue line = fine grid, black line = coarse grid). There is a small, but consistent overestimation of the water surface elevation on and upstream of the bridge. The reason for this discrepancy is that the height of the bridge deck in the simulation was chosen to be exactly 50% of the depth of water underneath the deck so that the numerical domain was easier to decompose in the vertical, which improved the parallelization of the code. The height of the bridge deck in the experiment was 48% of the depth of the water underneath it. There is some discrepancy between numerical prediction and measurement

90

in the vicinity of the standing wave, an area that is highly turbulent and where accurate water surface measurements using a point-gage are difficult to achieve.
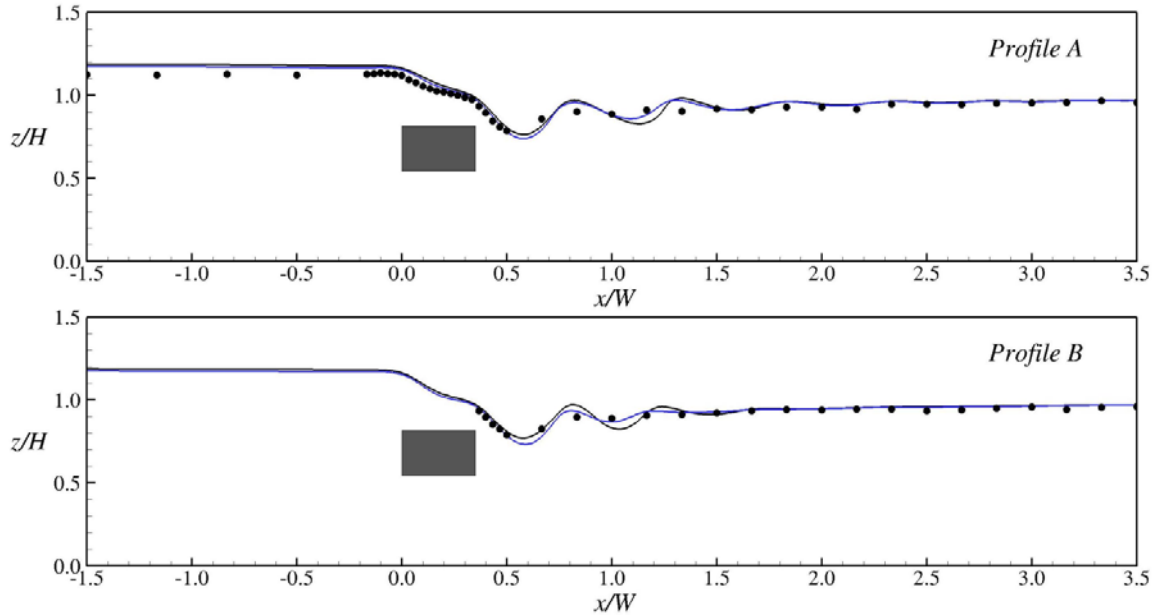
Figure 5-3 Longitudinal water surface profiles along two locations, which are channel center line (Profile A) and one-third of the channel width (Profile B) at the abutment face

Figure 5-4 presents measured and simulated cross-sectional water surface profiles at selected locations (a-e, see Figure 5-2). Upstream and on the bridge (Profiles a and b) the numerically predicted profiles are slightly higher than the measured ones, whereas numerically predicted Profiles c, d and e are in very good agreement with the measurements.
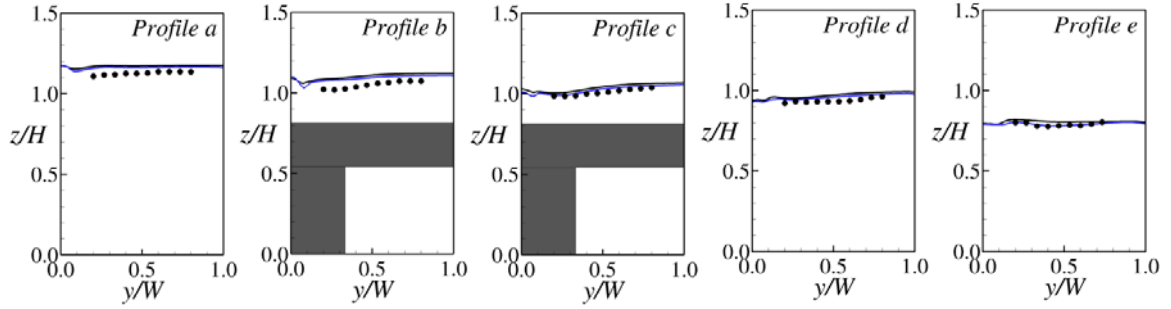
Figure 5-4 Cross-stream water surface profiles along six locations (Profiles a-e) looking upstream

Figure 5-5 provides a three-dimensional view of the time-averaged flow, depicting streamlines color coded by the turbulent kinetic energy (*tke*). Figure 5-5a) provides an oblique view from upstream visualizing the plunging flow over the deck and two distinct vortices (marked as AV and RV1). The approach flow on the abutment side is forced over the structure in a helical arch-shaped vortex (AV). This vortex rotates counter-clockwise and the rotation is induced near the bed (see Figure 5-5b) through the abutment-caused separation vortex (RV2a). As the vortex arches over the deck the flow is accelerated and the rotation disappears. The flow separates from the trailing edge of the deck creating a long longitudinal recirculation vortex (denoted RV1 in Figure 5-5a) downstream of the deck. Near the bed, small separation vortices (RV2a, b and d in Figure 5-5b) occur around the abutment. The near-bed recirculation zone denoted RV2c is the most significant one, as it generates and carries a significant amount of turbulent kinetic energy. A strong shear layer forms at the interface between this zone and the fast orifice flow from underneath the bridge, in addition the flow from over the deck plunges into this area creating strong turbulence. The *tke* in this shear layer exceeds eighty times the squared shear velocity of the uniform channel flow (u_*^2).
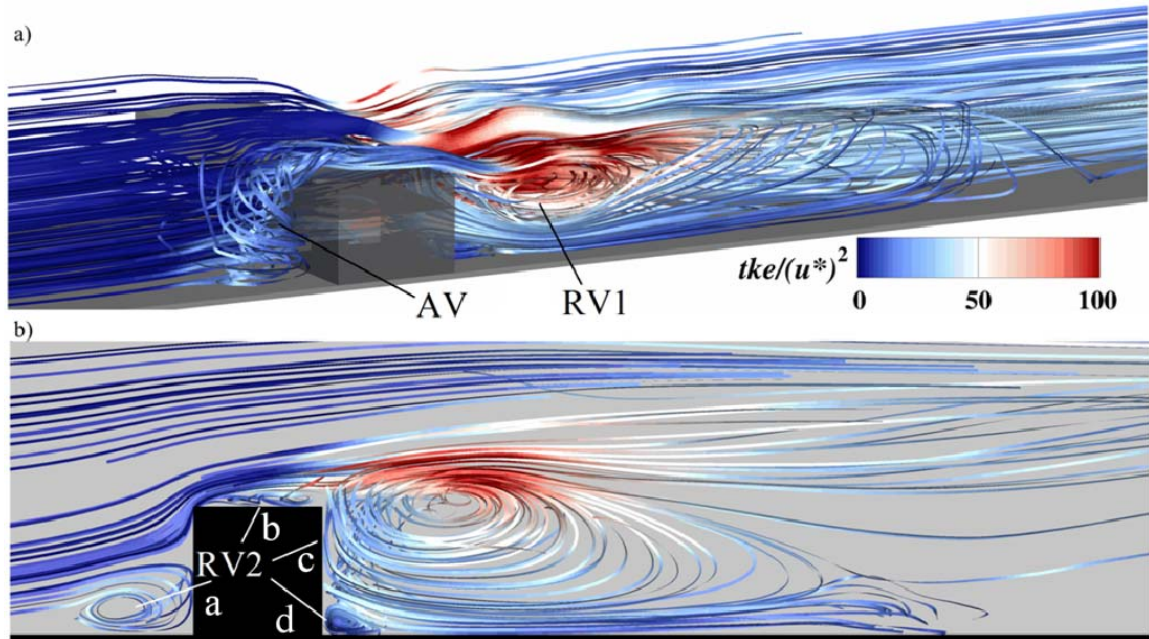
Figure 5-5 Streamlines of the time-averaged flow over a submerged bridge. a) oblique view from behind and b) in a horizontal plane near the bed

A more quantitative view of the flow is provided with the help of Figure 5-6, in which the time-averaged streamwise velocity together with streamlines in three longitudinal planes are plotted. The time-averaged flow over the bridge is subdivided into two portions: 74.8% of the discharge is forced underneath the bridge deck as submerged orifice flow, whilst the remaining 25.2% discharges over the deck as a weir flow. The deck acts similarly to a broad-crested weir and the critical depth of the portion over the deck is $y_c=(q^2/g)^{1/3}=1.73$cm, which is attained at $0.93L$, i.e. very close to the trailing edge of the deck. The flow plunges into the downstream area as supercritical flow, and undergoes an "undular" hydraulic jump. A vertical recirculation zone forms downstream of the abutment as depicted in Figure 5-6a. On the side of the abutment the standing wave

is not as steep as in the middle of the channel, a feature that was also observed in the experiment. At y/W=0.33 the separation vortex over the deck interacts with the lateral flow separation and recirculation from the abutment generating a vortex core at x/W=0.7 and a saddle point underneath (Figure 5-6b). At y/W=0.67 (Figure 5-6c) the submerged orifice flow features streamwise velocities up to almost three times the bulk velocity, which is due to the lateral and vertical contraction of the flow not only by the abutment and deck but also by the vertical and horizontal recirculation zones of the separated flow (see separation vortices SV1 and SV2 in Figure 5-9).

Figure 5-7 quantifies the complex flow over the submerged bridge in terms of bed shear stress τ, normalized with the mean boundary shear stress ($<\tau>$=ρgRS) for uniform flow, and *tke*, normalized with the squared mean shear velocity for uniform flow, u_*^2. The highest values of bed shear stress are observed in the bridge cross-sections and close to the leading edge of the abutment, which is where the flow is contracted. There is also a region of high bed shear slightly downstream of the abutment. The area of highest near-bed *tke* does not coincide with the area of highest bed shear, but, as discussed earlier, is found where the plunging flow from over the deck coincides with the edge of the lateral recirculation zone of the separated flow. This is significant for local scour; Hong et al. (2014), who report on experimental investigations of local scour around a submerged bridge, show that the location of the deepest scour hole occurs downstream of the bridge, and in fact at an analogue location to the high-*tke*-area identified herein.
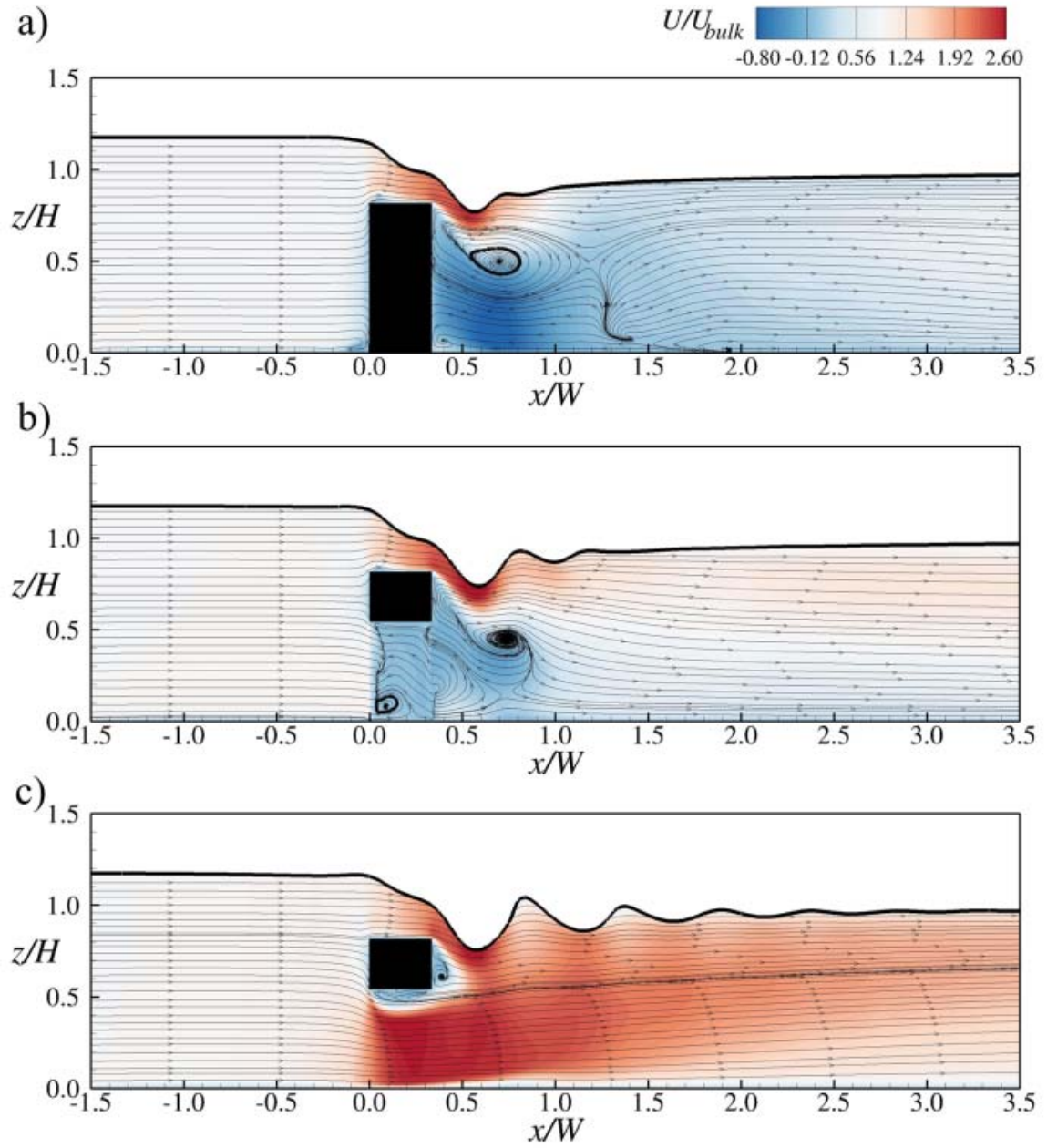
Figure 5-6 Time-averaged velocity contours together with streamlines of the flow in three selected longitudinal-sections: a) y/W=0.17; b) y/W=0.33; c) y/W=0.67
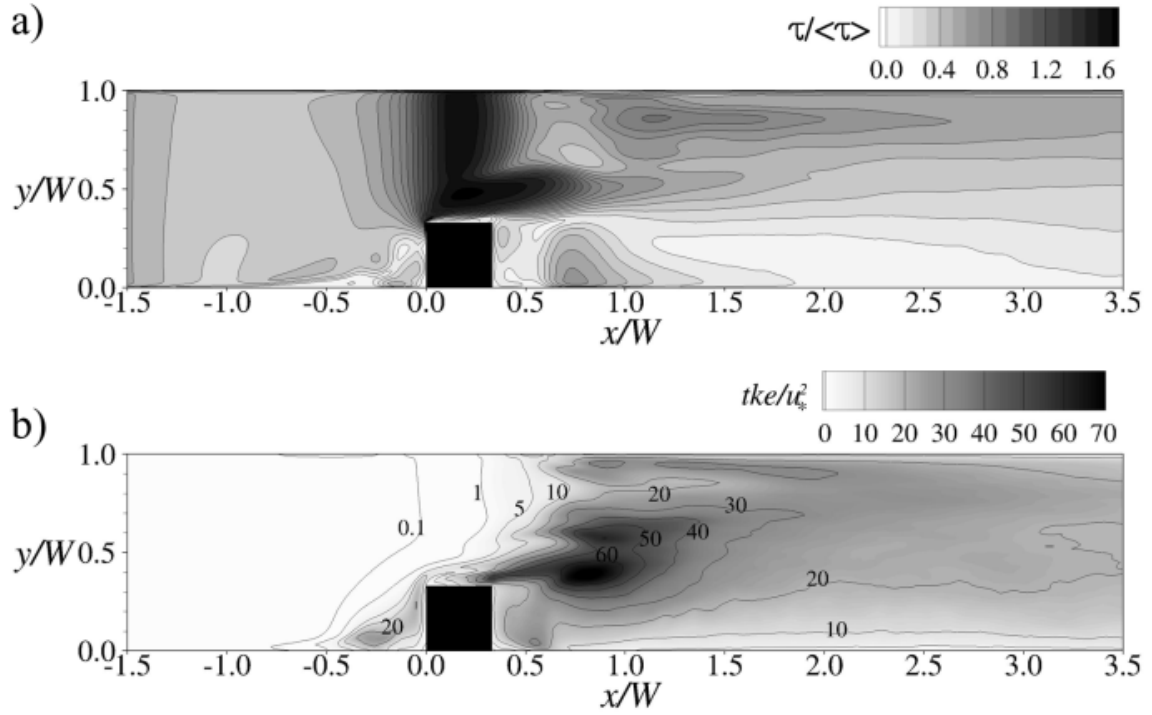
Figure 5-7 a) Contours of the normalized bed-shear stress and b) contours of the normalized turbulent kinetic energy in a horizontal plane at $z^+=50$.

Figures 5-8 and 5-9 provide an overview of the many instantaneous turbulence structures and features of this flow. Figure 5-8 presents instantaneous streamlines in an oblique view from upstream. The afore-mentioned helical arch-vortex is visible as well as the flow acceleration and plunging flow downstream of the deck. The longitudinal recirculation downstream of the deck is not very clear because the flow is too turbulent to identify distinct large-scale vortices. The streamlines are color coded by the instantaneous streamwise velocity, u, and areas of fast moving fluid over the deck are discerned as well as areas of negative velocity near the bed behind and in front of the abutment. Figure 5-9 presents isosurfaces of Q, a scalar that educes regions in the flow where rotation dominates strain, visualizing coherent turbulence structures. Figure 5-9a isosurfaces of $Q=500$ are depicted providing evidence of the high turbulence downstream of the bridge.

Similar to the streamlines in Figure 5-8, the flow in this zone does not seem to feature distinct coherent vortices, probably due to the violent acceleration of the plunging flow resulting in many incoherent small-scale structures. In Figure 5-9b) the structures upstream of the bridge are deduced. There the flow is less violent and distinct vortex structures are found, i.e. the horseshoe vortex system near the bed (HSV), the arch vortex (AV) and vertical (SV1) and horizontal (SV2) separated vortices at the leading edges of abutment and bridge deck. A close-up of the Q-criterion-deduced structures on the downstream side shows that separated vortices in the form of rollers (SV1) spring off the leading and trailing edges of the deck; however, they lose their coherence rather quickly as a result of the fast-moving plunging flow from over the deck.
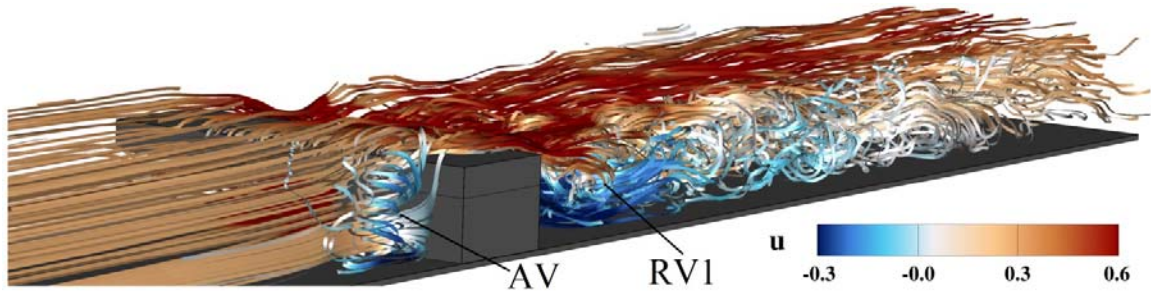
Figure 5-8 Streamlines of the instantaneous flow colored by the instantaneous streamwise velocity
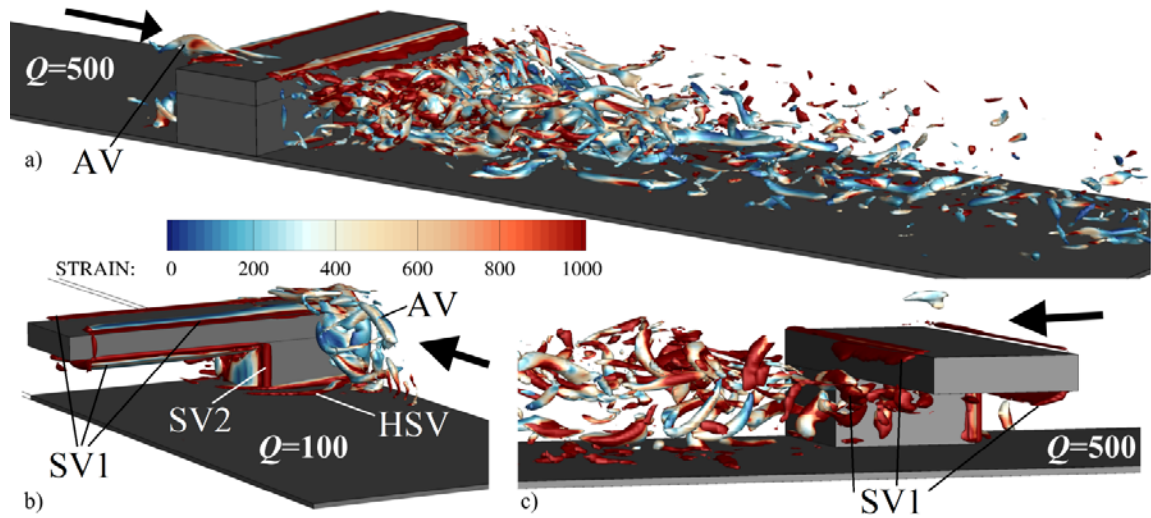
Figure 5-9 Isosurfaces of the Q-criterion colored by the rate of strain. a) oblique view from the front, b) oblique view from behind and c) view from the side. The black arrow indicates the flow direction

5.3 Summary and Conclusions

The flow through a submerged bridge with overtopping was investigated by means of a complementary experimental/numerical study. An idealized bridge model was placed in a flume and detailed water level measurements were used to validate a refined in-house large-eddy simulation (LES) code. A sophisticated numerical approach was chosen for this flow situation because of the complex turbulent structures and the severe water surface curvature caused by the bridge overtopping and lateral flow contraction due to the abutment. Analysis of the LES data revealed the complex nature of the flow featuring various vortical structures around the bridge. In addition to the horizontal flow separation vortices around the abutment, a substantial helical arch vortex spans over the bridge. The arch vortex is located on the abutment side of the bridge and its helical motion is a result of the near bed recirculation zone upstream of the abutment. The overtopping creates a horizontal recirculation zone downstream of the abutment and flow

contraction occurs underneath the deck. The overtopping flow reaches critical condition on the deck and creates areas of very high turbulence as it plunges in the form of an undular hydraulic jump downstream of the bridge. The area where horizontal and vertical recirculation zones meet is characterized by high magnitudes of turbulent kinetic energy, *tke*, and formation of substantial shear layers. The location of highest bed-shear stress, i.e. underneath the deck where the flow is contracted and accelerated, does not correspond to the location of maximum *tke*. These features of the complex turbulent flow structure induced by the bridge obstruction and flow contraction with overtopping have broader implications, relative to scour of a moveable sediment bed near a bridge abutment, that are being explored further.

CHAPTER 6

TURBULENT FLOW AROUND A SUBMERGED BRIDGE UNDER EXTREME

HYDROLOGICAL CONDITIONS

Extreme rainfall events associated with global warming are likely to produce an increasing number of flooding scenarios resulting in significant inundation and damages on bridges. These damages may lead failures for many of bridges which were not designed for extreme flow conditions. Hence, understanding the complex turbulent flow field for these flow conditions is crucial to estimate the probable failure risks for existing bridges and better design of future bridges.

The objective of this chapter of the thesis is to examine the mean and instantaneous flow field for free flow (discussed in Chapter 4), pressure flow with a partially submerged bridge deck, and overtopping flow over the bridge (discussed in Chapter 5) in a comparative manner by employing large-eddy simulations (LES), complemented with an analogous laboratory experiment. A free surface algorithm based on Level Set Method which has been proven to be an accurate method within LES to predict multi-phase boundaries (Yue et al. 2003, Croce et al. 2004, Kang & Sotiropoulos 2012) is used for prediction of water surface profiles for these extreme flow conditions.

6.1 Computational Setup and Boundary Conditions

Laboratory experiments were carried out in Cardiff University's hydraulic laboratory. A 10m long, W=0.30m wide tilting flume (bed slope 1/2000) was equipped with a model bridge consisting of a square abutment with length and width of L=0.1m, and height of h_a=0.05m. The rectangular bridge deck had a girder thickness of h_d=0.024m, and it extended across the channel. In the simulation the deck thickness was

taken as h_d=0.025m which allowed for more efficient grid generation and code parallelization. The bridge deck was not used in experiment and in the simulation of free flow for the sake of simplicity. Before inserting the bridge model into the flume uniform flow conditions were established. Table 6-1 presents the discharge (Q) and corresponding uniform flow depth (H), bulk velocity (U_b), mean shear velocity (u_*), Reynolds number (**R**) (based on U_b and four times the hydraulic radius, R), and the Froude number of the uniform flow (**F**) for free flow, pressure flow with a partially submerged bridge deck, and overtopping flow over the bridge. In the experiment, detailed water surface profiles were measured using a point gage. The laboratory and numerical setups are presented in Figure 6-1, in which all dimensions are normalized with the length/width of the abutment, L.

Table 6-1 Flow parameters

Case	Q (l/s)	H (cm)	U_b (m/s)	u_* (m/s)	R	F
Free flow	2.6	3.8	0.2	0.012	27,200	0.37
Pressure flow	4.0	5.9	0.2	0.014	38,300	0.30
Overtopping flow	8.5	9.2	0.3	0.017	70,250	0.32
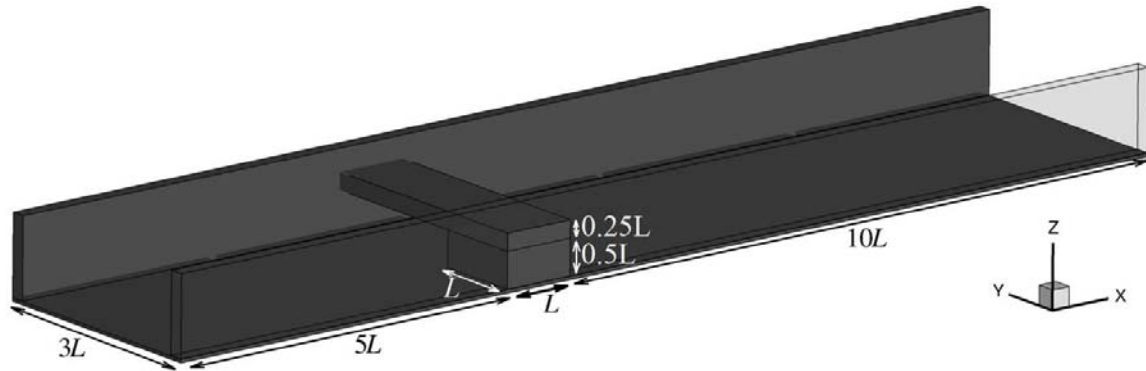
Figure 6-1 Computational domain

In the LES, a constant discharge is introduced into the system at the inlet section, a simplified inlet treatment, which is necessary due to the fact that the water surface elevation is unknown at the inlet. The convective boundary condition is used at the outlet to make sure that coherent structures leave the system without creating unphysical oscillations. The no-slip boundary condition is employed for smooth side walls and bottom of the flume as well as for the walls of the bridge abutment and deck. The computational domains are discretized with a fine uniform mesh for each case for which the details of the grid resolution in wall units are given in Table 6-2. The flow is driven by gravity, g=9.81 m/s^2 and the dynamic viscosity and density of water (air) are 1×10-3(1.8075×10-5)kg/(ms) and 1000(1.205)kg/m^3, respectively; hence, Reynolds number, **R**, and Froude number, **F**, of the simulation are the same as in the experiment.

Table 6-2 Grid resolution

Case	$Δx$	$Δy$	$Δz$	$Δx^+$	$Δy^+$	$Δz^+$
Free flow	0.003125	0.003125	0.0011250	38	38	7
Pressure flow	0.003125	0.003125	0.0015625	45	45	11
Overtopping flow	0.003125	0.003125	0.0015625	52	52	13

6.2 Results and Discussions

Figure 6-2 presents an overall impression of the instantaneous water surface of each flow case as predicted by the free-surface resolved large-eddy simulation. The water surface upstream of the abutment is fairly calm for the free flow (Figure 6-2a). However, there is a marked dip around the leading edge of the abutment, a couple of well-pronounced standing waves slightly downstream of that edge and a rough and wavy water surface downstream of the abutment. The bottom right blow-up visualizes the

water surface dip, which is the result of strong local streamwise velocity acceleration, and the standing waves. A stagnation point occurs on the upstream side of the bridge deck and the flow is concentrated under the bridge deck for the pressure flow (Figure 6-2b). Vortices formed due to vortex shedding immediately downstream of the abutment lose their coherency as they move toward the downstream. For the overtopping flow Figure 6-2c), the flow accelerates over the bridge resulting in a marked drop of the water surface. The flow plunges downstream of the bridge, which results in a standing wave or an undular hydraulic jump. Downstream of the standing wave the flow recovers gradually, exhibiting wavy motion, to the uniform flow condition. In general, Figure 6-2 shows very good qualitative agreement between the numerical results and the conditions observed in the laboratory experiment.

A more quantitative assessment of the predictive capabilities of the simulation results is provided in Figures 6-3 and 6-4, which depict measured (dots) and simulated (line) longitudinal (Figure 6-3) and cross-sectional profiles (Figure 6-4) of the water surface for each flow case. Free flow, pressure flow, and overtopping flow water surface profiles are shown at the bottom, in the middle, and at the top, respectively in Figures 6-3 and 6-4. The simulated longitudinal profiles (Figure 6-3) along A and B (see bottom sketch of Figure 6-4) are in very good agreement with the observed data. For free flow, the water surface is above the uniform flow depth immediately upstream of the abutment due to the backwater effect. Flow acceleration starting from the leading edge of the abutment leads to a depression of the water surface before it recovers slowly towards uniform flow depth. The standing wave seen in Profile A appears overpredicted slightly

by the numerical simulation, however this feature was also observed in the laboratory experiment but wasn't picked up by the point gage measurement.
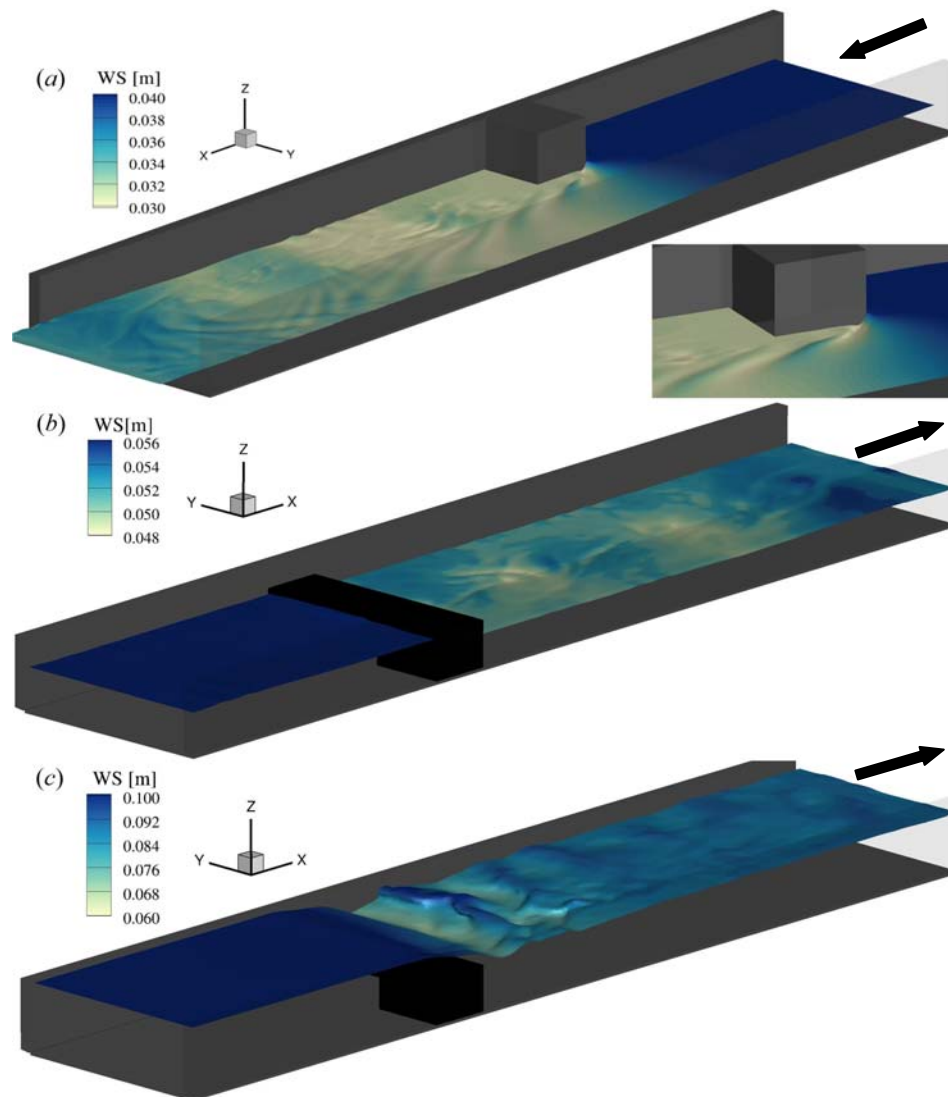
Figure 6-2 3D view of the simulated water surface corresponding to a) free flow (flow from right to left), b) pressure flow (flow from left to right), c) overtopping flow (flow from left to right)
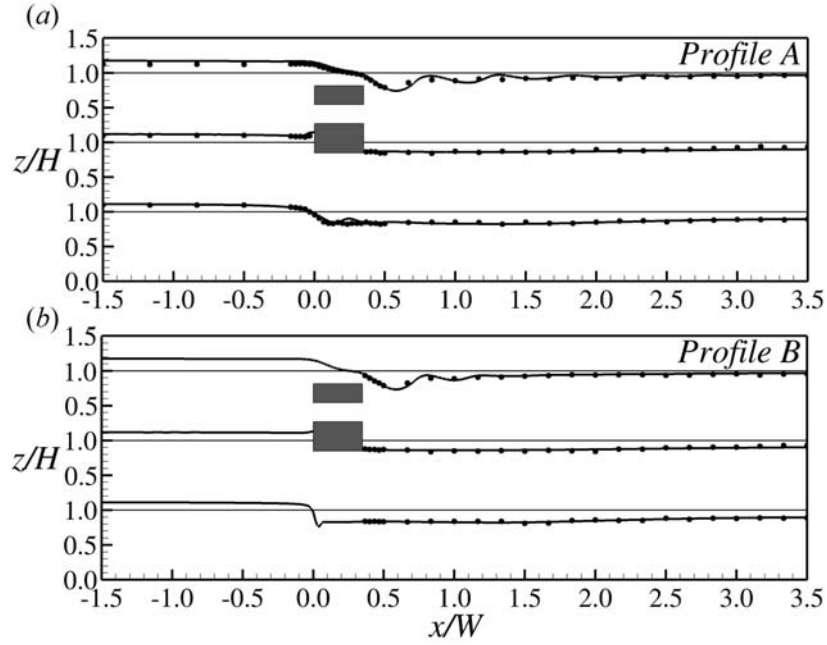
Figure 6-3 Longitudinal water surface profiles along two locations for each flow case: Solid black line shows simulated profile, solid grey line shows normalized uniform flow depth, and dots show the experimental data.
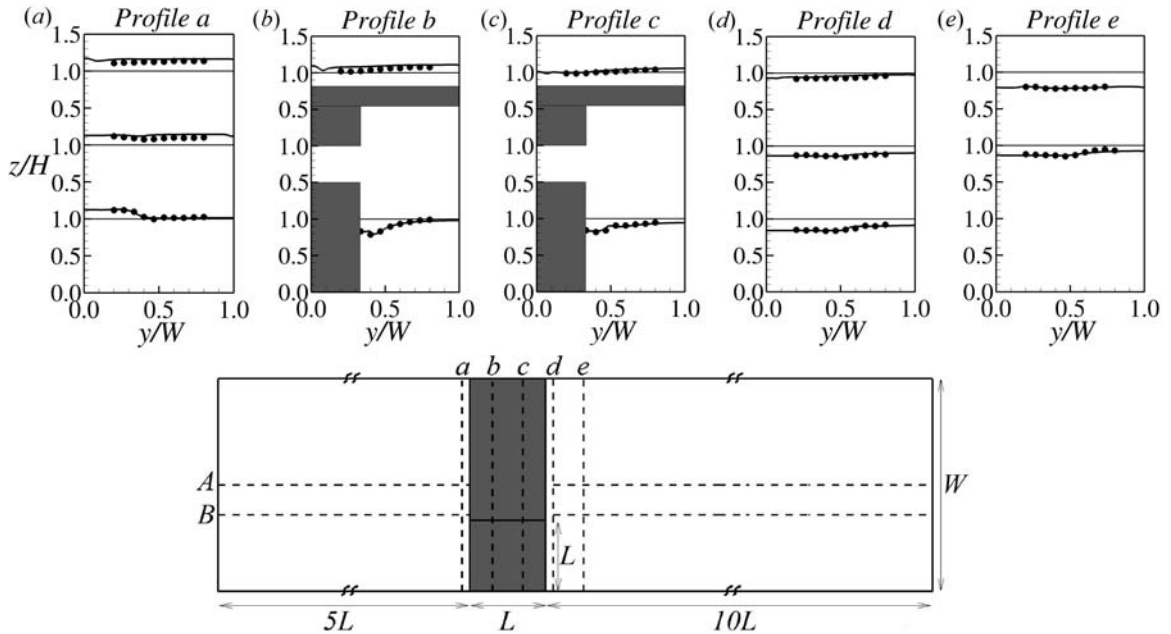
Figure 6-4 Cross-sectional water surface profiles along four locations for each flow cases: Solid black line shows simulated profile, solid grey line shows normalized uniform flow depth, and dots show the experimental data.

105

For pressure flow, the water surface level increment with an additional local rise immediately upstream of the bridge deck due to backwater effect and recovering towards the uniform flow depth in the downstream are captured well. For overtopping flow, there is a small but consistent overestimation of the water surface elevation on and upstream of the bridge. This is because the bridge deck of the numerical simulation is slightly higher than the one used in the experiment. There is some discrepancy between numerical prediction and measurement in the vicinity of the standing wave, an area that is highly turbulent and where accurate water surface measurements using a point-gage are difficult to achieve. Figure 6-4 presents measured and simulated cross-sectional water surface profiles at selected locations (Figure 6-4 a-e). The numerically predicted profiles are in very good agreement with the measured ones. For free flow, the slight overestimation of the standing wave seen at Profile A are also noticed in Profiles c and d, however the differences are very subtle and the accuracy of the point gage is probably not high enough to resolve such features. The numerically predicted profiles are slightly higher than the measured ones immediately upstream of the bridge deck for pressure flow (Profile a) and, upstream and on the bridge deck sections for overtopping flow (Profiles a and b) due to having a slightly higher bridge deck in the simulation.

Figure 6-5 presents the comparison of LES calculated time-averaged streamwise velocities of free flow, pressure flow and overtopping flow simulations for a horizontal plane at $z+=100$. From the figure it is seen that the flow separation at the leading abutment edge is more pronounced for the free flow and pressure flow simulations leading to a larger recirculation zone in the contracted area and behind the abutment than for the overtopping case. The higher velocity values on the downstream side of the bridge

are the result of the shear layer created between the large recirculation zone behind the abutment and the flow coming from the contracted area (Figure 6-5 a,b). Overtopping flow results in a smaller recirculation zone and exhibits higher velocity values through the bridge in the contracted area.

Figure 6-5 Distribution of normalized streamwise velocity in a horizontal plane near the bed at $z^+=100$ computed from a) free flow, b) pressure flow, and c) overtopping flow simulations.

Figure 6-6 depicts more quantitative evidence of the velocity field behavior by showing near-bed streamwise velocity profiles in the spanwise direction (Figure 6-6 a,b,c) and streamwise velocity profiles in the vertical direction at the centerline of the

flume (Figure 6-6 d,e,f). The shear layer downstream of the bridge disturbs the log-law

velocity profile (Figure 6-6 e). Closer to the outlet of the constriction, the effect of the

shear layer diminishes and velocity values approach the bulk velocity because the water

surface approaches the uniform flow depth (Figure 6-6f).

Figure 6-6 Streamwise velocity profiles at selected locations. *a-c* for near bed at $z^+=100$
in spanwise direction and *d-f* for the half width of the flume in vertical direction. Dashed-
dotted line, dashed line, and solid line show the profile for free flow, pressure flow, and
overtopping flow, respectively.

Figure 6-7 presents the comparison of LES calculated turbulent kinetic energy,

tke, normalized with the squared mean shear velocity for uniform depth, u_*^2, for free

flow, pressure flow and overtopping flow simulations in a horizontal plane at $z^+=100$.

Areas of high *tke* occur immediately before and at the leading edge of the abutment and

in the shear layer of the flow separation zone in the contracted region and downstream of the abutment. For overtopping flow, the recirculation zone downstream of the abutment is compacted because of the stronger shear layer at the interface between this zone and the fast orifice flow underneath the bridge. This results in a highly concentrated *tke* region behind the abutment and the highest *tke* values downstream of the abutment for the overtopping flow. It is worthy of note that the maximum normalized *tke* is 60 to 70 times the value of u_*^2 in this region.
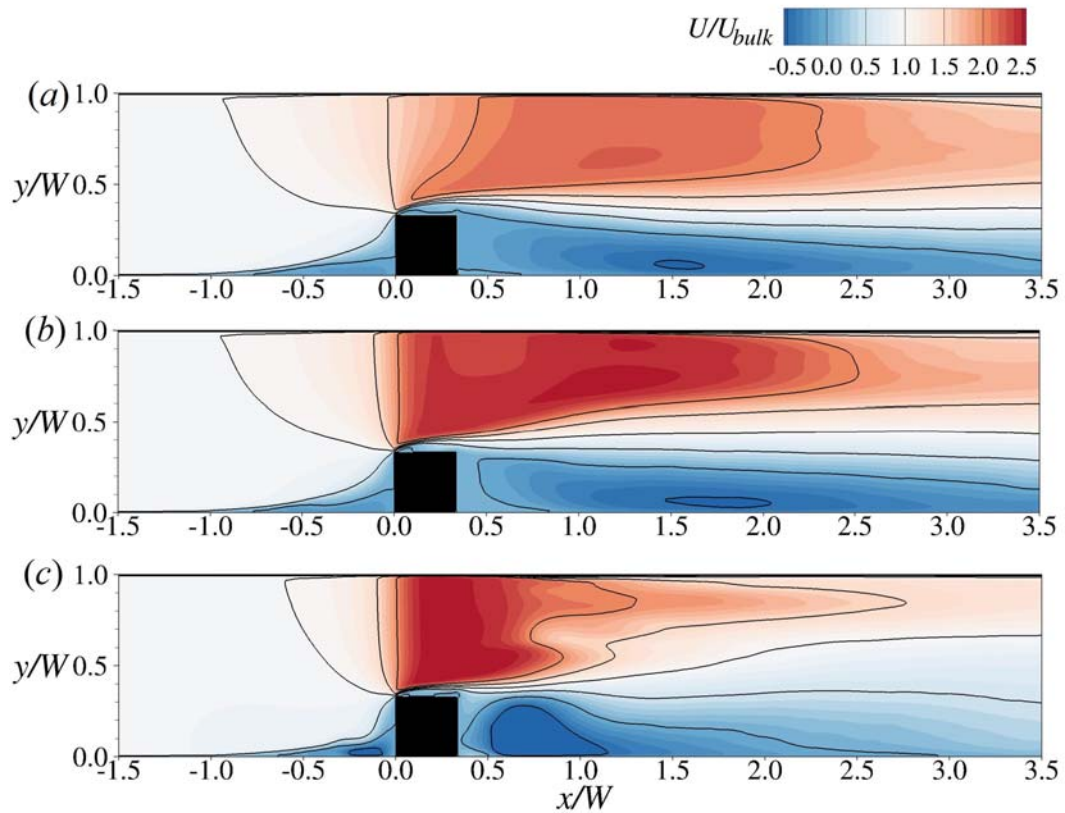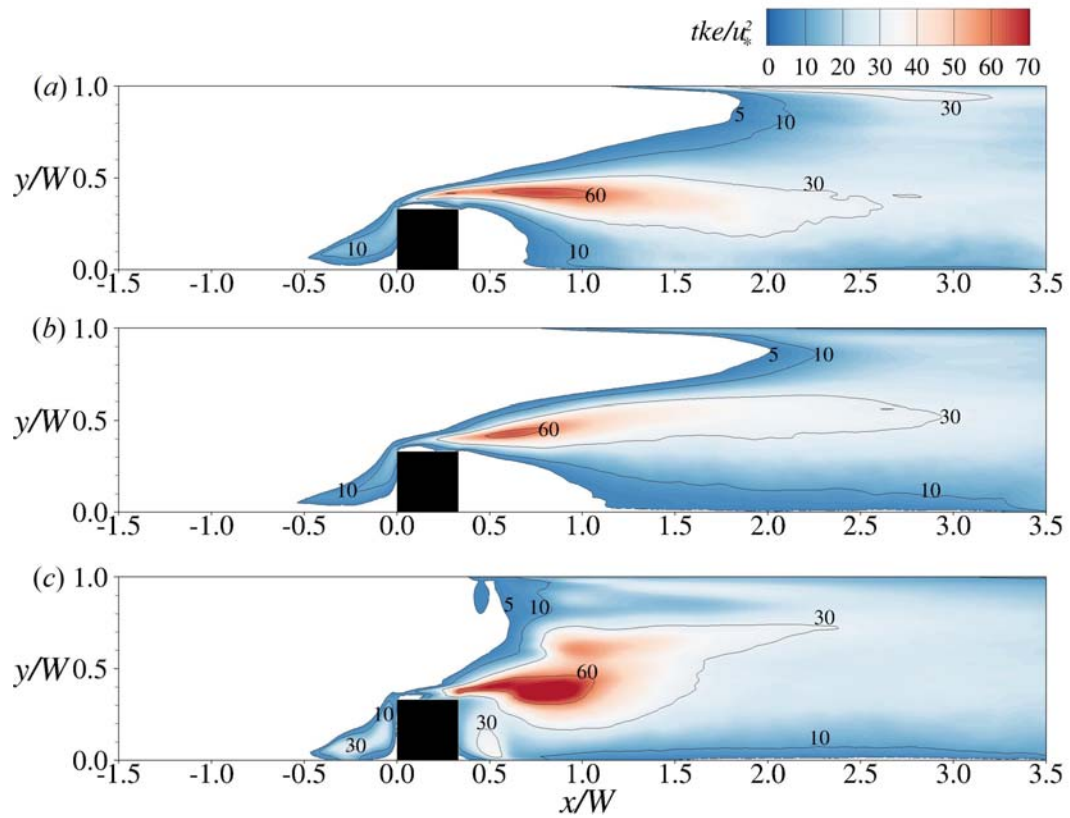

Figure 6-7 Distribution of normalized turbulent kinetic energy in a horizontal plane near the bed at $z^+=100$ computed for a) free flow, b) pressure flow, and c) overtopping flow simulations.

Figure 6-8 presenting the streamwise *tke* profiles at selected locations provides further quantitative evidence of concentration of *tke* downstream of the abutment in Figure 6-8b. In the shear layer of the flow separation zone in the contracted region, the maximum *tke* magnitude is observed for free flow case (Figure 6-8a). Figure 6-8d-f depict fairly uniform distribution of *tke* at y/W=0.5 for all cases except under the bridge deck where high *tke* area is obtained for pressure flow and overtopping flow simulations due to the turbulence created by bridge deck.
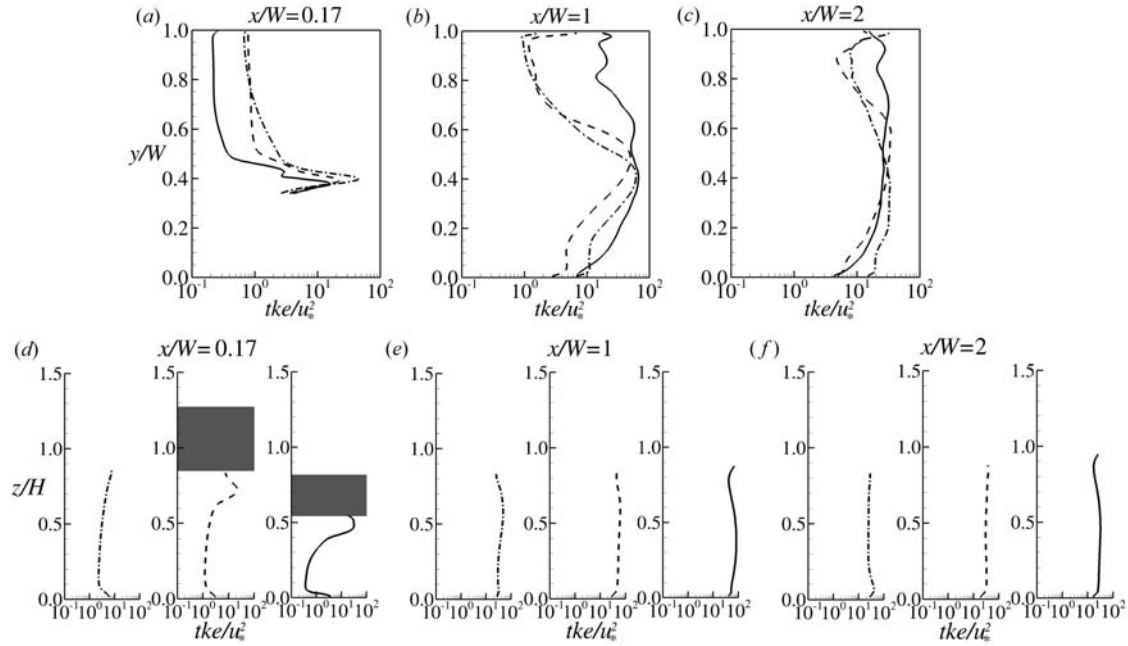
Figure 6-8 Streamwise turbulent kinetic energy profiles at selected locations *a-c* for near bed at z^+=100 in spanwise direction and *d-f* for the half width of the flume in vertical direction. Dashed-dotted line, dashed line, and solid line show the profile for free flow, pressure flow, and overtopping flow, respectively.

Figure 6-9, 6-10, and 6-11 show the streamwise, cross-streamwise, and vertical normal stress profiles for selected locations (Figure 6-9, 10 and 11 a-c for near bed at

$z^+=100$ in spanwise direction and d-f for the half width of the flume in vertical direction).

It is seen from Figures 6-9a and 6-9d that the most of the *tke* is produced by streamwise

normal stresses at the contracted section (x/W =0.17) except under the bridge deck where

cross-streamwise and vertical normal stresses also show the influence of the underside of

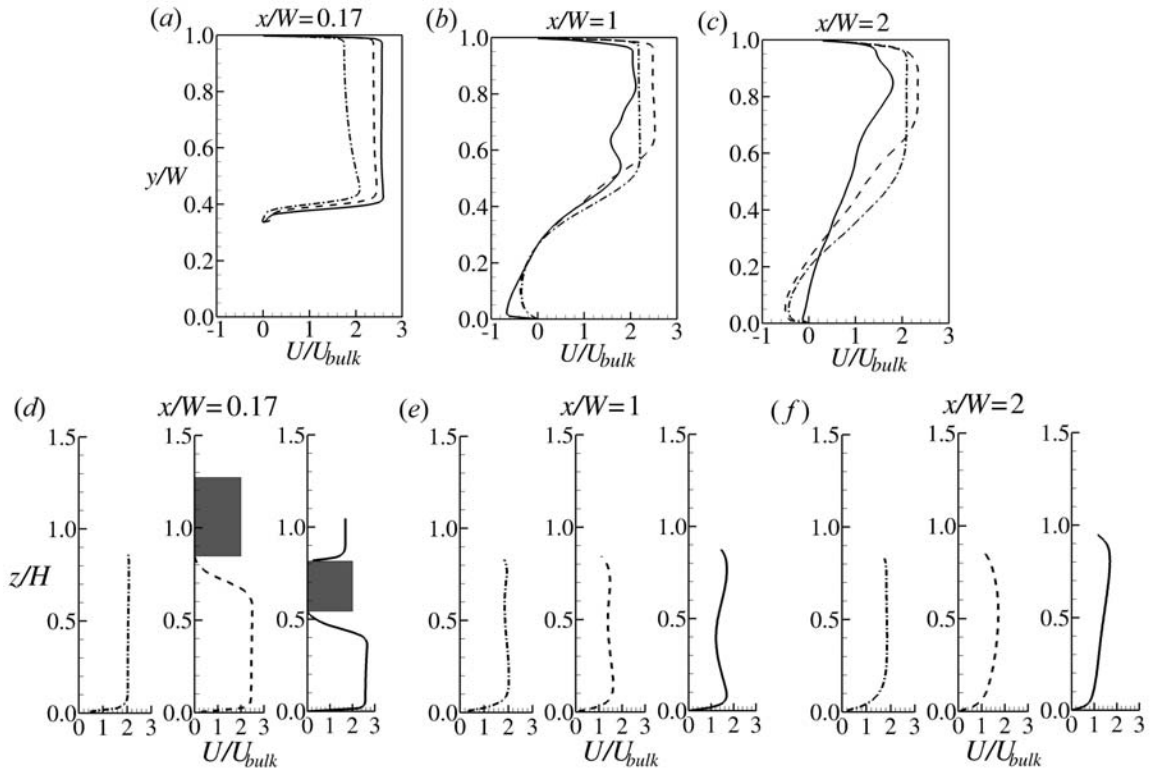the bridge deck for pressure flow and overtopping flow simulations.
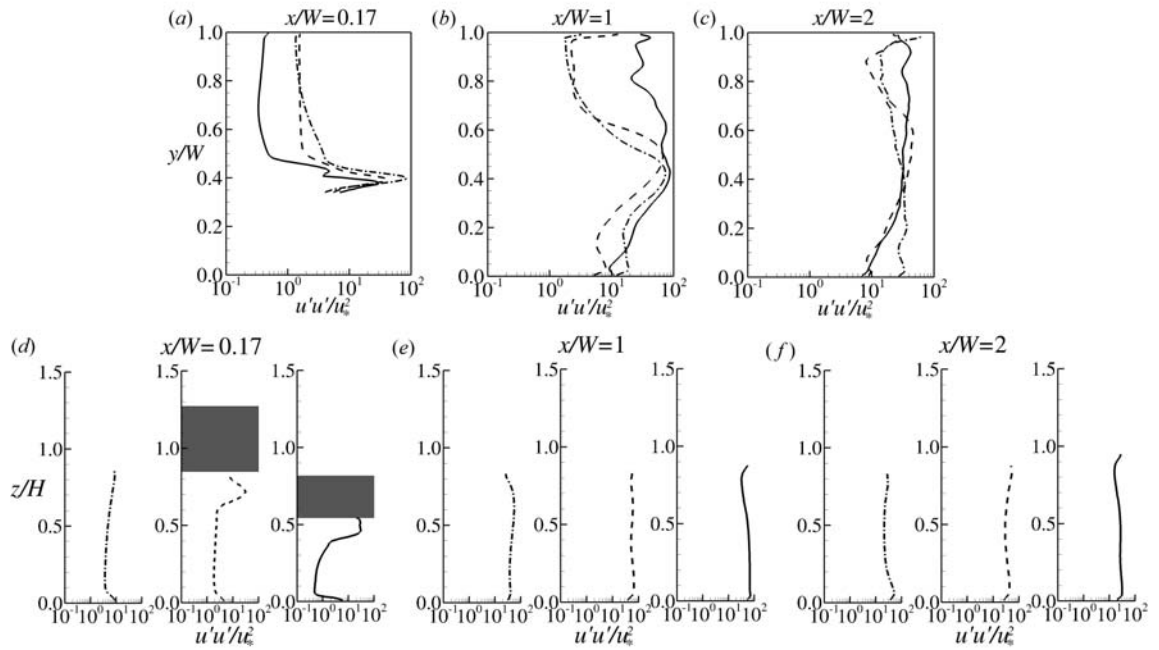
Figure 6-9 Streamwise normal stress profiles at selected locations. *a-c* for near bed at $z^+=100$ in spanwise direction and *d-f* for the half width of the flume in vertical direction. Dashed-dotted line, dashed line, and solid line show the profile for free flow, pressure flow, and overtopping flow, respectively.

The profiles at x/W =1 shows that all normal stresses contribute to *tke* production

due to the recirculation zone behind the abutment at that location. The streamwise normal

stresses have the biggest contribution to *tke* production in that area for all flow

conditions. The contribution of vertical normal stresses increase for overtopping flow at

the point ($z/H≈0.5$) where it is still possible to see the effect of high *tke*'s coming from

111

fast orifice flow under the bridge deck and overtopping flow over the bridge deck coincide. The high *tke* values mostly produced by streamwise normal stresses at $x/W = 2$ for each flow condition are highest near the side walls and bottom wall for the free flow. This is because of the wall shear effects decelerating the flow to return to uniform flow Figure 6-9c.
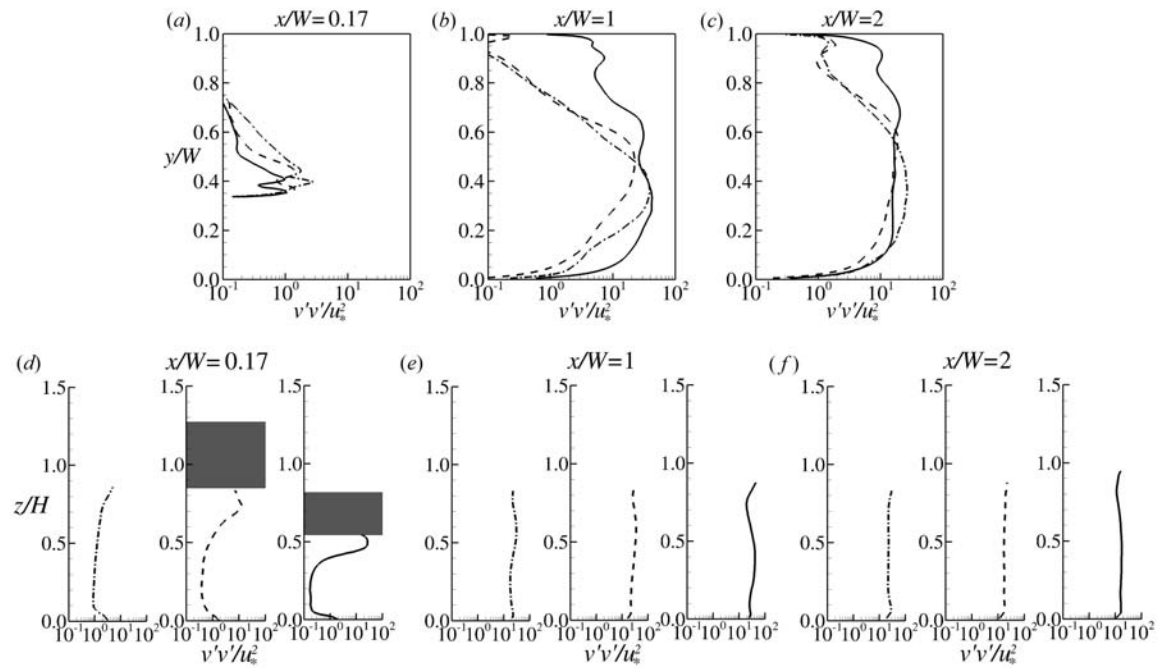
Figure 6-10 Cross-streamwise normal stress profiles at selected locations. *a-c* for near bed at $z^+=100$ in spanwise direction and *d-f* for the half width of the flume in vertical direction. Dashed-dotted line, dashed line, and solid line show the profile for free flow, pressure flow, and overtopping flow, respectively.
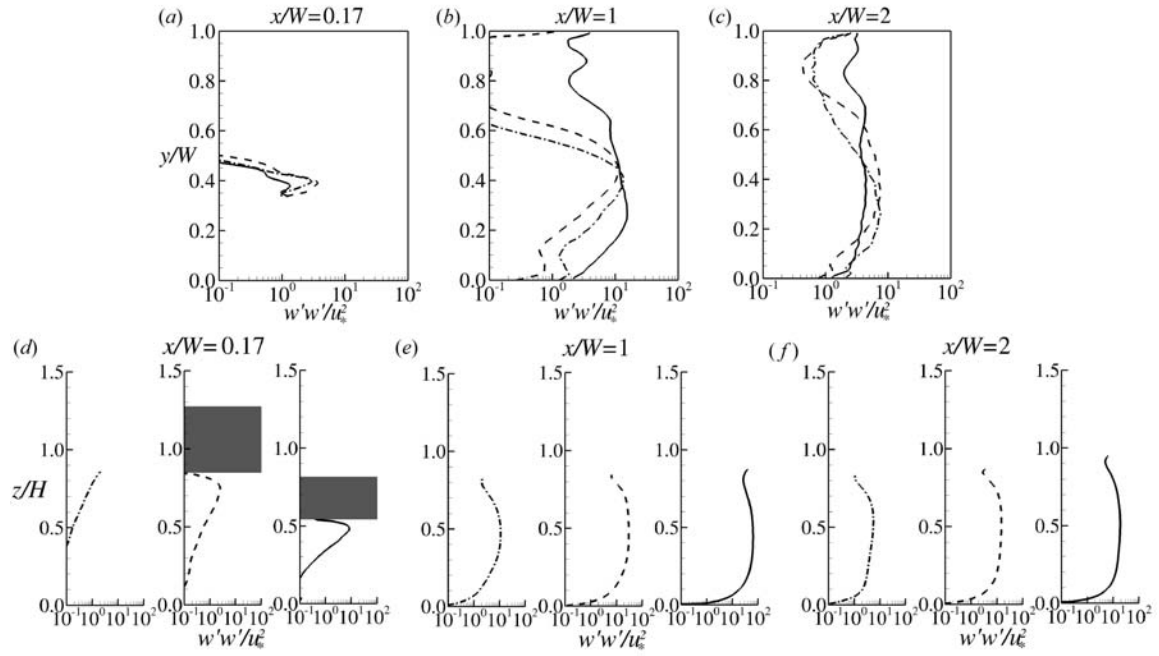
Figure 6-11 Vertical normal stress profiles at selected locations. *a-c* for near bed at $z^+=100$ in spanwise direction and *d-f* for the half width of the flume in vertical direction. Dashed-dotted line, dashed line, and solid line show the profile for free flow, pressure flow, and overtopping flow, respectively.

Figure 6-12 presents distributions of bed shear stress, τ (calculated as $\tau=\mu dS/dz$, where $S=\sqrt{U^2+V^2}$) normalized with the mean uniform flow shear stress ($<\tau>=\rho gRS$). High values of bed shear stress are observed close to the leading edge of the abutment where the horseshoe vortex system is present, in the contraction region where the flow accelerates and at the shear layer region slightly downstream of the abutment where high velocity coming from the contracted region is adjacent to the recirculation zone behind the abutment.
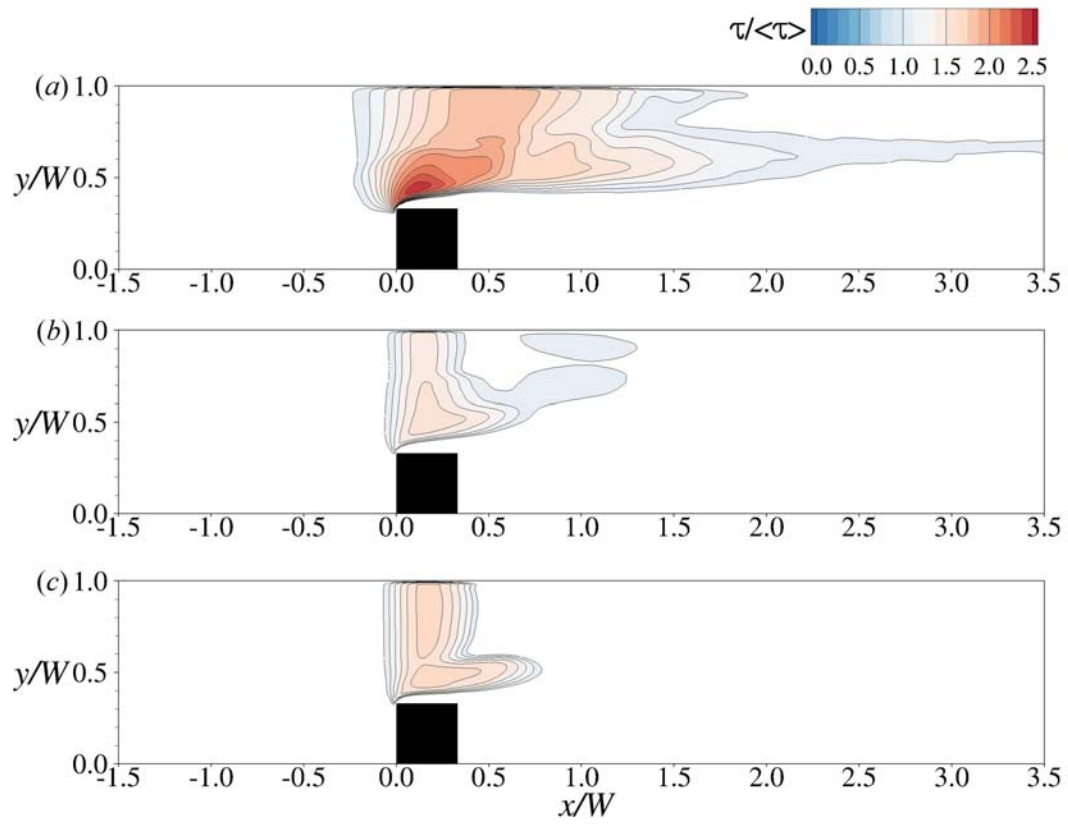
Figure 6-12 Distribution of normalized bed shear stress as computed for a) free flow, b) pressure flow, and c) overtopping flow simulations.

Figure 6-13 provides a more quantitative comparison of bed shear stress distributions by presenting profiles for selected locations for each flow type simulation. Figure 6-13a shows that the horseshoe vortex system for free flow results in nearly 50% higher bed shear stress values at the leading edge of the abutment compared to pressure flow and overtopping flow.
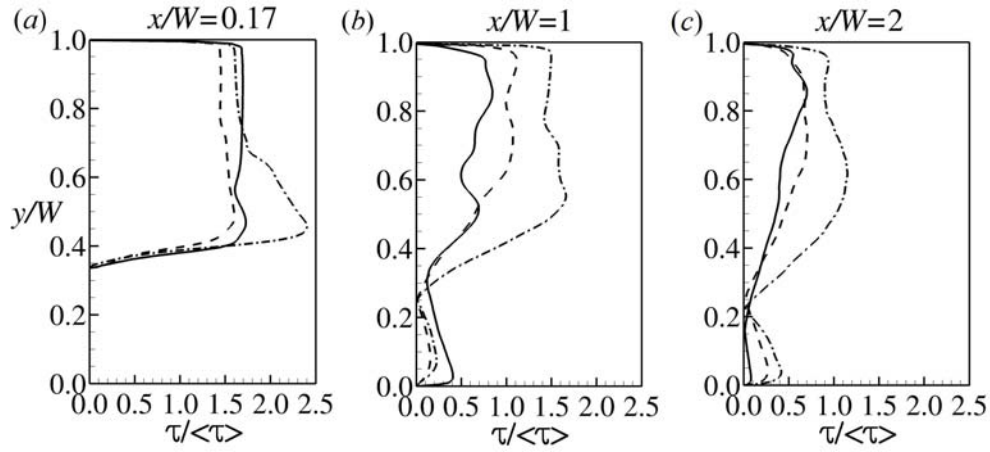
Figure 6-13 Bed shear stress profiles at selected locations. Dashed-dotted line, dashed line, and solid line show the profile for free flow, pressure flow, and overtopping flow, respectively.

Figure 6-14 depicts the vorticity magnitude for free flow, pressure flow, and overtopping flow simulations at the horizontal plane at $z^+=100$. Areas of high vorticity magnitude are observed within the horseshoe vortex system and in the shear layers of the separation zones upstream of the abutment and in the contracted area. Overtopping flow exhibits areas of especially high values of vorticity magnitude behind the abutment and in the region where fast orifice flow under the bridge deck interacts with the plunging flow over the deck.
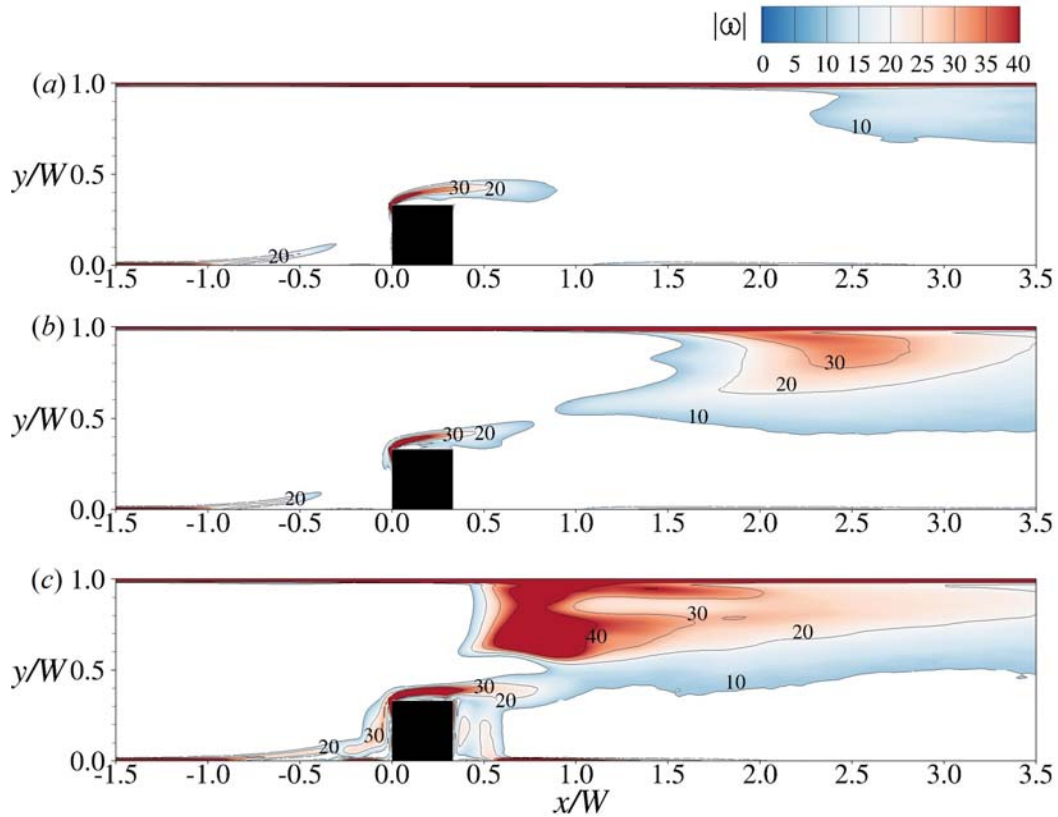
Figure 6-14 Distribution of vorticity magnitude in a horizontal plane near the bed at $z^+=100$ computed from a) free flow, b) pressure flow, and c) overtopping flow simulations.

6.3 Summary and Conclusions

LES results for simulations of free surface flow around an abutment, submerged orifice flow with a partially submerged bridge deck, and overtopping flow over the bridge were investigated in a comparative study. Water surface profiles obtained by employing LSM were validated for each case with data from a physical model of the bridge under analogous flow conditions. First and second order turbulence statistics were compared for each flow type. The flow accelerates in the contracted area, which is where high magnitudes of the primary velocities are found, however peak velocities are observed

downstream of the bridge, which is where water levels are lowest. The orifice flow suffers a vertical contraction and a local pressure gradient, hence the velocities for this case attain the highest values. The maximum *tke* values of each case are found downstream of the bridge, which is where the horizontal recirculation zone behind the abutment and the high-velocity flow through the bridge opening create and area of high shear. The highest values of *tke* are observed for the overtopping case where the horizontal recirculation zone behind the abutment, the fast orifice flow underneath the bridge and the vertical recirculation zone from the flow over the deck meet and interact. The bed shear stress comparison for these three flow cases showed that the horseshoe vortex system resulted in highest bed shear stress values at the leading edge of the abutment for free flow. Areas of high bed shear stress are found in the contracted are underneath the deck. Although high vorticity magnitudes are observed within the same regions around the abutment for each flow cases, another highest vorticity magnitude area is found for overtopping flow case in the region where fast orifice flow under the bridge deck interacts with the plunging flow over the deck.

CHAPTER 7

SUMMARY AND CONCLUSIONS

7.1 Summary

Scour at bridge foundations during extreme hydrologic events is a leading cause of bridge failure. Most previous research on bridge scour has been experimental and conducted in rectangular flumes that are not representative of prototype rivers. Rivers are typically compound channel sections with a floodplain and main channel subject to a nonuniform velocity distribution across the flood channel width. The result is intense interaction and exchange of momentum between the floodplain and main channel that creates turbulence. The bridge crossing itself usually consists of an embankment and an abutment that terminates on the floodplain or near the main channel bank. The result is flow contraction as some portion of the floodplain flow joins the main channel flow in the bridge opening which leads to a combination of local scour around the abutment and contraction scour over much of the cross section. In addition to the floodplain/main channel flow interactions, the main features of the flow include the generation of a horseshoe vortex by the bridge obstruction, a separated shear flow, and a downstream recirculation region as the approach flow is obstructed and sweeps through the bridge opening. In addition, the bridge may be subject to submerged orifice flow and overtopping as well as free surface flow. The objective of this thesis was to incorporate all of these realistic geometric and flow features into an advanced CFD model with a highly accurate free surface computation algorithm and advanced turbulence modeling

approach that could be used to explore the full dynamics of the flow field which are ultimately responsible for the scour process.

The thesis objective was achieved by developing a refined Large Eddy Simulation (LES) code which was successfully validated with experimental data. Refinement of the LES code proceeded in a series of steps each of which is essential to correctly and accurately simulating a turbulent flow in a compound channel which is obstructed by a bridge crossing. First of all, the code has been used to analyze in detail the flow in compound channels with deep and shallow overbank flows. Detailed analysis of the turbulence statistics has been carried out and specifics of the main-channel-floodplain interface shear and turbulence production have been reported. Secondly, the code has been equipped with a free surface algorithm based on the Level Set Method (LSM) which allows accurate predictions of 3D turbulent flow and water surface profiles around hydraulic structures. A fifth-order weighted essentially non-oscillatory (WENO) scheme was implemented for the convective fluxes in the momentum and level set equation to obtain the necessary compromise between numerical accuracy and algorithm stability which is especially important for the free surface algorithm. The code was validated systematically using the challenging test case of a traveling solitary wave and associated wave runup at a solid boundary. Thirdly, the method was then applied to three different flows around bridge structures of increasing complexity. The flow around an abutment in a channel was investigated first; in particular the free-surface-effects on the turbulence structures of such flows were investigated. Then the flow through a bridge opening with deck overtopping was studied and the code reproduced accurately the strongly deformed free surface over the bridge. Details of the turbulence structure and the time-averaged and

119

instantaneous flow have been revealed. Finally, submerged orifice flow was investigated and comparisons of this flow with the two other flow types in terms of flow and turbulence quantities were made.

7.2 Conclusions

The numerical simulations and analysis explained throughout the thesis have made several unique contributions both in terms of the numerical methodology employed and the conclusions that could be drawn regarding the flow and turbulence properties that are primary agents of scour around bridge foundations during extreme floods in which the bridge is likely to be submerged and even overtopped. In general, it can be concluded from the thesis that numerical simulations of such flows require accurate treatment of the significant deformation of the water surface that occurs, not only to predict the water surface elevations, but also to correctly predict the turbulence properties of the flows. More specific conclusions are given below.

7.2.1   Investigation of Hydrodynamics of Compound Channels

The results of large eddy simulations (LESs) of turbulent flow in a compound open channel with deep and shallow flood plain depths were presented. The simulations were validated with experimental data, and good agreement between measured and calculated data was found. It was determined that the floodplain-depth-to-main channel-depth ratio is an important parameter affecting first- and second-order turbulence statistics. The streamwise momentum balance was analyzed with respect to the momentum transfer at the interface between the main channel and the floodplain, and it

was found that secondary currents as well as primary and secondary Reynolds stresses contribute to the streamwise momentum transport. Depth-averaging of the streamwise momentum equation revealed the existence of an apparent shear stress at the main channel-floodplain interface caused by turbulent shear stress terms in the main channel and secondary currents in the floodplain. The apparent shear stress was greater for the shallow floodplain case. Comparison of the LES results with an analytical solution of the depth-averaged velocity equation demonstrated the importance of case-specific calibration of the parameters of the analytical solution. The turbulence anisotropy was quantified and its role in generating secondary currents was illustrated.

7.2.2 Investigation of Free Surface Effects on Flow around an Abutment

Two separate Large Eddy Simulations (LES) were carried out to investigate the effects of accurate computation of the curvilinear water surface deformation through a bridge contraction on the resulting time-averaged and instantaneous turbulence characteristics of the flow around an abutment. The simulation with the LSM was validated with data from complementary physical model tests under analogous geometrical and flow conditions. A second, rigid-lid based simulation of the same case was carried out and streamwise velocity, bed shear stress and second order turbulence statistics obtained from both simulations were compared. The results indicate that the turbulence structure of this flow is influenced strongly by the water surface variation and therefore, the accuracy of its prediction is very important. While bed-shear stresses and first order statistics are very similar for both cases, the instantaneous turbulence structure and consequently, the second order statistics, such as turbulent kinetic energy and Reynolds stresses, are distinctly different. The turbulence structures are stretched due to

local flow acceleration caused by strong deformations of the free surface, particularly near the leading edge of the abutment. There the turbulent kinetic energy attains maximum values in the free surface simulation which is a feature not detected by the rigid-lid simulation. In addition, the results of the free surface simulation show higher streamwise and lower spanwise values of the normal Reynolds stresses due to the dominance of streamwise vortex stretching. These are significant findings, particularly because to date all LES studies of similar flows have been performed under rigid-lid conditions with the assumption that the rigid lid boundary condition is valid. These simulations demonstrate the contrary to be true.

7.2.3   Investigation of Hydrodynamics of Overtopping Flow in the Presence of Bridge Structures

The flow over a submerged bridge was investigated by employing the method of LES which allowed elucidation of the instantaneous flow and an accurate quantification of its turbulence statistics. The complex water surface deformation over the bridge was validated with data from a physical model of the bridge under analogous flow conditions. Numerically predicted water surface profiles showed good agreement with measured data. The water surface resembles that of the flow over a broad-crested weir with a plunging nappe and a standing wave downstream of the bridge. The mean flow is characterized by a multitude of complex flow features including horizontal recirculation zones upstream and downstream of the bridge abutment and vertical recirculation zones of the separated plunging flow. The latter feature is characterized by large magnitudes of turbulent kinetic energy and the formation of substantial shear layers. The location of the largest shear stress is underneath the bridge deck where the flow is contracted and

122

accelerated, but the maximum turbulent kinetic energy is found near the bed where the plunging flow from over the deck coincides with the edge of the lateral recirculation zone of the separated flow. These novel findings have significant implications relative to the location of maximum scour depth.

7.2.4 Investigation of Hydrodynamics of Turbulent Flow around a Submerged Bridge under Extreme Hydrological Conditions

LES results of the free surface flow around an abutment, submerged orifice flow with a partially submerged bridge deck, and overtopping flow over the bridge were investigated in a comparative study. Water surface profiles obtained by employing LSM were validated for each case with data from a physical model of the bridge under analogous flow conditions. First and second order turbulence statistics are compared for each flow type and it is shown that maximum *tke* values are located downstream of the bridge in each case. The highest values of *tke* occur for the overtopping case at the interface of the recirculation zone behind the abutment and the fast orifice flow underneath the bridge. Comparisons of bed shear stress values for these three flow cases show that the horseshoe vortex system produces the highest bed shear stress values at the leading edge of the abutment for free flow. Although high vorticity magnitudes are observed within the same regions around the abutment for each flow case, another area of high vorticity is found for the overtopping flow case in the region where fast orifice flow under the bridge deck interacts with the plunging flow over the deck. Thus, these LES results show for the first time the turbulent structure generated by the three different types of flow that were studied.

7.3 Recommendations for Future Research

In the near future, the current study may be extended to apply local mesh refinement. This provides an opportunity to use smaller grid sizes near the structures where high resolution is needed to resolve highly turbulent areas better and to increase the size of the mesh gradually in the direction moving away from the structures. Successful implementation of this local mesh refinement in the current 3D LES code will decrease the cost and computational effort and will make it possible to use the code for larger domains and larger Reynolds numbers.

Future simulations of more realistic hydraulic structures and channel shapes should be carried out; for instance, sloping abutments protected by rock rip-rap, more detailed bridge models (e.g. including girders), bridges with abutments and piers and more complex channel shapes (e.g. compound channels) in combination with flow through a bridge having realistic geometry.

In this thesis, areas of high bed shear stress and *tke* are regions of interest because they represent possible areas of maximum scour depth where bed shear stress values may exceed critical shear stresses of sediment particles. In future studies, sediment transport equations can be implemented in the current 3D LES code, and these equations can be coupled with LSM to obtain the deformation of the interface between sediment bed and fluid. Then, it will be possible to compute maximum scour depths around bridge structures which are a critical component in terms of economical and safe design of future bridges and protection of existing bridges.

REFERENCES

Bai, J., Fang, H. and Stoesser, T. (2012). "Transport and Deposition of Fine Sediment in Open Channels with Different Aspect Ratios." Earth Surface Processes and Landforms, 38(6), 591-600.

Biglari, B. and Sturm, T. W. (1998). "Numerical modeling of flow around bridge abutments in compound channel." J. Hydr. Engrg., ASCE, 124(2), 156-164.

Bomminayuni, S. and Stoesser, T. (2011). "Turbulence Statistics of Open-Channel Flow over a Rough Bed." ASCE, Journal of Hydraulic Engineering, 137 (11), 1347-1358.

Broglia, R., Pascarelli, A. and Piomelli, U. (2003). "Large-Eddy Simulations of ducts with a free surface." J. Fluid Mech. 484, 223-253.

Bunner, B., 1998. MG NET.

Cater, J. E. and Williams, J. J. R. (2008). "Large eddy simulation of a long asymmetric compound channel." J. Hydr. Res., 46(4), 445-453.

Chan, R.K.-C. and Street, R.L. (1970). "A computer study of finite-amplitude water waves." Journal of Computational Physics 6(1), 68-94.

Chen, S., Johnson, D.B., Raad, P.E. and Fadda, D. (1997). "The surface marker and micro cell method." International Journal for Numerical Methods in Fluids 25(7), 749-778.

Chrisohoides, A., Sotiropoulos, F. and Sturm, T. W. (2003). "Coherent structures in flat-bed abutment flow: computational fluid dynamics simulations and experiments." J. Hydr. Engrg., ASCE, 129(3), 177-186.

Constantinescu G., Sukhodolov A. and McCoy A. (2009). "Mass exchange in a shallow channel flow with a series of groynes: LES study and comparison with laboratory and field experiments." Environ. Fluid Mech., 9, 587-615.

Croce, R., Griebel, M. and Schweitzer, M.A. (2004). "A parallel level-set approach for two-phase flow problems with surface tension in three space dimensions." Citeseer.

Daly, B.J. (1967). "Numerical Study of Two Fluid Rayleigh-Taylor Instability." Physics of fluids 10, 297.

DeBar, R. (1974). "Fundamentals of the KRAKEN code." Lawrence Livermore Laboratory, UCIR-760.

Glimm, J., Grove, J.W., Li, X.L., Shyue, K.-m., Zeng, Y. and Zhang, Q. (1998). "Three-dimensional front tracking." SIAM Journal on Scientific Computing 19(3), 703-727.

Gotvald, A.J. and McCallum, B.E. (2010). Epic flooding in Georgia. USGS Fact Sheet: 2010-3107.

Griebel, M., Dornsheifer, T. and Neunhoeffer, T. (1998). "Numerical simulation in fluid dynamics: a practical introduction." Siam, Philadelphia.

Guo, J., Zhang, T. C., Admiraal, D. M and Bushra, A. (2009). "Computational design tool for bridge hydrodynamic loading in inundated flows of Midwest Rivers." Report # MATC-UNL:227.

Harlow, F.H. and Welch, J.E. (1965). "Numerical Calculation of Time-Dependent Viscous Incompressible Flow of Fluid with Free Surface." Physics of fluids 8, 2182.

Hirt, C.W. and Nichols, B.D. (1981). "Volume of fluid (VOF) method for the dynamics of free boundaries." Journal of Computational Physics 39(1), 201-225.

Hong, S-H., Sturm, T.W. and Stoesser, T. (2014). "Prediction of Clear-Water Abutment Scour Depth in Compound Channel for Extreme Hydrologic Events." J. Hydr. Engrg., ASCE, under review.

Kang, S., Lightbody A., Hill C. and Sotiropoulos F. (2011). "High-resolution numerical simulation of turbulence in natural waterways." Advances in Water Resources, 34, 98-113.

Kang, S. and Sotiropoulos, F. (2012). "Numerical modeling of 3d turbulent free surface flow in natural waterways." Advances in Water Resources, 40, 23–36.

Kara, M. C., Stoesser, T. and Will, K. (2012). "A Numerical Method to predict fluid-structure interaction of flow past an elastically mounted circular cylinder." Proceedings of the Twenty-second (2012) International Offshore and Polar Engineering Conference, Rhodes, Greece, June 17–22, 2012.

Kara, S., Mulahasan, S., Stoesser, T. and Sturm, T. W. (2014). "Water surface response to flow through bridge openings." Proceedings of River Flow 2014, Lausanne, Switzerland (Under Review).

Kim, S.J. and Stoesser, T. (2011). "Closure modeling and direct simulation of vegetation drag in flow through emergent vegetation." Water Resour. Res., 47, W10511, doi:10.1029/2011WR010561.

Kim, D., Kim, J.H. and Stoesser, T. (2013). "The effect of baffle spacing on hydrodynamics and solute transport in serpentine contact tanks." IAHR J. Hydr. Res., 51(5), 558-568.

Knight, D. W. and Demetriou, J. D. (1983). "Flood plain and main channel flow interaction." J. Hydr. Engrg., ASCE, 109(8), 1073-1092.

Koken, M. and Constantinescu, G. (2008). "An investigation of the flow and scour mechanisms around isolated spur dikes in a shallow open channel. Part I. Conditions corresponding to the initiation of the erosion and deposition process." Water Resources Research, 44, W08406, DOI: 10.1029/2007WR006489.

Koken, M. and Constantinescu, G. (2009). "An investigation of the dynamics of coherent structures in a turbulent channel flow with a vertical sidewall obstruction." Physics of Fluids, 21, 085104, DOI 10.1063/1.3207859.

Krishnappan, B. G. and Lau, Y. L. (1986). "Turbulence modeling of flood plain flows." J. Hydr. Engrg., ASCE, 112(4), 251-266.

Lee, D., Nakagawa, H., Kawaike, K., Baba, Y. and Zhang, H. (2010). "Inundation flow considering overflow due to water level rise by river structures." Annuals of Disas. Prev. Res. Inst., Kyoto Univ., No. 53 B.

Malavasi, S. and Guadagnini, A. (2003). "Hydrodynamic loading on river bridges." J. Hydr. Engrg., ASCE, 129 (11), 854-861.

Malavasi, S. and Guadagnini, A. (2007). "Interactions between a rectangular cylinder and a free-surface flow." Journal of Fluids and Structure, 23, 1137–1148.

Melville, B. W. (1992). "Local scour at bridge abutments." J. Hydr. Engrg., ASCE, 118 (4), 615-631.

Melville, B. W. (1995). "Bridge abutment scour in compound channels." J. Hydr. Engrg., ASCE, 121 (12), 863-868.

Myers, R. C. and Elsawy, E. M. (1975). "Boundary shear in channel with flood plain." J. Hydr. Div., ASCE, 101(7), 933-946.

Nagata, N., Hosoda, T., Nakato, T. and Muramoto, Y. (2005). "Three-dimensional numerical model for flow and bed deformation around river hydraulic structures." Journal of Hydraulic Engineering 131(12), 1074-1087.

Naot, D., Nezu, I. and Nakagawa, H. (1993). "Hydrodynamic behavior of compound rectangular open channels." J. Hydr. Engrg., ASCE, 119(3), 390-408.

Nezu, I. and Nakagawa, H. (1993). "Turbulence in open-channel flows". IAHR-Monograph, Balkema, Rotterdam, The Netherlands.

Nicoud, F. and Ducros, F. (1999). "Subgrid-scale stress modelling based on the square of the velocity gradient tensor." Flow Turbul Combust 62, 183-200.

Noh, W.F. and Woodward, P. (1976). "SLIC (simple line interface calculation)." pp. 330-340, Springer.

Oliveto, G. and Hager, W. H. (2002). "Temporal evolution of clear-water pier and abutment scour." J. Hydr. Engrg., ASCE, 128(9), 811-820.

Orlanski, I. (1976). Simple Boundary-Condition for Unbounded Hyperbolic Flows. J Comput Phys 21, 251-269.

Osher, S. and Sethian, J.A. (1988). "Fronts propagating with curvature-dependent speed algorithms based on Hamilton-Jacobi formulations." Journal of Computational Physics 79(1), 12-49.

Osher, S. and Fedkiw, R. (2002). "Level set methods and dynamic implicit surfaces." New York: Springer-Verlag.

Ouillon, S. and Dartus, D. (1997). "Three-dimensional computation of flow around groyne. J. Hydr. Engrg., ASCE 123 (11), 962-970.

Papanicolaou, A.N., Kramer, C.M., Tsakiris, A.G., Stoesser, T., Bomminayuni, S. and Chen, Z. (2012). "Effects of a fully submerged boulder within a boulder array on the mean and turbulent flow fields." Acta Geophysica. DOI 10.2478/s11600-012-0044-6.

Paik, J., Ge, L. and Sotiropoulos, F. (2004). "Toward the simulation of complex 3D shear flows using unsteady statistical turbulence models." International Journal of Heat and Fluid Flow, 25, 513-527.

Paik, J. and Sotiropoulos, F. (2005). "Coherent structure dynamics upstream of a long rectangular block at the side of a large aspect ratio channel." Physics of fluids 17, 115104.

Palau-Salvador G., Stoesser T., Fröhlich J., Kappler M. and Rodi W. (2010). "Large eddy simulations and experiments of flow around finite-height cylinders." Flow Turbulence Combust, 84, 239-275.

Parola, A.C., Hagerty, D.J. and Kamojjal, S. (1998). "Highway infrastructure damage caused by the 1993 upper Missippi River basin flooding." Rep. No. NCHRP-417, Transportation Research Board, Washington, D.C.

Pezzinga, G. (1994). "Velocity distribution in compound channel flows by numerical modeling." J. Hydr. Engrg., ASCE, 120(10), 1176-1198.

Picek, T., Havlik, A., Mattas, D. and Mares, K. (2007). "Hydraulic calculation of bridges at high water stages." Journal of Hydraulic Research, 45, 400-406.

Prandtl, L. (1925). "Bericht über Untersuchungen über die ausgebildete Turbulenz (Report on studies on developed turbulence)." Zeitschrift für Angewandte Mathematik und Mechanik 5(2), 136–139 (in German).

Prinos, P., Townsend, R. and Tavoularis, S. (1985). "Structure of turbulence in compound channel flows." J. Hydraulic Eng. 111(9), 1246-1261.

Rajaratnam, N. and Ahmadi, R. (1981). "Hydraulics of channels with floodplains." J. Hydr. Res., 19(1), 43-60.

Rodi, W., Constantinescu, G. and Stoesser, T. (2013) "Large-eddy Simulations in Hydraulics." IAHR Monograph. CRC Press. ISBN-10: 1138000248.

Sethian, J. A. and Smereka, P. (2003). "Level set methods for fluid interfaces." Annu. Rev. Fluid Mech., 35, 341-372.

Shiono, K. and Knight, D. W. (1991). "Turbulent open channel flows with variable depth across the channel." J. Fluid Mech., 222, 617–646.

Shu, C-W. (2009). "High order weighted essentially nonoscillatory schemes for convection dominated problems." SIAM Review, 51(1), 82-126.

Sofialidis, D. and Prinos, P. (1998). "Compound open-channel flow modeling with nonlinear low-Reynolds k-ε models." J. Hydr. Engrg., ASCE, 124(3), 253-262.

Stoesser, T., Palau-Salvador, G., Rummel, A. and Rodi, W. (2007). "Turbulent Shallow Flow through Vegetation." 5th International Symposium on Environmental Hydraulics (ISEH V), Tempe, Arizona, USA, 2007.

Stoesser, T., Fröhlich, J. and Rodi W. (2007). "Turbulent Open-Channel Flow over a Permeable Bed." Proc. 32nd IAHR Congress, Venice, Italy July 1-6, 2007.

Stoesser, T. and Rodi, W. (2007). "Large Eddy Simulation of open-channel flow over spheres." 9th Results and Review Workshop on High Performance Computing in Science and Engineering, Oct. 19-20, 2006. High Performance Computing in Science and Engineering '06 : 321-330.

Stoesser, T. and Nikora, V. (2008). "Flow structure over square bars at intermediate submergence: Large Eddy Simulation (LES) study of bar spacing effect." Acta Geophysica, 56(3), 876-893.

Stoesser, T. (2010). "Physically realistic roughness closure scheme to simulate turbulent channel flow over rough beds within the framework of LES." ASCE, Journal of Hydraulic Engineering, 136 (10), 812-819.

Stoesser, T., Kim, S.J. and Diplas, P. (2010). "Turbulent flow through idealized emergent vegetation." J. Hydraulic Eng. 136(12), 1003-1017.

Sturm, T. W. and Janjua, N. S. (1994). "Clear-water scour around abutments in floodplains." J. Hydr. Engrg., ASCE, 120(8), 956-972.

Sturm, T. W. (2006). "Scour around bankline and setback abutments in compound channels." J. Hydr. Engrg., ASCE, 132 (1), 21-32.

Sussman, M., Smereka, P. and Osher, S. (1994). "A level set approach for computing solutions to incompressible two-phase flow." Journal of Computational Physics 114(1), 146-159.

Tang, X. and Knight, D.W. (2008). "Lateral depth-averaged velocity distributions and bed shear in rectangular compound channels." J. Hydraulic Eng. 134(9), 1337-1342.

Teruzzi, A., Ballio, F. and Armenio, V. (2009). "Turbulent stresses at the bottom surface near an abutment: Laboratory-scale numerical experiment." J. Hydr. Engrg., ASCE 135 (2), 106-117.

Thomas, T. G. and Williams, J. J. R. (1995). "Large eddy simulation of turbulent flow in an asymmetric compound open channel." J. Hydr. Res., 33(1).

Tominaga, A. and Nezu, I. (1991). "Turbulent structure in compound open-channel flows." J. Hydr. Engrg., ASCE, 117(1), 21-40.

Tryggvason, G., Bunner, B., Esmaeeli, A., Juric, D., Al-Rawahi, N., Tauber, W., Han, J., Nas, S. and Jan, Y.-J. (2001). "A front-tracking method for the computations of multiphase flow." Journal of Computational Physics 169(2), 708-759.

van Prooijen, B. C., Battjes, J. A. and Uijttewaal, W. S. J. (2005). "Momentum exchange in straight uniform compound channel flow." J. Hydr. Engrg., ASCE, 131(3), 175-183.

van Balen, W., Blanckaert, K. and Uijttewaal, W. S. J. (2010). "Analysis of the role of turbulence in curved open-channel flow at different water depths by means of experiments, LES and RANS." J. Turbulence, 11(12), 1–34.

Wardhana, K. and Hadipriono, F. C. (2003). "Analysis of recent bridge failures in the United States." Journal of performance of constructed facilities, 17(3), 144-150.

Youngs, D. (1982). "Time-dependent multi-material flow with large fluid distortion." Numerical methods for fluid dynamics 24, 273-285.

Yue, W., Lin, C.-L. and Patel, V.C. (2003) "Numerical investigations of turbulent free surface flows using level set method and large eddy simulation." University of Iowa.

Zhao, H., Chan, T., Merriman, B. and Osher, S. (1996). "A variational level set approach to multiphase motion." J. Comput. Phys., vol. 127, no. 1, pp. 179–195.